Identification and characterization of cell edge proteins in *Arabidopsis thaliana*

A Thesis Submitted to the College of

Graduate and Postdoctoral Studies

In Partial Fulfillment of the Requirements

For the Degree of Doctor of Philosophy

In the Department of Biology

University of Saskatchewan

Saskatoon

By

Zhihai Chi

Permission to Use

In presenting this thesis/dissertation in partial fulfillment of the requirements for a Postgraduate degree from the University of Saskatchewan, I agree that the Libraries of this University may make it freely available for inspection. I further agree that permission for copying of this thesis/dissertation in any manner, in whole or in part, for scholarly purposes may be granted by the professor or professors who supervised my thesis work or, in their absence, by the Head of the Department or the Dean of the College in which my thesis work was done. It is understood that any copying or publication or use of this thesis or parts thereof for financial gain shall not be allowed without my written permission. It is also understood that due recognition shall be given to me and to the University of Saskatchewan in any scholarly use which may be made of any material in my thesis.

Requests for permission to copy or to make other uses of materials in this thesis in whole or part should be addressed to:

Head
Department of Biology
Collaborative Science Research Building, 112 Science Place
University of Saskatchewan
Saskatoon, Saskatchewan S7N 5E2
Canada

OR

Dean
College of Graduate and Postdoctoral Studies
University of Saskatchewan
116 Thorvaldson Building, 110 Science Place
Saskatoon, Saskatchewan S7N 5C9
Canada

Acknowledgements

This work would not have been possible without the great supervision of my advisor, Dr. Chris Ambrose. As a biologist, his commitment and enthusiasm for scientific inquiry are unparalleled, and keep inspiring me all the time. As a mentor, his invaluable patience and support helped me succeed as a graduate student. I own all I achieved to Chris and cannot adequately express my gratitude to him.

I have benefited a lot from interactions with the members of my Ph.D committee, Dr. Daniel MacPhee, Dr. Yangdou Wei and Dr. Ken Wilson. I have received considerable support and valuable suggestions from them.

I have been fortunate to learn and work with a wonderful group of colleagues in the Ambrose Lab. I am particularly indebted to Yen Le, Liyong Zhang and Devon Ireland for numerous life suggestions and experiment ideas.

I wish to thank Dr. Eiko Kawamura from WCVM Imaging Centre and Dr. Guosheng Liu from Biology Department for their help with microscopy.

I am grateful to the Biology Dept for providing administrative and technical support.

Lastly, I wish to thank my parents and my wife for their endless love and support for helping me maintain a balanced existence. I certainly could not have completed this work without the support from my wife.

Abstract

Plant cells exhibit a variety of shapes and sizes that underlie their functions. These distinctive geometries are dictated by cell walls. The region adjoining two adjacent faces of a cell is termed a cell edge. Having varying degrees of curvature, cell edges play a fundamental role in defining the shape and geometry of the cell. Edge curvature is thus an important point of regulation in cell morphogenesis, and increasing evidence suggests a large compliment of proteins—edge proteins— resides at cell edges to control cell edge stiffness and curvature.

To understand cell edge properties, I identified additional edge proteins— Microtubule-Associated Protein 65-3 (MAP65-3), Phragmoplast Orienting Kinesin1 (POK1), BRICK1 (BRK1), Actin-related protein-2 (Arp2) and MUSTACHES. The project then focused on BRICK1 (BRK1), an actin nucleation-promoting factor.

Here, by examining BRK1 localization pattern and its regulation on the cell edges, I identified feedbacks between BRK1 and cell edges. On the one hand, cell edge curvature influences the accumulation of BRK1 to the edge. BRK1 exhibits a preferential enrichment at high-curvature cell edges. The localization pattern is gradually changed from uniform to specific enrichment as edge curvature change. On the other hand, BRK1 protein itself regulate cell edge through microtubule. In the absence of BRK1, fewer anticlinal microtubule bundles (AMBs) form, CMT tend to strongly align in parallel and change orientation more frequently. Collectively, these defects may explain cell lobe reduction in the *brk-1* mutant. Moreover, the *brk-1* mutants also exhibit cell plate orientation defects, which could result from failed asymmetric division.

Besides, additional functions were observed too. A series of preliminary results suggest an association between BRK1 and Plasmodesmata (PD). BRK1 signal localizes in the pit field at the anticlinal wall, where PD accumulate.

In summary, cell edges affect BRK1 localization through curvature changes, while BRK1 modulates cell edge curvature through MTs at both the cell division and cell expansion levels.

Table of Contents

List of Figures

List of Tables

List of Abbreviations

ACD: asymmetric cell division;

AIR9: auxin-induced in root cultures 9

AP: homogalacturonan;

Arp2/3: Actin-related protein 2/3

AMB: anticlinal microtubule bundle

BFA: brefeldin A;

BRK1: BRICK1;

CDZ: cortical division zone;

CLASP: Clip-associated protein;

CMT: cortical microtubule;

CSCs: cellulose synthase complexes;

CSI-1: cellulose synthase interactive protein 1

FRAP: fluorescence recovery after photobleaching

GCP2/3: gamma complex protein 2 and 3;

HG: homogalacturonan;

HSPC300: haematopoietic stem/progenitor cell protein 300;

KAC1: kinesin-like protein for actin-based chloroplast movement 1

Lat B: Latrunculin B;

Map65-3: MT-associated protein 65-3;

MAPs: MT-associated proteins;

MF: actin microfilament;

MTOC: MT-organizing centers;

MUS: MUSTACHES;

PD: plasmodesmata;

POK1: phragmoplast orienting kinesin1;

PPB: pre-prophase band;

RanGAP1: Ran GTPase activating protein 1

TBs: trans-facial MT bundles;

XGA: xylogalacturonan.

Chapter 1 General Introduction

Originating from small box-like precursors, plant cells acquire distinctive shapes, spanning from long cylindrical root hairs, jigsaw-shaped pavement cells, to branched trichomes. Those cell shapes, even subtle features of them, are appropriate for their bio-functions. For example, the hair-like shape of a root hair is thought to increase the surface area of the root for water and nutrient uptake. The establishment of plant cell shape is based on the coordinated interaction between cell wall tensile stress and turgor pressure (Kroeger et al., 2011; Guerriero et al., 2014). While isotropic turgor pressure would drive plant cells into spherical shapes, plant cells exhibit a wide variety of forms because of the anisotropic nature of the cell wall, which is mainly determined by the cell wall components. The pattern of cell wall deposition is in turn controlled in large part by the cytoskeleton, in particular, MTs.

1.1 Plant cell walls.

In contrast to animals, plant cells are encased by a relatively rigid but dynamic cell wall. To fulfill a wide range of functions, plant cells have evolved cell walls with incredibly complex structure and highly dynamic composition (Somerville et al., 2004; Cosgrove, 2005; Braybrook and Jonsson, 2016). Composed of a diversity of polysaccharides, structural proteins, and polyphenols, cell wall architecture can be regarded as a framework of cellulose microfibrils, cross-linked by hemicelluloses, nested in a pectin matrix. In this model, the rigid cellulose confers strength and directs the cell growth orientation, while hemicelluloses and pectin glue every constituent together and provides flexibility and growth permission (Braybrook and Jonsson, 2016). As a result, the cell wall determines cell growth through dynamic deposition and remodeling of wall components. Two types of cell walls exist, referred to as primary and secondary cell walls. Primary cell walls are relatively thin and flexible, and provide both basic structural support and flexibility for cell growth. The thicker and more durable secondary cell walls are deposited primarily following the cessation of cell expansion and provide mechanical support and protection to the plant cells (McNeil et al., 1984; Kumar et al., 2016).

Cellulose microfibrils are composed of β-1,4-linked glucan chains, which are synthesized by cellulose synthase complexes in the plasma membrane (Cosgrove, 2005). As the loading-bearing elements, cellulose microfibrils are long, stiff fibers with high tensile strength that create mechanical prohibition to cell elongation. In an elongating cell, cellulose microfibrils deposit in a

roughly transverse direction that is perpendicular to the elongation axis (Green, 1962). This orientation confers a mechanical bias to a single direction expansion (in this case, longitudinal) while constraining cell expansion in the lateral direction. Different from other wall polysaccharides and proteins, which are synthesized in the Golgi apparatus and transported to the plasma membrane for secretion into the apoplast, cellulose is synthesized and assembled directly at the plasma membrane by a rosette-shaped complex—cellulose synthase complexes (CSCs) (Lerouxel et al., 2006; Geisler et al., 2008). The CSC proteins are assembled and modified in the Golgi apparatus and then are delivered to the plasma membrane. CSC delivery relies on the cytoskeleton: actin microfilaments (F-actin) modulates the distribution of CSC–containing Golgi bodies, while MTs are responsible for marking the insertion site of CSCs proteins at the plasma membrane (Gardiner et al., 2003; Wightman and Turner, 2008; Crowell et al., 2009; Gutierrez et al., 2009).

After assembles on the plasma membrane, the CSC complex moves following linear tracks, extruding newly polymerized microfibrils into the cell wall (Morgan et al., 2013). While CSC mobility results from its own displacement during microfibril deposition, the trajectory of the CSC movement is dictated to a large degree by MTs. Specifically, the linear movement of CSCs co-aligns with the MT pattern inside the plasma membrane, and the change of MT arrangement leads to coordinated re-orientation of rosette complex tracking (Paredez et al., 2006; Gutierrez et al., 2009; Chan et al., 2011; Oda et al., 2015); Moreover, simultaneous observation of co-localization further confirms a direct link between CSC complexes and cortical MTs, which was reported to be bridged by CESA interactive protein 1 (CSI1) (Ledbetter and Porter, 1963; Paredez et al., 2006; Crowell et al., 2009; Gutierrez et al., 2009; Li et al., 2012). However, in the absence of MTs, CSCs continue their linear tracks for some time, probably due to the pre-existing cellulose in the cell wall (Himmelspach et al., 2003; Sugimoto et al., 2003; Wasteneys, 2004). Thus, MT arrangement controls cell expansion by guiding the direction of CSC movement and the corresponding orientation of cellulose microfibrils, although additional factors are also involved (Baskin, 2001; Wasteneys, 2004).

1.2 MT arrays in plants.

Since a plant cell's position is fixed and demarcated by a cell wall, the cell morphology is mainly determined by the orientation of cell division and directional cell expansion (Chakrabortty et al.,

2018). During interphase, MTs line on the plasma membrane and form the cortical MT array, which is responsible for guiding CSCs to direct cellulose microfibril orientation and cell expansion patterns (Figure 1.1 A). During mitosis, the division plane position and its orientation are already forecasted by a distinguished MT array structure — the pre-prophase band (PPB) (Figure 1.1B) (Wasteneys, 2004). At late G2 stage, with the assistance of F-actin, parallel cortical MTs gradually narrow down to form a dense ring-like PPB encircling the nucleus (Takeuchi et al., 2016). By modulating the biochemical composition locally, the PPB creates a "memory" for the future cell plate insertion site, which is termed the cortical division zone (CDZ) (Karahara et al., 2009; Spinner et al., 2013; Zhang et al., 2016; Schaefer et al., 2017). The CDZ is established and maintained by selectively depleting negative markers such as F-actin and KAC1(kinesin-like protein for actin-based chloroplast movement 1) and recruiting positive markers such as AIR9 (auxin-induced in root cultures 9), PHRAGMOPLAST ORIENTING KINESIN 1 and 2 (POK1 and POK2), Ran GTPase activating protein 1 (RanGAP1) and TANGLED (Cleary et al., 1992; Buschmann et al., 2006; Muller et al., 2006; Vanstraelen et al., 2006; Walker et al., 2007; Xu et al., 2008). Interestingly, the establishment and maintenance of CDZ requires different protein complexes, indicating a progressive maturation of the CDZ.

Even before PPB formation, the nucleus migrates from the periphery to the center of the future PPB location, and the failure of nucleus movement leads to cell division plane defects (Panteris et al., 2006; Masoud et al., 2013). The PPB disassembles coincident with nuclear envelope breakdown and spindle formation. Following nuclear division, the cytokinetic MT array — the phragmoplast— forms between daughter nuclei and deposits wall material in the cell center to build a cell plate (Figure 1.1). The cell plate keeps expanding until it connects with the parental wall to form a new wall. The final position and orientation of the new wall is based on the interaction between the expanding phragmoplast and former PPB site at the cortex (Rasmussen et al., 2013).

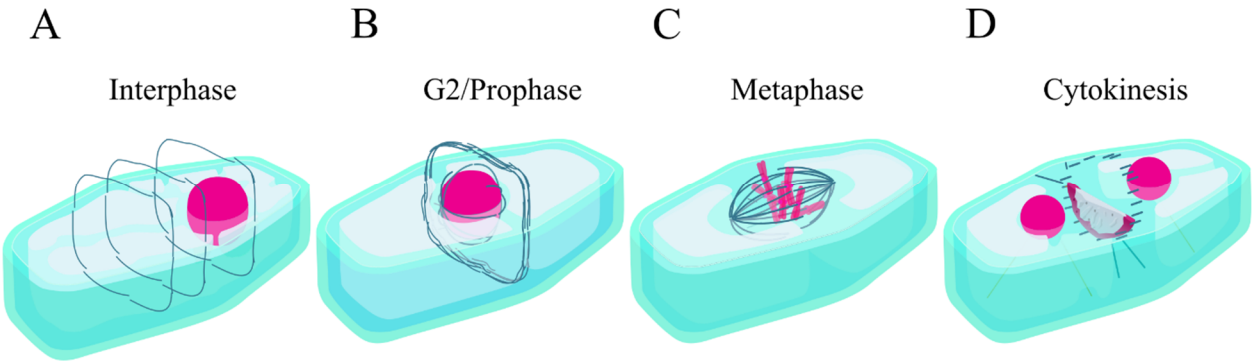

Figure 1.1 Schematic image of MT arrays in different cell cycle stages.

Navy blue lines represent MTs. Modification is done by Z.C based on SVG file on plant cell cycle from Kelvinsong [CC0], from Wikimedia Commons.

1.2.1 MTs and cell expansion.

Cell expansion is based on a delicate balance between turgor pressure and cell wall extensibility. As turgor pressure is isotropic, the plant cell wall locally yields to the stress by selectively loosening or stiffening the cell wall. This process results from either changing of cell wall composition or remodeling of the cellulose microfibril orientation (Sapala et al., 2018). By directing the cellulose synthase complex, MT determines the deposition pattern of the cellulose microfibrils. Since the cellulose microfibrils have anisotropic tensile strength, their pattern can resist parallel force and promote orthogonal stress, contributing to the formation of cell shape (Baskin, 2005). MTs, in turn, are highly responsive to the numerous mechanical stresses inherent to multicellular organisms with complex cell and tissue geometries (Hejnowicz et al., 2000; Hamant et al., 2008). Specifically, when a cell experiences tension (i.e., it is pulled), MTs become aligned parallel to the principal direction of this tensile stress (Hamant et al., 2008; Uyttewaal et al., 2012; Sampathkumar et al., 2014a). This alignment of MTs then generate cellulose microfibrils parallel to the tension to dampen cell elongation and tissue weakening.

1.2.2 MTs and cell division plane orientation.

The cell plane orientation is determined by both intrinsic and extrinsic factors. The extrinsic factors include mechanical stress directions, cell geometry, and polarity cues. The information from those factors is translated by MTs to allow the appropriate orientation of cell division (Uyttewaal et al., 2012; Facette et al., 2018; Martinez et al., 2018). Several theories were put forward as early as the

19th century to explain cell division plane selection. Generally, without internal or external cues, cell plane was found to bisects the long axis of the cell to inserts an anticlinal wall with the less possible interface area (Hofmeister, 1863; Sachs, 1878; Errera, 1886). Moreover, newborn cell plane was further found to be prohibited to connect at the same point as a neighboring cell, that is, four-way junction avoidance (Flanders et al., 1990). The molecular mechanism behind those geometrical rules is proposed to be through the organization of MTs (Lloyd, 1991; Besson and Dumais, 2011). Cytoplasmic strands enriched with MTs helps to relocate the nucleus during cell division and then determine the division plane.

1.3 Terminologies for cell geometry.

From a geometrical standpoint, the wall-encased plant cell can be simplified as a polyhedron consisting of faces, vertices, and edges. Periclinal walls are the faces that are parallel to the surface of the organ, while the anticlinal walls are perpendicular to the surface of the organ. The region that adjoins two cell faces is defined as the cell edge, while the vertices correspond to the areas that three or more faces intersect (i.e., the cell corners) (Figure 1.2). In this chapter, I will classify cell edges according to the same parameters as for cell faces. Therefore, like periclinal walls, periclinal edges are oriented parallel to the organ face, and anticlinal edges are perpendicular to the organ surface. Moreover, considering there are two types of periclinal edges in both root and hypocotyl cells, I define the one crossing a periclinal wall as the transverse periclinal edge and the one parallel to the periclinal wall as the longitudinal periclinal edge.

Among the geometrical features, curvature is one of the most important properties of the cell edge (Ambrose and Wasteneys, 2008; Ambrose et al., 2011; Chakrabortty et al., 2018). Cell edge curvature often changes over time. I define the curvature level in a geometrical way: the curvature is equal to the reciprocal of the radius of a circle at a given region of wall. Theoretically, the curvature level is high if radius is small, and low if radius is big. After cytokinesis, the cell plate fuses with the parental wall at a 90-degree angle, creating new cell edges (Ambrose et al., 2011). These newly formed cell edges are sharp and thus they have high curvature (Figure 1.2C top). During subsequence cell expansion, cell edges often become gradually more rounded (i.e., low curvature) as the cell wall stretches and deforms to coordinate cell growth (Figure 1.2C bottom). Importantly, the diversity of plant cell shape requires that many cell edges must remain sharp at

maturity. This suggests that there must be some cellular factors to monitor and control cell edge curvature during cell expansion and differentiation.

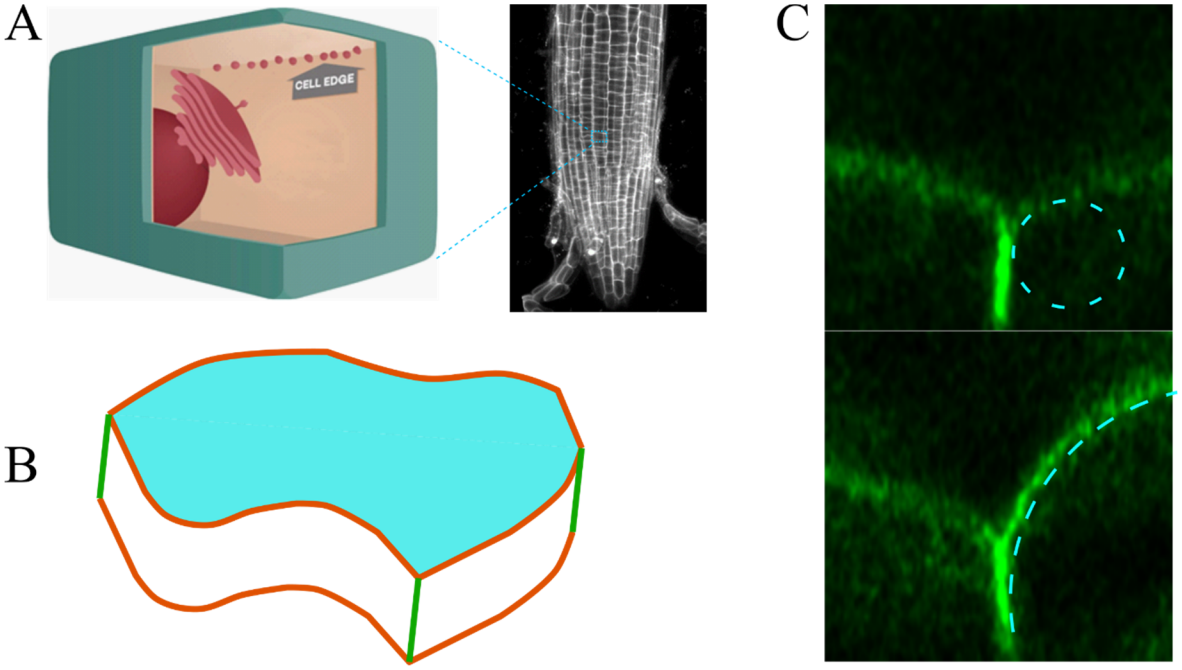

Figure 1.2 Cell edge and edge types in leaf cells.

A illustrates the cell edge and cell edge proteins (the pink ball at the edge) in the root. The image is adapted from (Rahni and Birnbaum, 2016). B shows cell edge types from leaf cell: orange lines mark periclinal edge while green ones mark anticlinal edges. The blue region indicates the periclinal wall while blank regions indicate the anticlinal wall. C is a cross-section view of periclinal cell edges in different cell stages: upper panel shows new-born edges with higher curvature while the bottom one shows mature edges with lower curvature.

So far, the geometrical modulation of cell edge on cell growth is mainly through the influence of MT organization (Ambrose et al., 2011).

1.4 Cell edge, MTs and cell edge proteins.

Just as cytoskeletal organization dictates the geometry of a cell, this geometry, in turn, has a major impact on the cytoskeletal organization. This phenomenon has been studied with respect to the establishment and functioning of cell edges (Ambrose et al., 2011). The study revealed that for newly formed cell edges, their high curvature acts as a physical barrier to block MTs from growing across into the adjacent cell face, which leads to MTs catastrophe when MTs approach it. This

barrier effect ensures MTs align parallel to the sharp edge, which then promotes cell elongation (Ambrose et al., 2011). When cells step into differentiation and expansion, the barrier effect is gradually lost as cell edge become rounded, which allows MTs to grow across onto the neighboring cell face.

To grow around the sharp cell edge, MTs form bundles and particular MT-associated proteins provide extra stabilization to it at the edge (Ambrose and Wasteneys, 2011; Ambrose et al., 2011). The MT bundles spanning between cell walls are termed as Trans-facial MT bundles (TBs) (Ambrose et al., 2011). The stabilization of TBs assures the cell maintains its edge curvature in the undifferentiated state (Ambrose et al., 2011). Therefore, cell edges impart the geometrical information to regulate cell growth through modulating MT.

As its advantage was gradually recognized, mathematical and computational modeling was widely applied to plant morphogenesis research (Eren et al., 2012; Deinum and Mulder, 2013). Started with the CMT alignment model, modeling simulation confirmed the interaction between cell geometry and MTs (Ambrose et al., 2011; Chakrabortty et al., 2018). Therefore, the feedback loop between cell shape and MTs creates a system capable of responding to signals from both inside and outside the cell.

Cell edge proteins are the proteins that specifically enriched at the cell edge. So far, three cell edge proteins have been reported and their function to edge mechanism investigated (Ambrose and Wasteneys, 2011; Ambrose et al., 2011; Kirchhelle et al., 2016).

1.4.1 Clip-associated protein (CLASP).

The first identified cell edge protein, CLASP, belongs to an evolutionarily conserved family of MAPs that promote MT stabilization (Ambrose and Wasteneys, 2008; Inoue et al., 2000; Lemos et al., 2000; Maiato et al., 2003). By preferentially binding to the plus end of MTs, CLASP displays a broad range of functions in cell division and cell morphogenesis by stabilizing MT (Mimori-Kiyosue et al., 2005; Hannak and Heald, 2006; Lansbergen et al., 2006; Sousa et al., 2007; Ambrose and Wasteneys, 2008). Among those functions, an intriguing role of CLASP emerged as a cell edge protein with preferential targeting to newly-formed cell edges. Generally, after cell division, CMTs arrange longitudinally (perpendicular to future cell expansion orientation) to facilitate the exit of cell division. However, in meristematic cells, TBs tend to orient longitudinally

and thus count against cell expansion orientation (Ambrose et al., 2011). In meristematic cells, CLASP is enriched at the newly formed cell edges (with high edge curvature), promoting TB formation by stabilizing in-coming MTs to allow them to pass the cell edge (Figure 1.3A). Therefore, through the selective distribution of CLASP (and other components), the cell can re-organize the MT array pattern to facilitate cell morphogenesis (Figure 1.3) (Ambrose et al., 2011).

1.4.2 Gamma complex protein 2 and 3 (GCP2/3).

Among the different type of tubulins, γ-tubulin plays a critical role in MT nucleation and organization (Job et al., 2003; Wiese and Zheng, 2006; Raynaud-Messina and Merdes, 2007). MT nucleation is initiated by γ-tubulin at the microtubule-organizing center (MTOC), such as centrosome in mammals or spindle pole body in yeast (Pereira and Schiebel, 1997). In plants, instead of binding specifically to the minus end of MTs, γ-tubulin distributes on all MT arrays (Liu et al., 1993). To initiate MT nucleation, a ring-like structure (γ-tubulin ring complex, or γTuRC) is formed and consist of γ-tubulin, γ-tubulin complex proteins 2 and 3 (GCP2/3) and other GCPs (Liu et al., 1994; Binarova et al., 2006; Pastuglia et al., 2006). In interphase cells, GCP2 and GCP3 are localized in the cell cortex along CMTs, where they nucleate MTs off of pre-existing ones to facilitate normal CMT orientation (Erhardt et al., 2002; Seltzer et al., 2007; Nakamura and Hashimoto, 2009). In root meristems and recently-divided leaf cells, GCP2/3 accumulates at the nuclear envelope and along the newly formed cell edge, where it nucleates MTs (Ambrose and Wasteneys, 2011). The newly nucleated MTs then grow away from the cell edge, thereby forming polarized CMT arrays that are perpendicular to the cell edge (Figure 1.3B). The pattern of GCP2/3 at cell edge is identical to that of CLASP, although their temporal dynamics differ: GCP2/3 appear at cell edges prior to CLASP and disappear earlier. This change in edge protein composition corresponds to a change in MT growth direction with respect to the cell edge: early on, MTs grow away from the new edge, while later, they grow predominately toward the new edge. All of these indicate a time-dependent interplay between CLASP, GCP 2/3 and CMT organization, presumably to help control cell edge maturation, composition, and curvature (Ambrose and Wasteneys, 2011).

1.4.3 RAB-A5c.

RAB-A5c is a plant Rab guanosine triphosphatase (Rab GTPase), which regulates membrane trafficking (Woollard and Moore, 2008). Through GTP/GDP-bound state switching, individual Rab protein bind with a certain membrane. RAB-A5c exhibits localization in both the trans-Golgi

network (TGN) and cell edges, which makes it distinguished from other members. The edge localization is GTP binding-dependent, and inhibition of RAB-A5c leads to deformation of cell geometry, such as radial swelling and wall softening (Kirchhelle et al., 2016). It's remained unknown for RAB-A5c's specificity to edge mechanism. However, based on current results, it's been suggested that RAB-A5c could mediate specialized membrane trafficking to locally regulate cell edge stiffness, which would favor anisotropic growth at the global cellular level (Kirchhelle et al., 2016).

As a geometric domain, cell edge is shown to have unique property to deal with the stress, presumably through edge curvature change (Ambrose and Wasteneys, 2011; Kirchhelle et al., 2016). Since the edge curvature determines the passability of the MT, one path to regulate edge curvature is carried on by MT nucleator GCP2/3 and stabilizer CLASP. Through stabilizing MTs at the edge, both GCP2/3 and CLASP help to constrain the boxy cell in the meristematic state by creating mixed CMT arrays (Ambrose and Wasteneys, 2011; Ambrose et al., 2011).

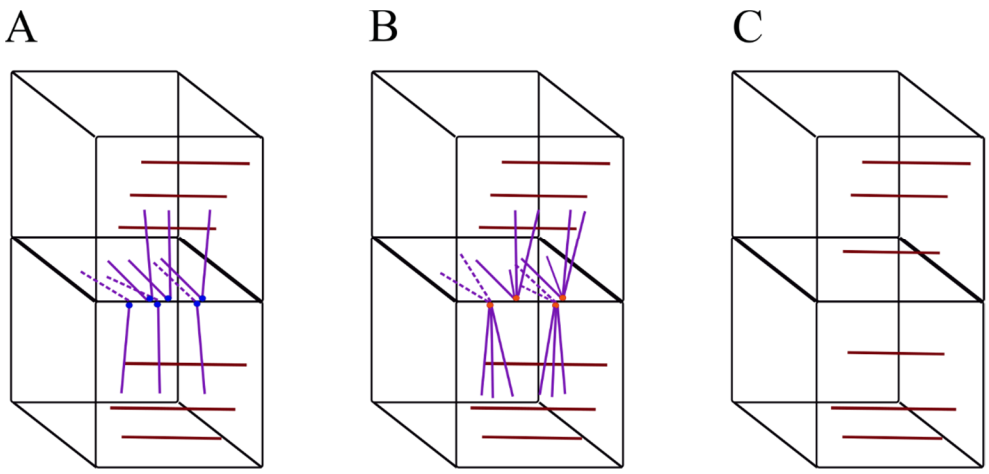

Figure 1.3 CLASP and GCP2/3 localization at the newly-formed cell edges.

The image is adapted from (Ruan and Wasteneys., 2014). A, CLASPs (blue dots) at cell edge stabilize edge-crossing MTs to form TBs (purple lines); B, GCP2/3 (orange dots) at cell edge nucleates CMTs to form TBs (purple lines). In both A and B, the formation of TBs prohibits cell growing longitudinally. C, without assistant from certain edge proteins, MTs cannot form TBs due to the sharp cell edge induced encounter-based catastrophe. Cells will grow longitudinally. Brown lines are CMTs.

Considering that the CLASP/GCP and RAB-A5c pathway are independent of each other (Kirchhelle et al., 2016), it's conceivable that multiple mechanisms containing other edge components participate in the regulation of cell edge mechanical properties, especially the edge curvature. Based on current knowledge, the regulation of cell edges on morphogenesis is through modulating cytoskeleton and other system and this modulation is assisted by edge proteins such as GCP2/3 and CLASP. After cell division, the incipient cell edge is sharp, thereby exhibiting a higher edge curvature. Since its relative rigid character, CMT crossing the edge increase the MT catastrophe frequency because it needs extra energy for bending. In that case, cell expansion will be perpendicular with new edge (Figure 1.3C). While in the mature cells, cell edge becomes rounded and thus CMTs can pass. Considering this complexity, cell edges may act as a dynamic spatial domain with many more protein components involved.

1.5 Themes and research objects.

This project is a part of Dr. Ambrose's NSERC project—Subcellular Dynamics, Cell Morphogenesis, and Organ Formation in Plants. The theme of the project is to determine the role of cell edges in plant morphogenesis and understand the regulation mechanism of cell edge components on cell edge formation and development.

To start the main project, I first obtained published Arabidopsis marker lines for edge candidate proteins and run a large-scale screen. After screening the subcellular localization of those candidate lines, I identified five candidates. Given that no research has been conducted on actin-related cell edge protein yet, I then focused on functional characterization of *Brk1*. I first investigate the subcellular localization pattern and dynamics of BRK1 and its relationship with cell edge curvature. To illustrate BRK1's influence on cytoskeleton and the cytoskeleton-associated cell morphogenesis, I investigated the distribution and dynamics of both F-actin and MT. Finally, I investigated the biological function of BRK1 on cell wall and the mechanisms underpinning. The goals of this thesis are as follows:

- To assess the relationship between CMT arrangement and catastrophe;
- To identify and characterize more cell edge proteins;
- To determine the spatial-temporal localization of BRK1;

- To investigate the change of cytoskeleton in the *brk-1*mutant and the mechanisms underpinning;
- To investigate the biological function of BRK1 on cell wall, to be specific, its association with PD.

Chapter 2 BRK1 localization is associated with cell wall curvature

2.1 Introduction

2.1.1 Actin cytoskeleton and actin nucleating proteins.

The actin cytoskeleton is essential for numerous fundamental eukaryotic cell activities such as cell morphogenesis, cytokinesis and cell motility (Pollard and Cooper, 2009). In terms of plant-specific functions, actin mediates long distance transport, organelle positioning, plasmodesmata regulation, and fungus resistance (White et al., 1994; Ketelaar et al., 2002; Romagnoli et al., 2007). Actin regulates cellular morphogenesis mainly through actin-dependent vesicle trafficking (Hepler et al., 2001; Smith and Oppenheimer, 2005; Zerzour et al., 2009; Yanagisawa et al., 2015). Unlike animal cells using MTs, plant cells employ F-actin as the tracks for long-distance transport of organelles, such as secretory vesicles containing cell wall material.

Actin primarily exists as monomeric globular subunits (G-actin), which polymerize into filamentous actin (F-actin), also known as actin microfilaments. To assemble thermodynamically unfavorable F-actin, cells recruit actin nucleating proteins such as Formins and the Arp2/3 (actin-related protein 2/3) complex (Deeks et al., 2002; Pollard and Beltzner, 2002). While Formins form unbranched F-actin, Arp2/3 nucleates on the existing F-actin to form branched F-actin (Pollard and Beltzner, 2002).

2.1.2 BRICK1/HSPC300 and function.

Polymerized by the Arp 2/3 complex, actin is under tight spatial and temporal regulation (Bompard and Caron, 2004). The Arp2/3 complex activity, in turn, is regulated by the suppressor of cAMP receptor (SCAR)/ WASP (Wiskott-Aldrich syndrome protein)-family verprolin homology protein (WAVE)proteins (Pollard and Borisy, 2003). By binding and triggering a conformational change, SCAR/WAVE can lock the Arp2/3 complex into its activated state (Escobar et al., 2010). Acting as a hub, SCAR/WAVE orchestrate various signaling pathways, such as linking signals from Rac GTPase family and then converting it to activate Arp2/3 (Ismail et al., 2009; Chen et al., 2010). In animals, the SCAR/WAVE complex is composed of five subunits: Sra1, Nap1, Abi1, SCAR/WAVE, and Brick1/ haematopoietic stem/progenitor cell protein 300 (HSPC300) (Ismail et al., 2009; Chen et al., 2010; Linkner et al., 2011).

Encoding a small protein, BRK1/HSPC300 is highly conserved in eukaryotes. So far, no recognizable functional motif (including any predicted signal peptides for secreted proteins) has

been identified in BRK1 in any organisms (Frank and Smith, 2002). In the non-plant field, the explorations of BRK1/HSPC300 focus on its precursor role in Scar/WAVE-complex assembly whereas the research in plants is mainly related to its functions in the F-actin-remodeling-dependent process such as cytokinesis and cell morphogenesis (Linkner et al., 2011). In vertebrates, the majority of HSPC300 exists in the cytosol as trimers, which is in contrast to the other four components, which remain in the SCAR/WAVE complex at the plasma membrane (Gautreau et al., 2004). Moreover, an *in vitro* experiment confirmed that the Arp2/3 complex still can be stimulated by SCAR/WAVE complex without HSPC300 (Innocenti et al., 2004). All of these suggest other functions of HSPC300, which might be independent of the SCAR/WAVE complex.

In higher plants, especially in Arabidopsis, the homologous genes of SCAR/WAVE complex have been identified (Basu et al., 2004; Deeks et al., 2004; Zimmermann et al., 2004; Dyachok et al., 2008). Despite extensive research on SCAR/WAVE complex in both plants and animals, the function of *Brk1* is the least understood.

The *Brk1* gene was characterized in both Maize and Arabidopsis (Frank and Smith, 2002; Le et al., 2006). In both species, *Brk1* is globally expressed with the highest gene expression levels in expanding leaves and lower levels in mature tissues such as mature leaves in maize, flower buds and root tip in Arabidopsis (Frank and Smith, 2002; Djakovic et al., 2006; Dyachok et al., 2008). Subcellular analysis localized BRK1 on the plasma membrane, and the localization is SCAR-dependent: mutations in *SCAR* lead to a reduction of BRK1 at its localization (Dyachok et al., 2008; Yanagisawa et al., 2018). In Arabidopsis, BRK1 specifically enriches to sites of heavy cell wall material deposition, such as the tips of growing trichomes, pavement cell lobes and three-way cell junctions (Dyachok et al., 2008). In maize, the localization patterns are similar, but with BRK1 also exhibiting localization at the contact site between subsidiary cells and guard mother cells (Facette et al., 2015).

2.1.3 BRICK1 and plant cell morphogenesis.

In general, F-actin modulates cell wall composition and patterning by targeted vesicle trafficking (Szymanski and Staiger, 2018). As an activator of the actin nucleation system, BRK1 was found to promote asymmetric division and polar growth and then participate in cell morphogenesis (Frank and Smith, 2002; Le et al., 2006; Dyachok et al., 2008). So far, current research focuses on

BRK1's role in asymmetric cell division, promoting of cell-cell adhesion and lobe formation in pavement cells, and the initiation and maintenance of trichome. These three are discussed in turn below.

2.1.3.1 BRK1 and asymmetric division in maize.

Brick1 (Brk1) gene was isolated because of its role in maintaining the proper asymmetric division of stomatal subsidiary cells. For monocot plants, stomatal development proceeds in an invariant division sequence: two asymmetric divisions generate the guard mother cell (GMC) and subsidiary mother cell (SMC) and a following symmetric division produces the guard cells (Figure 2.1 A-C) (Hepworth et al., 2018). After the "entry division", the new GMC emanates inductive cues toward the epidermal cells flanking its both sides (Figure 2.1 A). The flanking cells then become SMCs, and their nucleus migrate to the region in contact with the GMC. The position of the nucleus next to the GMC defines the region of asymmetric division, which results in a small subsidiary cell (SC) next to the GMC, and a large pavement cell (PC) (Figure 2.1B and C).

During this process, a recessive mutant of *Brick1* was isolated due to its abnormal cell pattern of subsidiary cells. The abnormal subsidiary cells in the *brk1* mutant are due to the failure of polarization of SMC, which show less F-actin enrichment in actin patch and few nuclei associating with actin patch (Frank and Smith, 2002). As actin depolymerizes or actin patch disappears, the percentage of properly oriented PPB decrease too, indicating a close relationship between two cytoskeletons. Further research on subsidiary cells in the *brk-1* mutant showed that MTs surround the nucleus globally and fill in the cytoplasmic area that used to be occupied by actin patch in wild type (Panteris et al., 2006). Interestingly, the BRK1 localizes at the contact site of GMC and SMCs and forms a patch-like pattern (Facette et al., 2015). The BRK1 patch appears even before the nuclear migration and the maintenance of BRK1 patch even do not require actin patch (Facette et al., 2015). The mechanism of BRK1 function in SMC polarity remained unknown until recent further functional characterization of BRK1 and the SCAR complex: after the SMC receives a cue from the GMC, the SCAR/WAVE complex (with associated BRK1) in the SMC accumulates at the GMC-SMC contact site and sequentially targets several additional factors to this site. These factors are PANGLOSS2 (PAN2), PANGLOSS1 (PAN1) and Rho of Plants (ROP) GTPases (Facette et al., 2015). The PAN1-dependent activation of ROP physically interacts with the SCAR

complex, which leads to an actin patch at the GMC-SMC contact site to cue nuclear migration there.

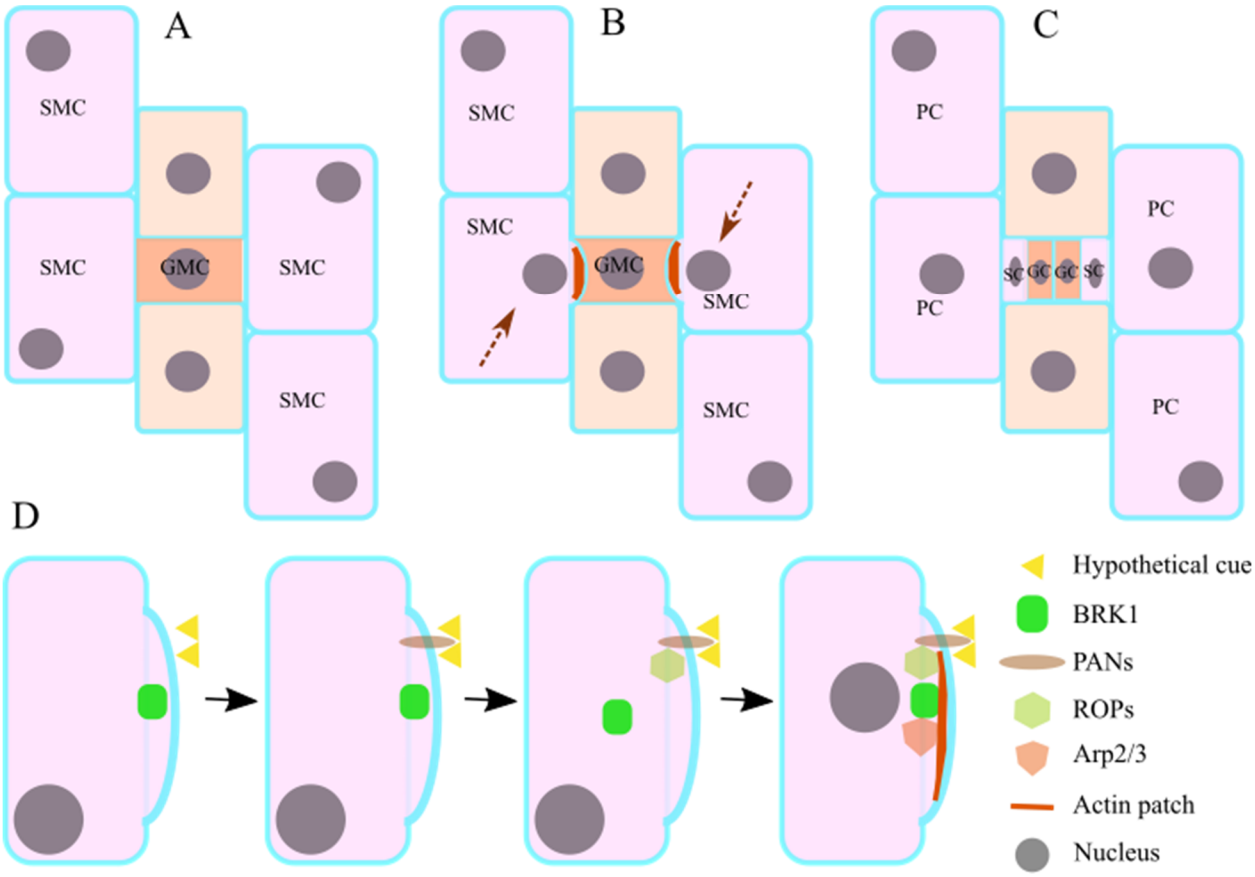

Figure 2.1 Hypothesized role of BRK1 in SMC polarization in maize.

A to C schematic depicting cellular events during SMC polarization in maize: (A) GMC emit cues to flanking SMC. (B) Guided by a hypothetical cue from GMC, the SMC is polarized, accompanied with nucleus migration (migration direction marked by brown arrow). (C) The asymmetric division completed. (D) The proposed molecular model for SMC polarization: the BRK1 containing SCAR system polarizes at the contact site between SMC and GMC. PANs recruit and activate ROPs, which further activate the BRK1 containing SCAR system. Activated BRK1 activates Arp2/3 to polymerize F-actin, which promotes nuclear migration towards the GMC.

In contrast with this well-characterized system in maize, the function of BRK1 on Arabidopsis guard cell differentiation remain unknown.

2.1.3.2 BRK1 and cell adhesion.

In animals, HSPC300 promotes cell adhesion by enforcing cell-cell contact (Yamazaki et al., 2007). With regard to plants, previous analysis of leaf cell wall junction in the *brk-1* mutant showed defects in both maize and Arabidopsis: in maize, the thickening of periclinal wall junction lacks in another SCAR/WAVE mutant—a *Sra* mutant with similar phenotype as *brk-1* while the Arabidopsis *brk-1* mutant has failed adhesion between cotyledon epidermal cells, leading to the appearance of holes at the lateral junctions between three cells (a.k.a three-way junction) (Djakovic et al., 2006) and in roots these same regions are swollen and have altered wall composition, although no holes form (Dyachok et al., 2008). All these junction defects indicate a weak cell wall junction between neighbor cells, which could result from the change of wall materials gluing the junction. Consistent with this, BRK1-YFP in plants is enriched at the three-way junctions (Yamazaki et al., 2007; Dyachok et al., 2008). Similar to the thinner junctions in the outer periclinal wall in maize, all these morphology defects correspond to weak cell adhesion (Frank and Smith, 2002; Dyachok et al., 2008).

Considering its function on actin nucleation in Arabidopsis, BRK1 was proposed to polymerize actin for the delivery of vesicle containing wall materials to the three-way junctions for further fortify these naturally weaker regions (Dyachok et al., 2008).

2.1.3.3 BRK1 and trichome formation.

Through governing cell polarity, BRK1 exerts a critical influence on the development of trichome in Arabidopsis (Dyachok et al., 2008; Yanagisawa et al., 2015). With strict spatial-temporal regulation, Arabidopsis trichome development undergoes three stages—initiation, spacing, and morphogenesis (Szymanski et al., 1998). F-actin plays a critical role in the morphogenesis stage by establishing and maintaining the complex cell polarities required for proper trichome elongation (Szymanski, 2000). In these cells, F-actin aligns to thick bundles along the long axis of the trichome branch from base to the apical dome (Szymanski, 2000; Le et al., 2006). By blocking the genes encoding actin-related proteins, such as components of Arp 2/3 and its regulators, plants show impaired trichome shape (Frank and Smith, 2002; Le et al., 2006). As an activator of Arp 2/3, BRK1 participates in actin regulation, thus the morphogenesis of trichome. Distinctive phenotype was observed in the *brk-1* mutants: the prickle hairs and macrohairs of maize leaves become shorter and blunter, and the trichome in Arabidopsis either fail to initiate or often distorted

and swollen (Frank and Smith, 2002; Le et al., 2006). The research about BRK1 function on trichome development mainly focus on Arabidopsis: it is reported that BRK1 localized at the tip of the newborn trichome branches and either blocking or enhancing the BRK1 expression leads to aberrant trichome (Djakovic et al., 2006; Dyachok et al., 2008). Consistent with BRK1's function to accumulate F-actin, *brk1* mutant show aberrant F-actin bundle arrangement, and the change becomes more obvious as the trichome continues to expand (Djakovic et al., 2006).

2.1.3.4 BRK1 and cell lobe formation.

In numerous plants, the epidermis produces pavement cells with wavy anticlinal walls. Since adjacent cells interlock with each other, one pavement cell has multiple wall undulations (i.e., lobes), and each lobe has a concave side and convex side. The establishment of the interdigitation has been proposed to occur due to varied wall growth rates and directions (Wasteneys and Galway, 2003; Fu et al., 2005).

This wall growth heterogeneity, in turn, is proposed to be directed by the dynamic change of cytoskeleton pattern: F-actin accumulates at lobe emerging site to form actin patch, presumably facilitating the delivery of cell wall materials needed for wall expansion while MT array converge transversely in the convex side of lobe to restrict the wall expansion via guiding stiff cellulose microfibrils deposition (Wasteneys and Galway, 2003; Fu et al., 2005; Sampathkumar et al., 2013). Mutation or pharmacological inhibition of both cytoskeletal systems results in defective or absent cell lobing (Panteris and Galatis, 2005).

According to current knowledge, the molecular mechanism behind this cytoskeletal patterning is governed by two antagonistic ROP signaling pathways, where ROP4 recruits F-actin to promote the lobe formation while ROP2 recruits MT to restrict lateral cell expansion to form the indentation (Wasteneys and Galway, 2003; Fu et al., 2005).

The critical role of F-actin in lobe formation is supported by the presence of lobing defects during drug-induced actin depolymerization, and in a number of actin-related mutants with deficient lobe formation, including *brk1* mutants in both maize and Arabidopsis (Frank and Smith, 2002; Panteris and Galatis, 2005; Djakovic et al., 2006; Dyachok et al., 2008). In the maize mutant, the actin patch found in the concave side of the lobe is not present (Frank and Smith, 2002). Consistently, the formation of the lobe is completely blocked in the pavement cells, whereas the cells in the

internal tissue layers (for example, mesophyll) are not affected (Frank and Smith, 2002). Interestingly, *Brk1* gene was shown to act non-cell-autonomously (Frank et al., 2003). Specifically, by creating plants having a mosaic of epidermal cells with wild type or *brk1* identities, this paper showed that a wild-type cell could rescue nearby *brk1* cells. Relevant to my thesis, this suggests a possible pathway of BRK1 traveling between neighboring cells through plasmodesmata (Frank et al., 2003). The research on Arabidopsis shows similar results: the lobe formation is reduced in pavement cell in the *brk1* mutant; F-actin distribution in cells is less dense, and the F-actin intensity in lobe tip reduces (Djakovic et al., 2006; Le et al., 2006). Subcellular analysis of BRK found that BRK mainly enriched at the three-way-adjunction in both root and pavement cells, where space could be filled with cell wall materials through actin-dependent trafficking (Dyachok et al., 2008). Moreover, considering that F-actin is depleted in the cell corner in the *brk1* mutant, the localization of BRK may suggest an important role of three-way-adjunction in pavement lobe formation.

The establishment of morphology is based on both orientated cell division and directional expansion, which are under the regulation of cytoskeleton (Smith and Oppenheimer, 2005). Therefore, serving to activate actin nucleator system, BRK1 protein in the plant cell is directly involved in morphogenesis but detailed information about the exact mechanism remains unknown.

Given that cell edges function as structure domain, I hypothesized that in addition to the identified cell edge proteins, new edge proteins can be identified by examining the localization patterns of fluorescent protein-tagged candidate proteins. Moreover, the localization of edge proteins may be affected by cell edge geometry.

2.2 Result

2.2.1 Identification of five new cell edge proteins.

In previous work, Dr. Ambrose identified and characterized the first two cell edge proteins, CLASP, and GCP2/3, which exhibit cell edge localization. Furthermore, during analysis, both edge proteins were hypothesized to represent functional cellular domains, containing other edge components. In order to identify additional proteins at the cell edge, I screened fluorescent reporter lines of Arabidopsis from four functional categories known to determine plant cell shape: microtubule-associated proteins, F-actin organization proteins, endomembrane trafficking

proteins, and cell wall formation related proteins. Twenty reporter lines were obtained from other research groups (Table 2.1), and their localization was examined in root meristematic cells.

Table 2.1: Genes used for screening.

Genes	Category	Biological role	Reference
AtAIR9 (AT2G34680)	microtubule associated protein	Localization: PPB and cell division site Role: cell plate maturation	(Buschmann et al., 2006)
AtARP2 (AT3G27000)	actin organization protein	Localization: plasma membrane Role: branch actin nucleation	(Zhang et al., 2013a)
AtAURORA1 (AT4G32830)	microtubule associated protein	Localization: PPB Role: PPB dynamics	(Demidov et al., 2005)
AtBRK1 (AT2G22640)	actin organization protein	Localization: plasma membrane Role: branch actin nucleation	(Dyachok et al., 2008)
AtCESa6 (AT5G64740)	cell wall formation related protein	Localization: cell wall Role: cell wall formation	(Panteris et al., 2015)
AtFRA1 (AT5G47820)	microtubule associated protein	Localization: MTs associated Role: MT-dependent vesicle trafficking	(Zhu et al., 2015)
AtKAC1 (AT5G10470)	microtubule associated protein	Localization: plasma membrane and cell plate Role: phragmoplast guidance	(Vanstraelen et al., 2006)

AtKINUa (AT1G12430)	microtubule associated protein	Localization: PPB Role: PPB and cell cycle regulation	(Quan et al., 2008)
AtKTN1 (AT1G80350)	microtubule associated protein	Localization: MT associated Role: MT severing	(Burk et al., 2001)
AtMAP65-3 (AT5G51600)	microtubule associated protein	Localization: membrane and phragmoplast Role: phragmoplast integrity and cell plate formation	(Steiner et al., 2016)
AtMUS (AT1G75640)	cell wall formation related protein	Localization: cell plate Role: stomatal bilateral symmetry	(Keerthissinghe et al., 2015)
AtPLP3a (AT3G50960)	cell wall formation related protein	Localization: MT binding Role: cell division	(Castellano and Sablowski, 2008)
AtPLDδ (AT4G35790)	cell wall formation related protein	Localization: plasma membrane Role: signal transduction	(Angelini et al., 2018)
AtPOK1 (AT3G17360)	microtubule associated protein	Localization: plasma membrane and CDZ Role: phragmoplast guidance	(Muller et al., 2006)
AtROP11 (AT5G62880)	actin organization protein	Localization: plasma membrane Role: secondary wall pit formation	(Oda and Fukuda, 2013)
AtSEC3A (AT1G47550)	endomembrane trafficking protein	Localization: plasma membrane Role: exocytosis regulation	(Bloch et al., 2016)

AtSPR1 (AT2G03680)	microtubule associated protein	Localization: MT binding Role: cell expansion	(Nakajima et al., 2004)
AtTANGLED (AT3G05330)	microtubule associated protein	Localization: plasma membrane and CDZ Role: division plane establishment and/or phragmoplast guidance	(Walker et al., 2007)
AtTOR1 (AT4G27060)	microtubule associated protein	Localization: MT binding Role: CMT orientation regulation	(Buschmann et al., 2004)
AtTPLATE (AT3G01780)	endomembrane trafficking protein	Localization: cell plate and cell division site Role: cell plate anchoring	(Van Damme et al., 2006)

Of the 20 fluorescent reporter lines, I identified five new cell edge proteins, and they are Microtubule-Associated Protein 65-3 (MAP65-3), Phragmoplast Orienting Kinesin1 (POK1), BRICK1 (BRK1), Actin-related protein-2 (Arp2) and MUSTACHES (Figure 2.2). In roots, these edge proteins mainly enriched at the outer periclinal edge, with varied levels of accumulation extending down the anticlinal edges. Interestingly, those edge proteins barely accumulated at the inner periclinal wall, which led to a U-shaped-distribution pattern. Besides, this pattern was not due to signal attenuation caused by light scattering, as I observed the pattern in true optical slices taken from the median plane of the organs.

Those edge proteins are from different categories, such as MAP65-3 and POK1 are MAPs while BRK1 and Arp2 are actin organization related proteins. And their temporal expression and functional patterns are different too. Judging from their categories, the temporal order for functioning from early to late is POK1, MAP65-3, MUSTACHES, BRK1, Arp2 (Figure 2.12). In addition to their localization in roots, edge components also exhibited similar enrichment pattern at the edge in young leaves (data not shown).

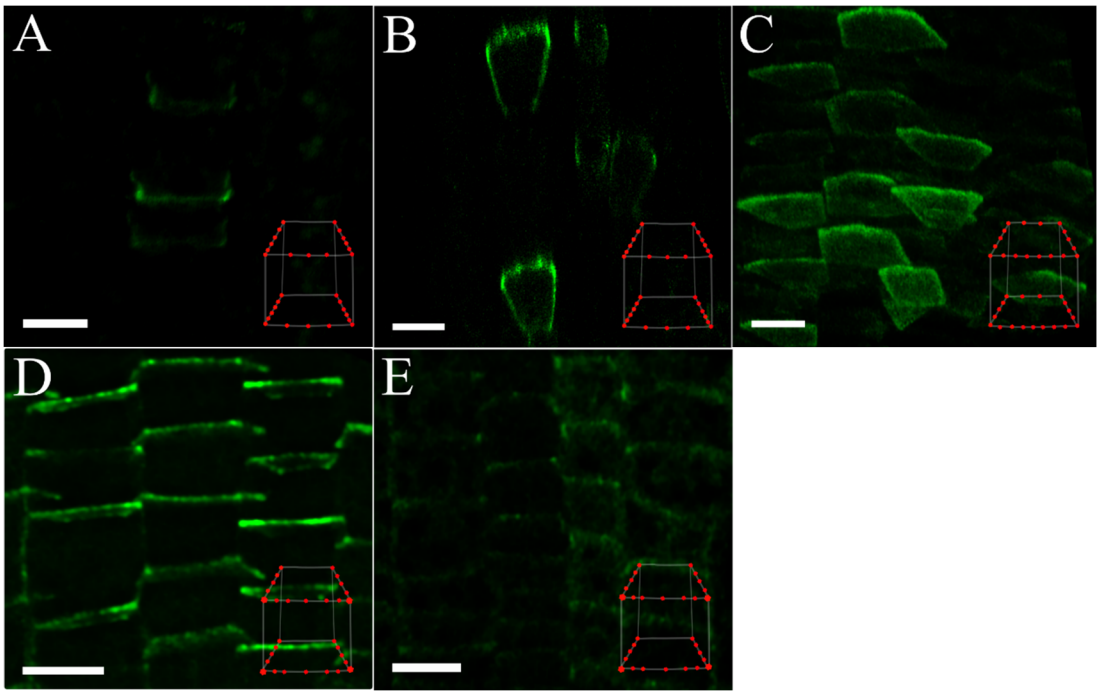

Figure 2.2 New edge components localization pattern in root.

(A-E) Confocal images of the localization pattern of newly identified edge proteins in roots. Reference schematic at lower right shows the edge proteins (red dots) localization pattern. A: MAP65-3-eGFP; B: YFP-POK1; C: MUS-3GFP; D: BRK1-YFP; E: Arp2-YFP. Scale bars are 5 μm.

2.2.2 MUSTACHES exhibits a vesicle-like particle movement.

Different from other edge proteins which are directly cytoskeleton-related, MUS is a leucine-rich repeat receptor-like kinase (LRR-RLK) and participates in guard cell symmetric division by positioning the MT organization center (Keerthissinghe et al., 2015). MUS signals were found in cell plates in both root and pavement cells. Consistent with the report, epidermal cells exhibited similar GFP-MUS signal pattern with preferential localizing at the outer periclinal edge (Figure 2.3A). Interestingly, I also found that MUS in the forming guard cell presented as a particle (Figure 2.3B). Time course analysis results showed that these MUS signal particles kept moving in a highly dynamic way, which resembles vesicle movement. Moreover, the movement of MUS was around the plasma membrane, which is consistent with the former report about MUS localization near the cell membrane (Keerthissinghe et al., 2015). Considering another edge protein—Rab A5c

mediates membrane trafficking to regulate cell edge, it's tempting to speculate that MUS may function in a similar scenario or even overlap with Rab A5c pathway.

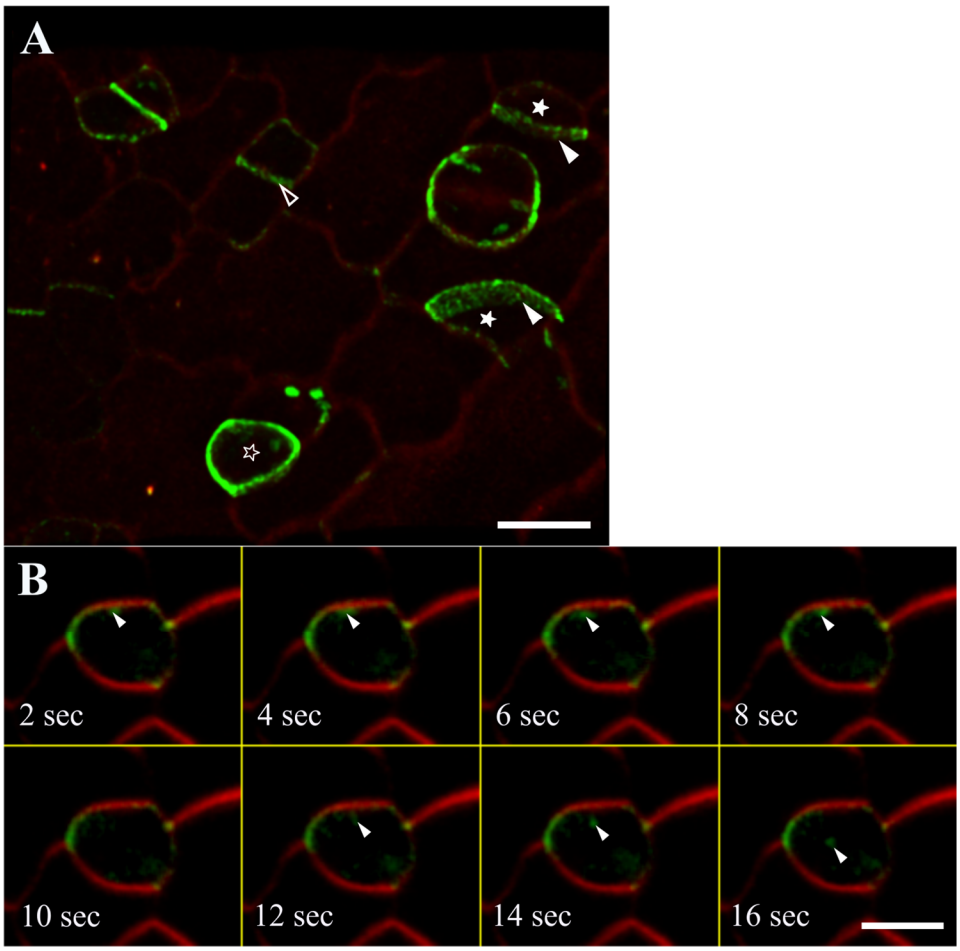

Figure 2.3 MUS-3GFP dynamic exhibits vesicle-like character in leaf.

Confocal images of MUS-3GFP with the FM4-64 stained plasma membrane (Red). (A) GFP-MUS localization in leaf. The white arrowheads mark GFP-MUS signal in meristemoid cells (solid asterisk) while hollow arrowhead marks signal in non-stomatal cells. Hollow asterisk indicates the guard mother cell. Scale bar is 5 μm. (B) GFP-MUS dynamic in a guard mother cell. The white arrowhead marks the MUS signal. Scale bar is 5 μm.

2.2.3 BRK1-YFP accumulate at cell edges.

Given that BRK1 is the first actin-related edge protein I found, I decided to focus on it. To gain insight into the function of BRK1 in Arabidopsis, I examined its localization pattern using lines

stably expressing *BRK1:: BRK1-YFP* in the *brk-1* null mutant background (Dyachok et al., 2008). In previous reports, the localization pattern of BRK1-YFP was described as being in "cell corners" (Dyachok et al., 2008), while I found that this pattern actually represented anticlinal cell edges (Figure 2.1; Figure 2.4A and F). Whether the cell corner description from Dyachok et al. was a nomenclatural mistake or an interpretation mistake is not clear. A similar pattern was observed in other tissues, such as cotyledon, true leaf, and hypocotyl (Figure 2.4 B, C, and D). In expanding leaf pavement cells that have begun lobe formation, punctuate BRK1-YFP enrichment was also found on the periclinal edges around the tips of lobes (Figure 2.4B and C). Intriguingly, BRK1-YFP signal also was found in palisade mesophyll cells, which is the first time this has been described in mesophyll cells (Figure 2.4 E). In these column-shaped mesophyll cells, BRK1-YFP signal mainly localized to the region of the anticlinal wall just internal to the outer periclinal edge. Given the localization pattern of BRK1 in all those cell types, it's conceivable that the BRK1-YFP localization is associated with high curvature edges.

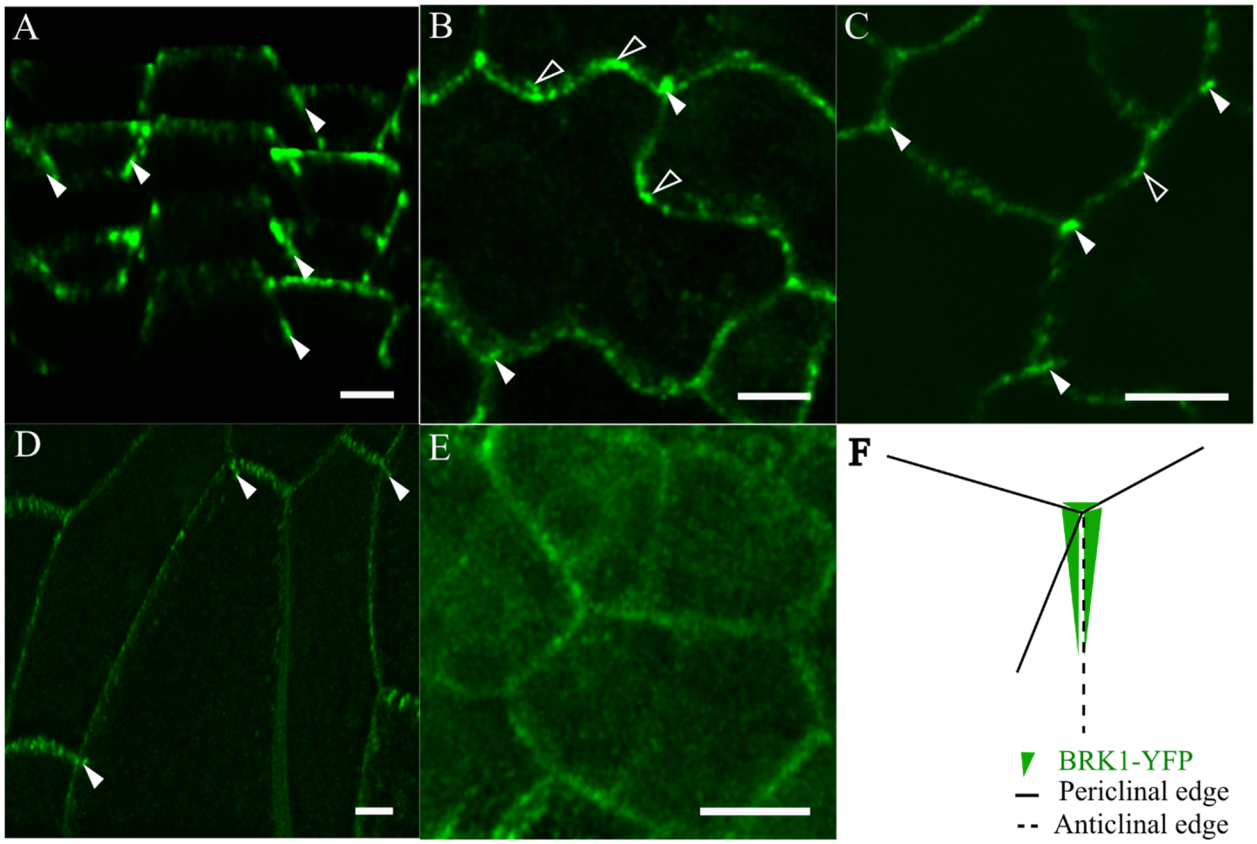

Figure 2.4 BRK1-YFP localization in different cell types.

A to E shows BRK1 localization in root, cotyledon, leaf, hypocotyl and palisade mesophyll cells, respectively. Solid arrowheads point out the signal enrichment in anticlinal edge and hollow arrowheads point out the lobe tip with local enrichment of the signal. Scale bar is 5 µm. (F) schematic image of BRK1-YFP localization pattern.

2.2.4 Time course analysis of BRK1-YFP dynamics reveals a gradual accumulation at newly-formed cell edges following cytokinesis.

While the preferential localization of BRK1-YFP implies an association between BRK1 and cell edge curvature, I next investigated the formation of this pattern from the earliest stage of cell wall formation, which is after cytokinesis has just completed. Because the epidermal cells of very young leaves have many cells in the various stage of division, the observed cell walls at any given time will be of the various stage of maturity. This is shown in Figure 2.5A, where the level of wall maturity is indicated by the heat map color of the arrows and arrowheads. BRK1-YFP signals were weakly, yet uniformly distributed along the newborn edges and the anticlinal edge exhibits brighter signal than the periclinal edge (Figure 2.5A). This cell wall maturity-dependent BRK1-YFP

enrichment suggests a continuous and gradual accumulation of BRK1-YFP at cell edges following cytokinesis.

To test this, time-course experiments were performed to follow the patterns of BRK1-YFP appearance following cytokinesis. As we see in Figure 2.5B and C, after cell division, BRK1-YFP localization in both root and leaf cells underwent gradually accumulation along the newly formed periclinal and anticlinal edges. It seems that the BRK1-YFP gradually accumulated at the new-born edges, which possess high curvature. Moreover, as the periclinal edge curvature changes during cell maturity, BRK1-YFP localization at the periclinal edge shifts from a uniform distribution to enrichment around the lobe (Figure 2.5B). The whole process was relatively slow, indicating a stable character of BRK1.

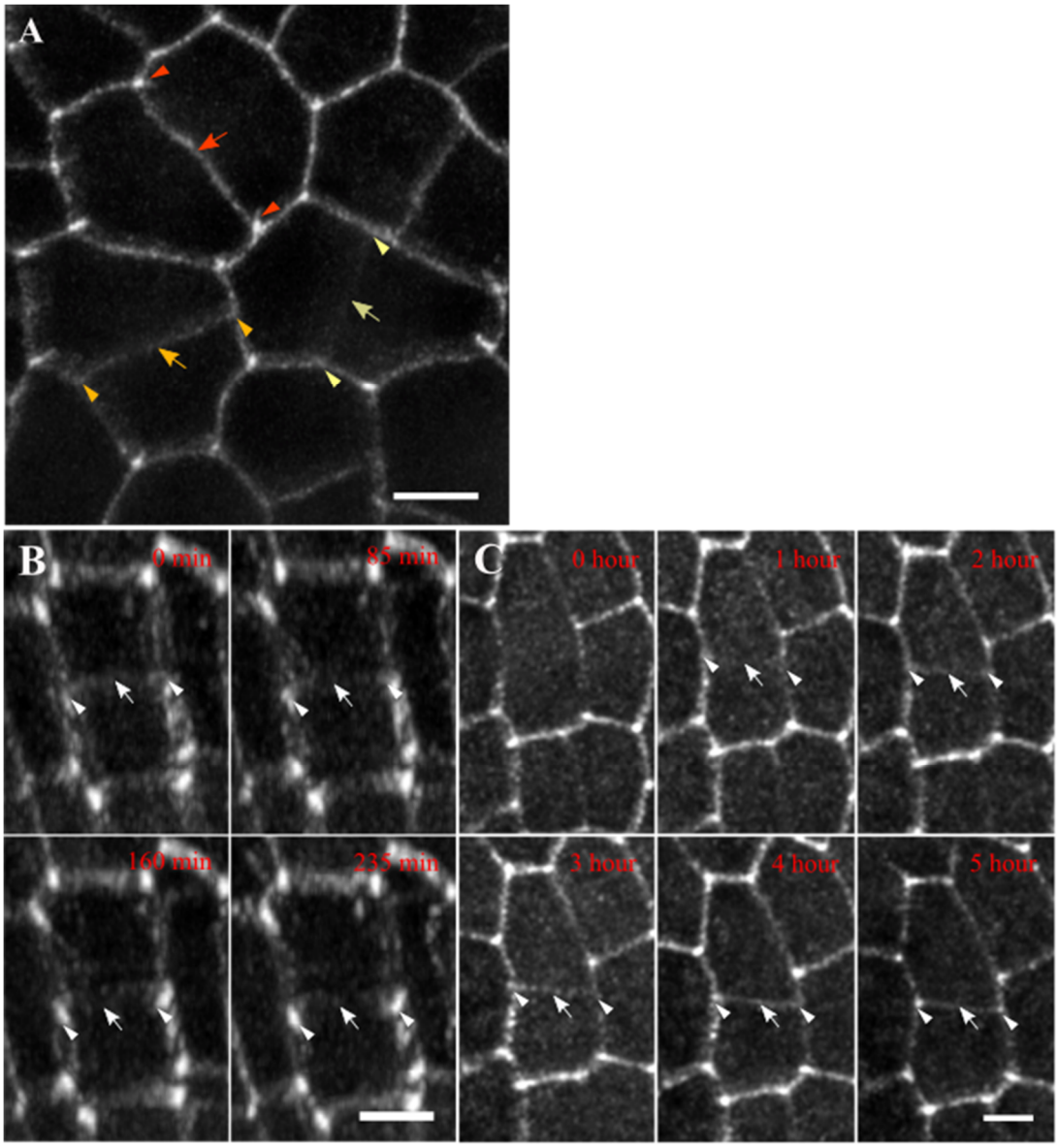

Figure 2.5 BRK1-YFP gradually accumulates at newly-formed anticlinal edges.

(A) BRK1 enrichment level at the cell edge in pavement cells at varied ages. Arrowheads and arrows point out the BRK1 signal on anticlinal and periclinal edges respectively and color range from light yellow to red indicates the signal accumulation. (B) and (C) time-lapses of BRK1 accumulation on cell edges in root and leaf pavement cells respectively. Arrowheads point out the anticlinal edge and arrows mark the periclinal wall. Scale bar is 5 μm.

2.2.5 BRK1 is relatively stable at both anticlinal and periclinal edges.

Our results about BRK1 accumulation at edges implied that the BRK1 is relatively stable. In an attempt to investigate the BRK1 dynamic on the periclinal edge and anticlinal edge, time course

experiments were performed. By examining the dynamic of BRK1-YFP, I found that BRK1 was relatively stable on both periclinal and anticlinal edge: even after 150 minutes, most BRK1 signal at both edges remained at its original place (Figure 2.6B). Moreover, BRK1-YFP localization on the anticlinal wall remained the same pattern over 24 hours (Figure 2.6C). All these results indicate a stable localization of BRK1, which could be due to either stable association of BRK1 at edges or BRK1 protein turnover.

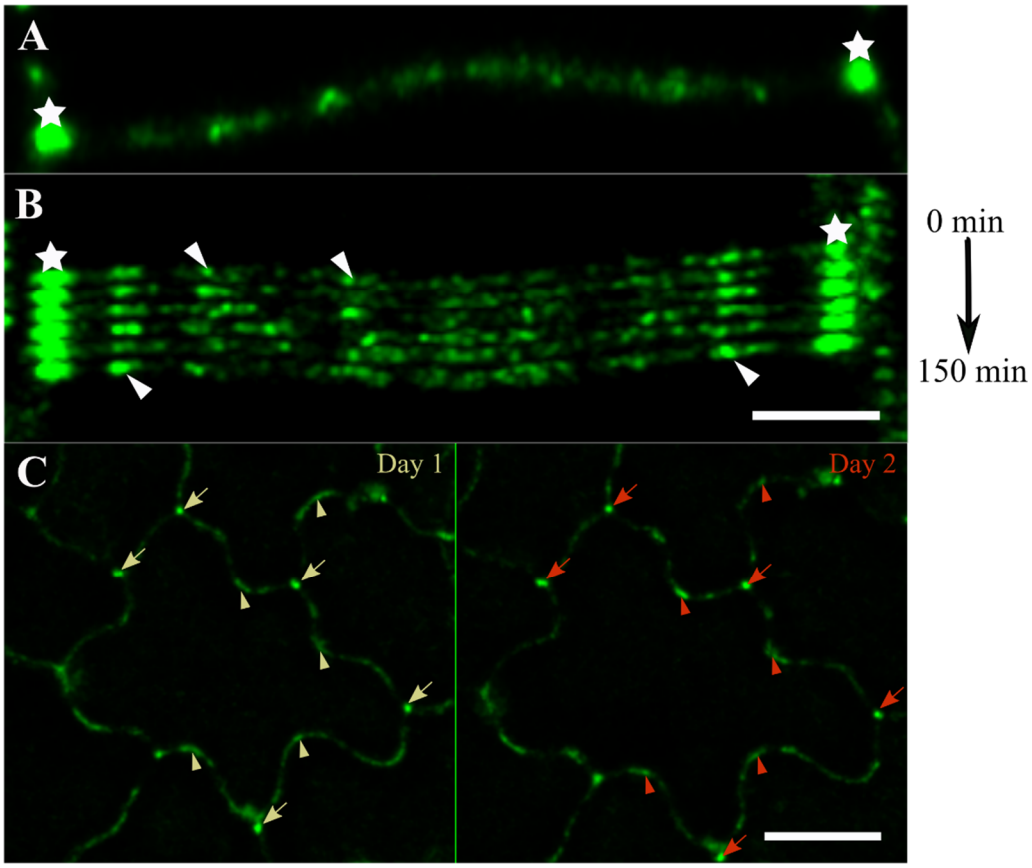

Figure 2.6 BRK1 is relatively stable at periclinal edges.

(A) shows the periclinal edge and the anticlinal edge it connected. (B) shows the kymograph of localization of BRK1-YFP over 2.5 hours. The stars indicate anticlinal edges and arrowheads denote the stable BRK1-YFP signal at the periclinal edge. The time interval is 30 mins. Scale bar: 5µm. (C) Long term of BRK1 localization pattern over 24 hours in pavement cells. Arrowheads and arrows mark the stable BRK1-YFP signal at the periclinal and anticlinal wall over time respectively. Scale bar: 10µm.

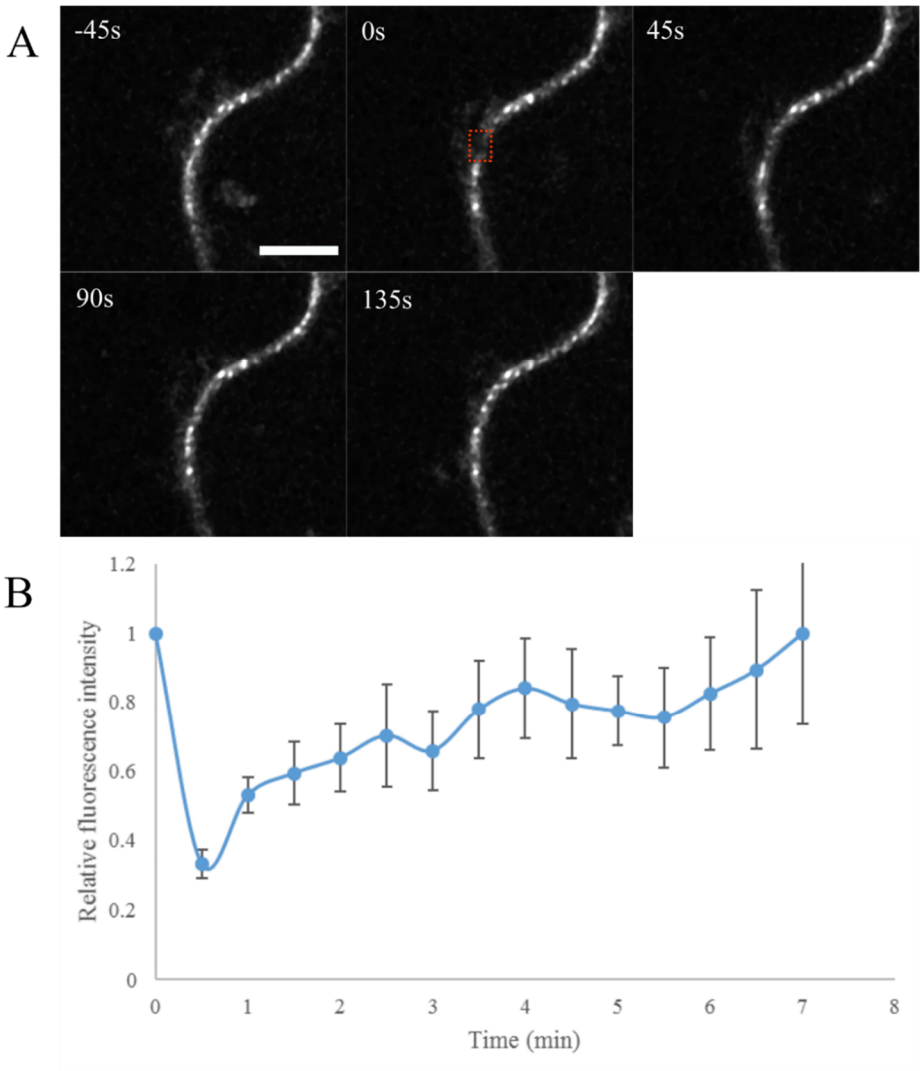

Figure 2.7 FRAP analysis reveals slow motility of BRK1-YFP on the edges.

(A) shows an example of BRK1-YFP during FRAP experiment. The initial bleaching region was marked as the red box. Scale bar is 10 μm. (B) Fluorescence recovery curve for a dataset of eight independent FRAP experiments on BRK1-YFP.

To clarify if the stable BRK1 pattern at edges is caused by association or turnover, fluorescence recovery after photobleaching (FRAP) was used to test whether the BRK1 is mobile on the edges and then characterize the mobility of the BRK1 (Figure 2.7A). The FRAP results showed nearly complete recovery of the BRK1-YFP signal at the edges. The fluorescence recovery time varied as the initial signal intensity changed: the stronger the initial signal, the short the recovery time (data not shown). In this case, I focused on the signal at the three-way junction and the average

recovery time is around 7 mins (Figure 2.7B). Comparted to the plasma membrane marker line LTI6b (fully recovery time is around 75s), the BRK1-YFP recovery was slow. This slow recovery of BRK1-YFP signal on the edges suggested a low turnover of BRK1 and slow motility mechanism that was different from the lateral diffusion of the proteins on the plasma membrane.

So far, I have no clue about the mechanism of how BRK1 (and even the Wave/Scar system) transportation to the edge and how BRK1 is relocated during cell maturation. To explore if F-actin or MT are involved in this process, drug treatments were applied in both short and long-term. It turns out that neither Latrunculin B (Lat B) or Oryzalin treatment affected BRK1 pattern in both leaf (Figure 2.8) and root (data not shown) in both short and long-term treatments.

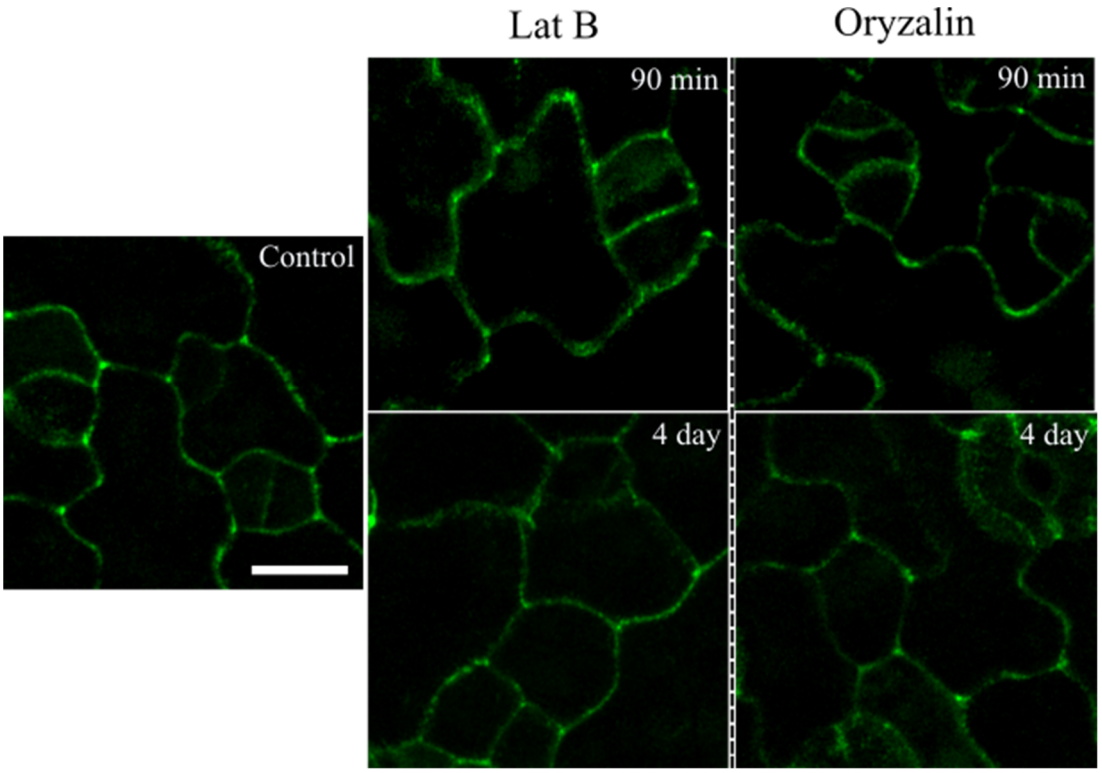

Figure 2.8 Cytoskeleton depolymerization drugs do not affect BRK1-YFP localization.

Leaf was treated with either Lat B and Oryzalin for short-term (90 mins) and long-term (4 days). Scale bar is 10 µm. For short-term treatment, seedlings of BRK1-YFP line were mounted in mock (ddH_2O), 25µM Lat B or 50µM Oryzalin just before imaging. For long-term treatment, BRK1-YFP line grew on medium containing either 0.1 µM Lat B or 0.1µM Oryzalin and 4-day-old seedlings were imaged.

2.2.6 BRK1-YFP localizes at the concave side of the lobe.

Considering the enrichment of BRK1 around lobe tip (Figure 2.4B), and its role in promoting actin polymerization, it is reasonable that BRK1-YFP localization at lobe tips corresponds to the concave side of the lobe. To test this, BRK1-YFP localization at cell lobes was examined with super-resolution microscopy. In the mature pavement cells, I found that the majority of BRK1-YFP lobe signal was at the concave side of the lobe (Figure 2.9A). The signal accumulation started from the internal region of the anticlinal wall to the outer periclinal edge and continued along the anticlinal wall. Some bright foci accumulated at the lobe tip and others distributed on the flanking wings around the tip. Quantification of BRK1-YFP signal intensity across the plasma membranes confirmed that the fluorescent peak of BRK1-YFP was located at the concave side (Figure 2.9B and D). The localization pattern of BRK1 was consistent with its function as an actin polymerization activator (Dyachok et al., 2008). According to Figure 2.9A, some BRK1-YFP signal particles seemed to cross the neighboring plasma membrane. To further corroborate which side —concave or convex— of BRK1 localizes, plasmolysis experiments were performed: consistent with above observation, after plasma membrane detached from the cell wall, the BRK1 signal was found to stay on the concave side of the lobe (Figure 2.9C). Therefore, based on both results, BRK1 was confirmed to localize at the concave side of the lobe, which is consistent with its function during lobe formation. Besides, other than localized at the plasma membrane on the concave side, after partial plasmolysis, BRK1-YFP signals also were found between the plasma membrane, where cell wall localizes. That localization indicates a new localization pattern that has not been described yet, and will be discussed in chapter four.

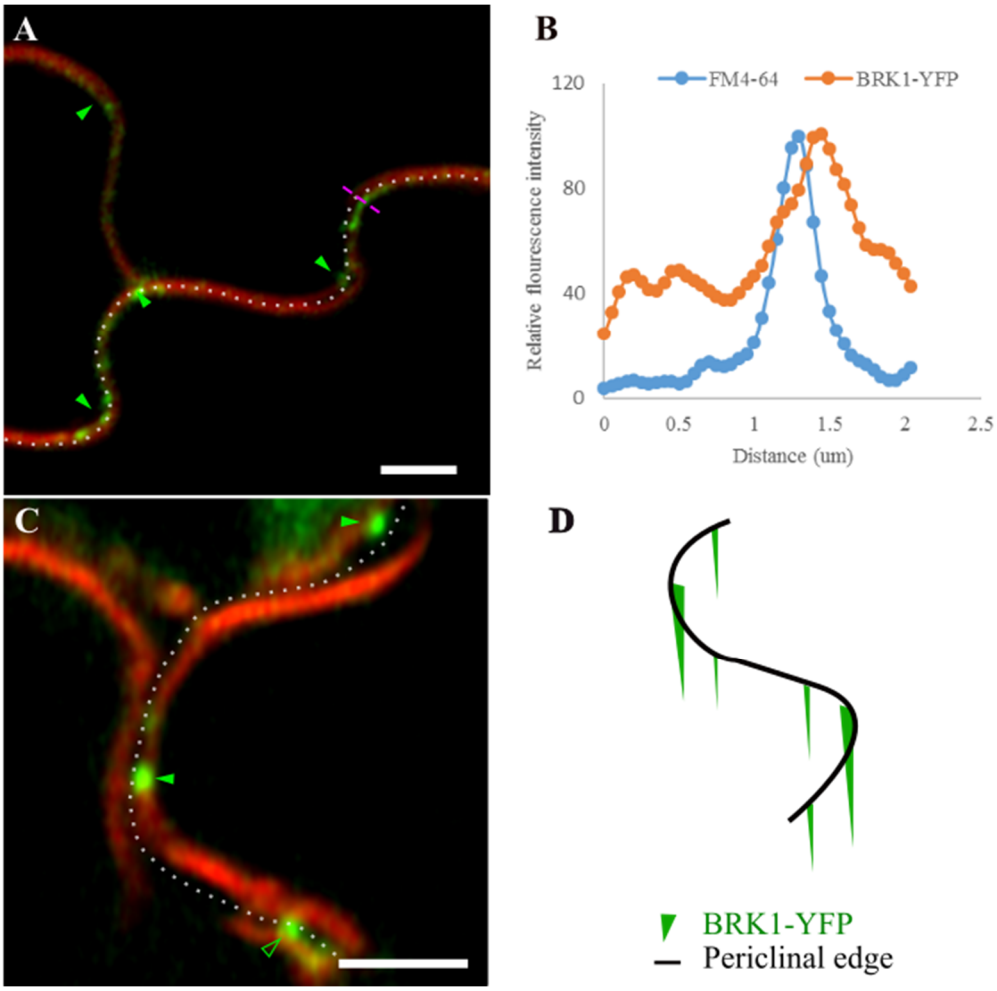

Figure 2.9 BRK1-YFP accumulates at the concave side of lobes.

(A) The plasma membrane was stained with FM4-64 and broken lines outline the cell wall. Green arrowheads point out the BRK1-YFP signal and purple dash marks the quantification spot for (B). (C) shows BRK1-YFP localization after mild plasmolysis. The hollow arrowhead marks the BRK1-YFP signal across the cell wall. Scale bar is 2.5 μm. (D) Schematic image of BRK1-YFP localization pattern at the lobe.

2.2.7 Periclinal wall curvature changes as lobe forms.

The observation of BRK1-YFP revealed a preferential accumulation at the anticlinal edge. Above analysis confirmed the enrichment of BRK1-YFP at the concave side of the lobe. Those localization patterns imply the possibility of a common mechanism that may related to cell geometry. Since anticlinal edge exhibits a high curvature, a subsequent experiment was conducted to verify if the concave-side-accumulation of BRK1-YFP also correlated with curvature (mainly the periclinal edge curvature) through examining curvature level at the lobe. For the periclinal

edge, the curvature forms due to the contacting of the periclinal and anticlinal wall, thus the periclinal edge curvature is along the Z-axis while the anticlinal edge curvature is along the lateral dimension because it forms by two anticlinal walls contacting. To examined the periclinal edge curvature at the lobe, pavements cells expressing *UBQ1:: LTI6b-GFP,* a plasma membrane marker line, were observed: during lobe formation, the two periclinal walls on the lobe exhibited different geometry. On the concave side, the periclinal wall was steeper, indicating a higher curvature (Figure 2.10A and B) while on the other side, the wall was relatively mild with a lower curvature (Figure 2.10A and C). This geometry pattern was associated with lobe formation because before lobe formation, both sides show a steeper periclinal edge. During the cell maturation, the outer periclinal wall gradually curves outward and thus certain periclinal edges selectively become rounded and decrease their curvature. In this case, periclinal edge curvature decreases at the convex side of lobe while remains sharp at the concave side.

My former results showed BRK1-YFP preferentially accumulated at the anticlinal edge, which exhibited a sharp curvature. Combining with the enrichment of BRK1-YFP at the concave side of the lobe, which also showed a higher curvature, these results indicate a tight correlation between BRK1 localization and cell edge curvature level.

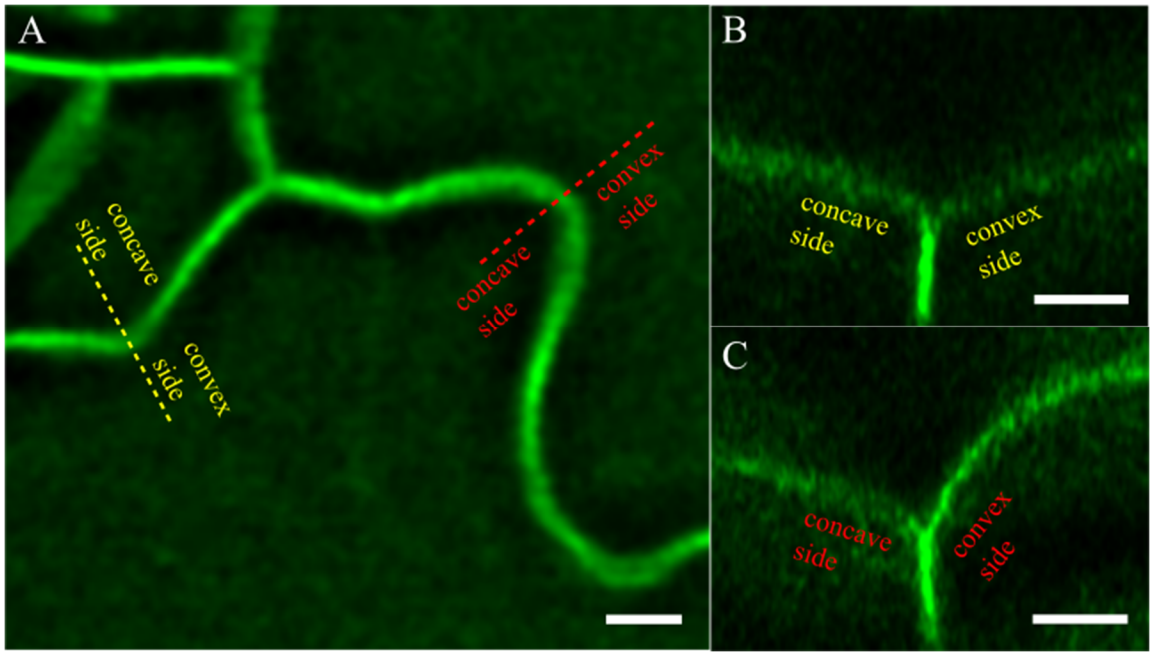

Figure 2.10 During lobe formation, the periclinal wall curvature changes.

(A) top view of pavement cells expressing *UBQ1:: LTI6b-GFP* (plasma membrane), which shows the different cell geometry of two adjacent periclinal walls. B and C are stack reslices (orthogonal views) corresponding to the colored lines in panel A. B shows a smaller, less developed lobe, where the edges are still sharp in each cell. C shows a larger, more developed lobe, where the concave side remains sharp, while the convex side has bulged outward. Scale bars are 5 μm.

2.2.8 BRK1-YFP accumulates at high curvature periclinal edges.

The results presented so far confirmed a relationship between BRK1 localization and cell edge curvature. As we know, during cell maturation, certain cell edge curvature changes as the related wall geometry changes. To further elucidate the relationship between BRK1-YFP and cell edge curvature, I examined the relationship between edge curvature and BRK1-YFP signal localization in pavement cells. To display the periclinal edge curvature, Propidium iodide (PI) was applied to label the cell wall. Consistently, I found that the BRK1-YFP signal intensity on the periclinal edge at the concave side of the lobe was higher than the one on the convex side (Figure 2.11A). To verify that, periclinal edge curvature in mature pavement cells was quantified with the Image J plugin called Kappa, and the relative fluorescence intensity of BRK1-YFP was measured by Image J. Kappa is a plugin for curvature analysis. By tracing the curve of edges, I drew a segmentation line that fit the curve and the plugin output a curvature value in form of reciprocal of the osculating

circle radius. Since BRK1-YFP began accumulation at the periclinal edge and the signal continued down the anticlinal wall, I only measured the signal fluorescence intensity at the edge and right below the edge. In total, 30 BRK1-YFP spots and 30 edges each spot belonged to were quantified. According to Figure 2.11B, it was obvious that the BRK-YFP signal intensity increased as the edge curvature increased. For example, the edge with higher curvature (such as the concave side of the lobe tip) exhibited higher BRK1-YFP signal intensity. This trend was also observed in hypocotyl cells (data not shown). These results show a positive correlation between BRK1-YFP fluorescence intensity and cell edge curvature.

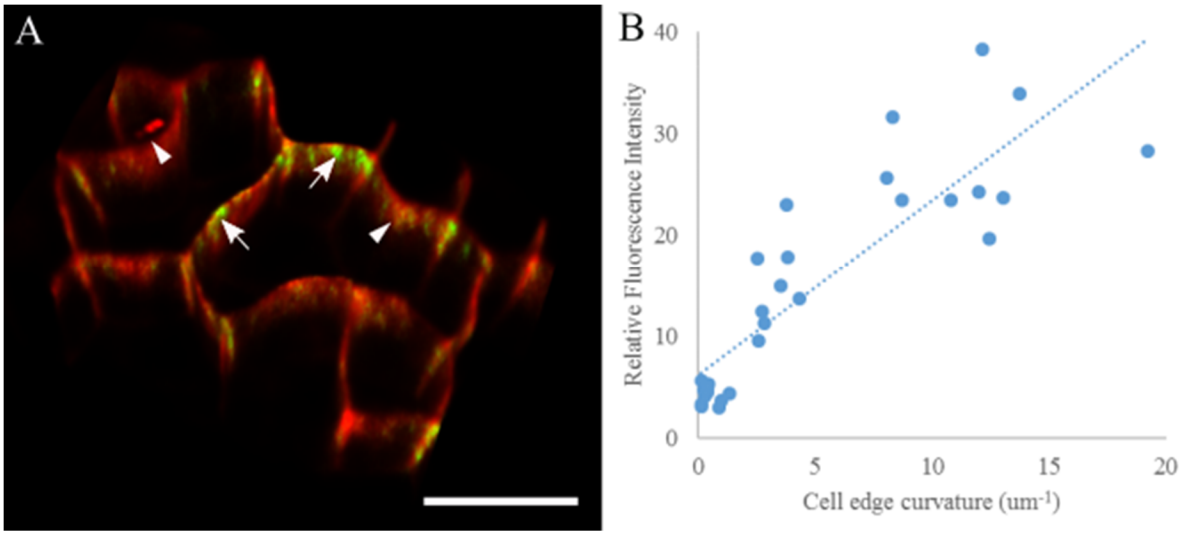

Figure 2.11 BRK1-YFP signal intensity changes as cell edge curvature change.

(A) pavement cells with PI staining. Arrows mark the BRK1-YFP at the concave side of lobe while arrowheads mark the convex side. Scale bar is 10 μm. (B) Quantification of BRK1-YFP signal on periclinal edges with different edge curvature. Dash line is a trend line.

2.3 Discussion

The ability to control cell edge stiffness and curvature are important for proper cell shape establishment and differentiation, and evidence thus far implicates the cytoskeleton and membrane trafficking systems in this control (Ambrose and Wasteneys, 2011; Kirchhelle et al., 2016). Through screening, I identified five new cell edge proteins. Interestingly, those edge proteins exhibited different spatiotemporal expression and localization patterns, suggesting there are

different mechanisms involved in cell edge regulation. For example, BRK1, Arp2/3, and MUS show a similar localization pattern in roots even though obvious different functions were reported. Those similar patterns may indicate a potential interaction and coordinated mechanism to modulate cell edge properties. Thus, it's essential to observe the whole process of cell edge formation and maturation by specifically visualizing the spatiotemporal dynamics of each edge protein during cell growth. Since I chose BRK1 for further analysis, this has not been done for the other identified edge proteins.

According to reports, POK1 and MAP65-3 are associated with cell division plane establishment. POK1 is a kinesin-12 motor protein, recruited to the cortical division zone (CDZ) during PPB formation (Muller et al., 2006). The POK1 at the CDZ remains present throughout mitosis and gradually narrows to a tight ring by late cytokinesis as the expanding cell plate begins contact with the parental wall (Figure 2.11A) (Muller et al., 2006; Lipka et al., 2014). MAP65-3 selectively bind with MT plus end in the phragmoplast midline to facilitate Golgi-derived vesicle trafficking to the developing cell plate (Figure 2.11B) (Muller et al., 2004; Caillaud et al., 2008; Ho et al., 2011). The activity of MAP65-3 is regulated by a series of proteins, which includes POK2, paralogy of POK1 (Herrmann et al., 2018). Combining with other proteins, POK1 and MAP65-3 may facilitate the local modification of the plasma membrane at the CDZ by control of vesicle trafficking and microtubule organization (Van Damme and Geelen, 2008).

What I found was that after cytokinesis, both POK1 and MAP65-3 remain at the anticlinal edge even after the cell plate merges with the parental wall, which might indicate a new function other than reported for guiding cell plane orientation or maintaining phragmoplast integrity. Intriguingly, the mutant of both *pok1/pok2* and *map65-3* exhibits bulgy outer periclinal wall in root meristematic cells, indicating a decreased curvature of both the transverse and radial edge (Caillaud et al., 2008; Lipka et al., 2014). This bulgy phenotype is similar to the *clasp-1* mutant, which shows a defect in transfacial bundle formation. Considering the function of MAP65-3 in crosslinking antiparallel MTs at the phragmoplast midline, and the potential interaction between POK1 and MAP65-3, it's possible that like CLASP at edges, MAP65-3 and POK1 may participate in the transfacial bundle regulation to maintain the edge curvature.

By localizing at the newly formed cell edges, MUS helps to enforce the cytoskeletal polarity (Keerthissinghe et al., 2015). In the guard cells, MTs form and maintain polarized arrays with

minus ends localizing at the stomatal pore and plus ends radiating outward (Liu et al., 1993; Marc, 1997). In stomatal pore, γ-tubulin accumulates, representing an MTOC (Marc, 1997). Interestingly, the MT polarity pattern is disrupted in the *mus* mutant with the plus end projecting inward to the pore (Keerthissinghe et al., 2015). Considering GCP2/3 containing γ-tubulin complex nucleates MTs and both MUS-3GFP and GCP2/3-3GFP exhibit cell edge localization in root cells, it's tempting that MUS may regulate GCP2/3-3GFP localization or even, MUS may regulate cell edge maturation through GCP2/3 pathway. Still, a couple of questions need to be clarified on this idea. For example, does MUS influence GCP2/3 through directly phosphorylation or indirectly phosphorylating other subunits of the γ-tubulin complex? Besides, MUS-3GFP exhibits enrichment around the three-way junction in meristemoid cells, indicating a possible association with edge curvature (Keerthissinghe et al., 2015). And our result shows some MUS dynamic is similar to vesicle, which could be part of a recruitment mechanism to the cell edge.

The other two proteins— BRK1 and Arp2/3—appear after cytokinesis only and remain for some time and are presumably involved in cell edge maturation. As both BRK1 and Arp2/3 are involved in branched actin formation, they might affect cell geometry through actin-dependent vesicle trafficking or other mechanisms. Similar to RAB-A5c's mediation of cell wall stiffness, both BRK1 and Arp2/3 may also modulate cell wall elasticity through influencing the delivery of the cell wall material to the cell junctions (Figure 2.12C) (Frank and Smith, 2002; Frank et al., 2003; Djakovic et al., 2006; Dyachok et al., 2008; Facette et al., 2015).

Besides, I also found that those edge proteins exhibit preferential accumulation at the outer periclinal edges, which in the case of epidermal cells are unique in that they face the environment and are free to expand outward because there is no counter-expansion from neighboring cells, which is the case for all other edges. Considering that the outer periclinal wall bears much of the mechanical stress generated by tissue tension and bulges outward during cell maturation, the enrichment of the above edge proteins may suggest a key role in modulating periclinal edge curvature, and then the periclinal wall bulginess.

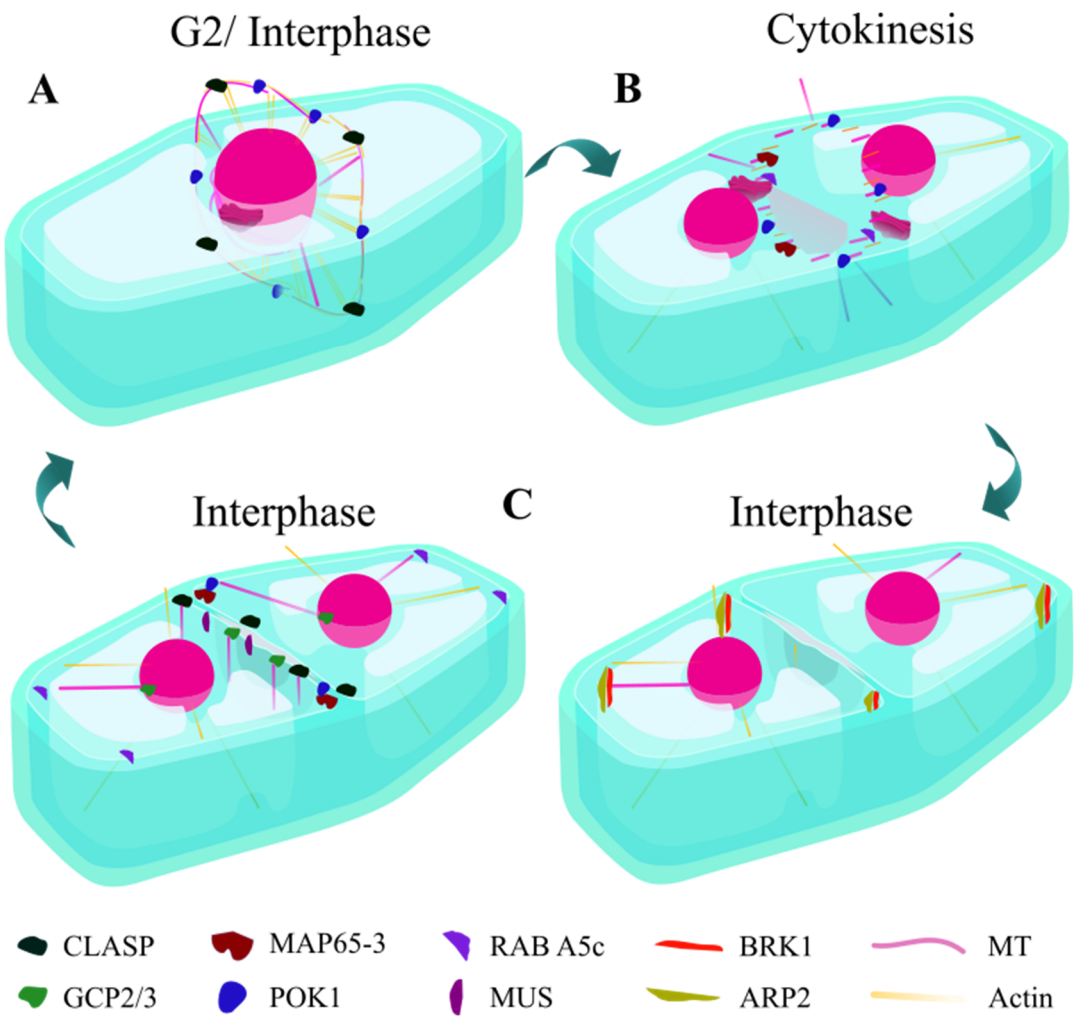

Figure 2.12 Schematic illustration of edge protein localization patterns.

(A) During Preprophase, POK1 is positioned at the plasma membrane to forecast the PPB forming site, and CLASP stabilizes the PPB. (B) During cytokinesis, RAB5Ac and MAP65-3 regulate the Golgi-derived-vesicle trafficking to facilitate the cell plate formation. (C) Left panel, CLASP, and GCP2/3 at the cell edge maintain the transfacial bundles through either stabilizing or nucleating MTs. Right panel, BRK1, and Arp2/3 at the cell edge might modulate cell edge through cell wall material delivery. Modification is done by Z.C based on SVG file on plant cell cycle from Kelvinsong [CC0], from Wikimedia Commons.

During cell growth, local wall stiffness alters through either cell wall composition changes or microfibril pattern remodeling. The change of wall stiffness leads to redistribution of stress generated due to cell growth. It is therefore conceivable that the cell edge components I found so far are associated with the regulation of cell wall stiffness specifically at cell edges.

To better understand the mechanism of BRK1 localization, BRK1-YFP distribution patterns and dynamics were analyzed by a series of experiments.

Prior functional analysis described BRK1-YFP localization to cell corners (Dyachok et al., 2008) while my results showed that instead of a periphery spot, BRK1 specific enriches at the anticlinal edge. The edge localization pattern matches with its function to produce F-actin and then facilitate the delivery of wall material containing vesicles to the anticlinal edge to glue the neighboring anticlinal walls together. Corresponding to the BRK1 edge localization, the *brk-1* mutant exhibits reduced cell adhesion among anticlinal walls of neighbor cells (Le et al., 2006) and thus bulgy outer periclinal wall (Figure 4.1).

My results suggest that cell edge curvature might influence the accumulation of BRK1 to the edge. BRK1 signal exhibits a gradual accumulation at cell edges with higher curvature after cytokinesis, and edge curvature is associated with cell wall maturity. During cell growth, the anticlinal edges generally have brighter BRK1-YFP signal than the periclinal edges. The BRK1-YFP signal at the periclinal edges gradually changes from a uniform distribution to enrichment around the developing lobes. Interestingly, the BRK1-YFP signal pattern change corresponds to cell wall maturity, which generally begins sharp and gradually round off (Figure 2.12). After cytokinesis, the newly formed cell wall joins the parental walls at roughly 90º angles, forming four highly curved cell edges. During this time, BRK1-YFP uniformly distributes along the edges; as subsequent cell differentiation, the individual cell walls develop and then undergo edge curvature changing, includes the outer periclinal edge in pavement cells and transverse edge in root and hypocotyl cells. As these edges change curvature, BRK1-YFP signal localization pattern changes from uniform to specific enrichment (Figure 2.13). Based on these results, I suggest that the BRK1 localization pattern is affected by cell edge curvature, which is in turn determined by cell wall maturity.

Besides, the edge-curvature-associated BRK1 localization pattern might correspond to certain functions. During cell growth, the cell edges at both three-way junction (anticlinal edge) and outer periclinal wall (periclinal edge) are under intense mechanical force and thus their corresponding cell wall get thickened and stiff (Kutschera, 2008). The stiffen cell edge happen to match with the localization pattern of BRK1. This correspondence may help maintain cell geometry through cell wall remodeling, which is actin-associated.

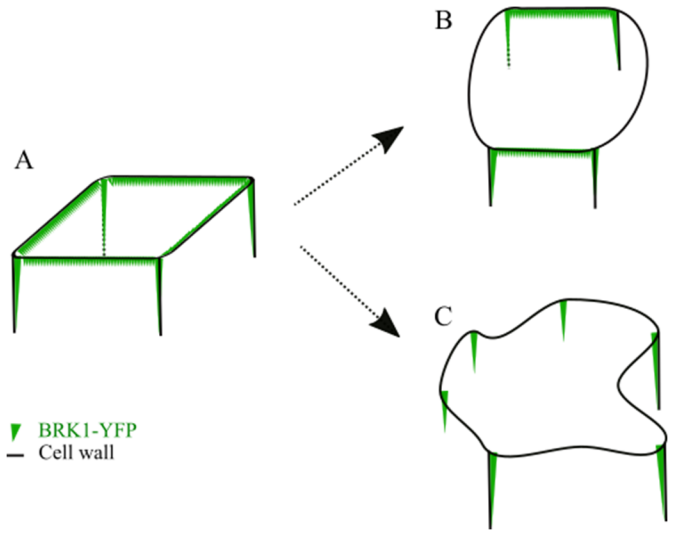

Figure 2.13 BRK1 localization pattern model.

A to C schematic depicting BRK1-YFP localization pattern in different cell types with varied cell wall maturity: (A) newborn root or pavement cell showing BRK1 signal accumulation at both anticlinal and periclinal edges; (B) mature root or hypocotyl cell showing preferential accumulation of BRK1 at both anticlinal and transverse periclinal edge; (C) mature pavement cell showing dominant BRK1 localization at the anticlinal edge.

2.4 Materials and methods

2.4.1 Plant materials and growth conditions.

Arabidopsis thaliana ecotype Columbia 0 (Col-0) was used as wild type in this study. The transgenic line *BRK1:: BRK1-YFP* (Dyachok et al., 2008) was obtained from the E. Blancaflor lab (The Samuel Roberts Noble Foundation), *Arp2:: Arp2-YFP* from Y. Wei lab (University of Saskatchewan), *MAP65-3:: MAP65-3-eGFP* from B. *Favery* lab (INRA-CNRS-Université Nice Sophia Antipolis), *MUS::MUS-3GFP* from F. Sack lab (University of British Columbia), *POK1::YFP-POK1* from S. Muller lab (University of Tuebingen).

Seeds were sterilized with 70% ethanol, rinsed five times with sterilized water and plated onto Petri dishes containing ½ MS media, 1.0 % agar, 1 % sucrose and pH is 5.7. Plates were wrapped with parafilm (Bemis Inc.) and transferred to a 21 °C growth cabinet (with continuous light) and placed in the rack vertically. Young root, hypocotyl and cotyledon were imaged at 3–4 days after germination, and true leaf cells were imaged at 4–5 days after germination.

2.4.2 Tissue preparation and microscopy.

All observations were performed on living cells. For true leaf imaging, cotyledons were cut off at the base with fine scissors and the rest of seedlings were mounted. All the tissue samples were mounted in Nunc chambers (Lab-Tek) with 10 ul Perfluoroperhydrophenanthrene (PP11) and covered by 2~3-mm-thick 0.7% Phytagel. All CLSM images were obtained via point-scan confocal microscopy: Zeiss Meta 510 with Zeiss Axiovert 200M microscope, 63X water immersion and Zeiss 880 with Airyscan, both 40X and 63X water immersion. GFP fluorescence was detected with an excitation wavelength of 488nm from an argon laser and captured with emission wavelength of 495 – 550nm. YFP was detected with an excitation wavelength of 514nm from an argon laser and captured with emission wavelength of 495 – 550nm. FM4-64 was detected with an excitation wavelength of 514nm from an argon laser and captured with emission wavelength of 570 – 645nm. PI was detected with an excitation wavelength of 514nm from an argon laser and captured with emission wavelength of 570 – 640nm. The Z-stack interval varies from 0.2 µm to 0.4 µm. For sampling, more than 5 cotyledons or first pair of true leaves were picked and more than 10 cells for each sample were imaged.

2.4.3 Image analysis.

Images were processed with Image J software (http://rsb.info.nih.gov/ij/). The ClearVolume plugin (https://imagej.net/ClearVolume) (Royer et al., 2015) from Image J and Fluorender (http://www.sci.utah.edu/software/fluorender.html) (Wan et al., 2009) were used for 3D renderings and Kappa (https://imagej.net/Kappa) from Image J was used for cell edge curvature analysis. For the curvature quantification, segmented lines were drawn to fit the edge curvature and the curvature value of every pixels on the line was exported as a CSV file. The maximal value was chosen as cell edge curvature value and abnormal value was ignored if it's not fit the overall data trend. Figures were assembled using Corel Draw software (www.Corel.com; Corel System. Ottawa, ON, Canada), and Inkscape vector graphics software (www.inkscape.org). Statistical analysis was performed with Microsoft Excel (Microsoft, Edmond, WA).

2.4.4 Drug treatment.

4-day-old seedlings of *BRK1:: BRK1-YFP* were grown on ½ MS media with 1.0 % agar and 1 % sucrose. For short-term treatments, seedlings were incubated with either 25µM Lat B or 50µM Oryzalin (Fisher Scientific). For long-term treatment, seedlings were grown directly on ½ MS

media containing either 0.1 μM Lat B or 0.1μM Oryzalin. Both true leaf and root were imaged using the above treatments.

2.4.5 Fluorescence recovery after photobleaching (FRAP) analysis

FRAP experiments were performed on Zeiss 880 with Airyscan. YFP was detected with an excitation wavelength of 514nm from an argon laser and captured with emission wavelength of 495 – 550nm. A rectangular region of interest was photobleached by 514-nm laser line operating at 15% laser power with 30 iterations. The fluorescence recovery was monitored at 30- or 45-seconds interval. The fluorescence recovery data were analyzed in Image J, and were normalized for bleaching during imaging as described (Konopka et al., 2008). Since the observed recovery time range varies as the original signal intensity changes, I picked up eight samples with similar signal intensity and position for analysis.

2.4.6 FM4-64 and PI staining.

To label the plasma membrane, FM4-64 (Sigma-Aldrich) was used. Five-day-old seedlings were incubated with 10μM FM4-64 in 1.5ml Eppendorf tube and then centrifuged at 3381g for 1min. After centrifugation, keep incubating for 20mins at room temperature. Stained samples were rinsed gently with distilled water, mounted with PP11, and imaged in chambers as above.

To label the cell wall, Propidium Iodide (PI) (Invitrogen) was used. Four or five-day-old seedlings were incubated with 100μg/ml PI in 1.5ml Eppendorf tube and then centrifuged at 3381g for 1min. After centrifugation, keep incubating for 20 mins at room temperature. Stained samples were rinse gently with distilled water, mounted with PP11, and imaged in chambers as above.

Chapter 3 BRK1 and microtubules

3.1 Introduction

3.1.1 Pavement cell morphology and cytoskeleton

As an attractive system for cell expansion study, pavement cells form a jigsaw-puzzle shape, which is based on subcellular anisotropic growth (Fu et al., 2002, 2005). Specifically, the growth is associated with the heterogeneity of cell wall composition, which is regulated by the cytoskeleton. Correspondingly, anticlinal wall property is heterogenous with plastic lobe and stiffer indentation (Majda et al., 2017). Interestingly, the pavement cell shape is affected by even minor change of wall composition, and de-methyl esterified pectin is found in the lobe. All these observations implied a correlation between cell wall property and lobe formation, which associates with the cytoskeleton (Majda et al., 2017; Sotiriou et al., 2017).

A series of studies were performed to explore the mechanism underlying pavement cell shape establishment. According to studies, cortical MTs accumulate in the indentation side and restrain the cell wall growth through guiding the cellulose microfibrils deposition while F-actin converges at the opposite for lobe formation, presumably facilitating the delivery of vesicles that contain cell wall materials for cell wall expansion (Fu et al., 2002; Sampathkumar et al., 2014a; Armour et al., 2015). The important role of both cytoskeletons is confirmed by cytoskeleton-related mutants showing lobe formation defects. A series of actin-related mutants exhibit either a lower level of lobeyness or no recognizable lobes. The corresponding proteins include Rho of plants (ROP) — signal factors that upstream of F-actin (Fu et al., 2002, 2005), Arp 2/3 complex—branch actin nucleator (Le et al., 2003; Mathur et al., 2003a, 2003b), Formin1—actin nucleator (Rosero et al., 2016), SCAR complex—activator of branch actin nucleator (Basu et al., 2004, 2005, 2005; Le et al., 2006). Moreover, pharmacological experiments further confirmed those findings by the application of actin depolymerization reagent such as Lat B (Panteris and Galatis, 2005). Mutants that affect the MT cytoskeleton also support MT's role in lobe formation by exhibiting either non-lobed or lightly lobed pavement cells. These correlated proteins include ANGUSTIFOLIA—MT-associated protein (Tsuge et al., 1996), KTN1—MT severing protein (Burk et al., 2001), GCP2—MT nucleator (Nakamura and Hashimoto, 2009). These results also were confirmed by pharmacological experiments using either oryzalin or colchicine (Wernicke and Jung, 1992; Panteris et al., 1993). So far, this cytoskeleton pattern during lobe formation was proposed to be governed by ROP family (Fu et al., 2005; Lin et al., 2013).

3.1.2 F-actin and cell plane orientation

In addition to its function in cell expansion, actin is also involved in division plane prediction to regulate cell geometry. During the cell cycle, F-actin forms different arrays in each stage to facilitate the cell plane orientation. In interphase, some F-actin arrays wrap up the nucleus while others link the nucleus to the cortical F-actin. Those F-actin arrays were proposed to position the nucleus for preparation of future mitosis (Traas et al., 1987). After the onset of mitosis, F-actin arrays rearrange to parallel to the newly formed PPB. The F-actin arrays at this position may correlate with PPB narrowing and disappear as PPB breaks down (Pickett-Heaps and Northcote, 1966). The disappear of MF arrays leaves a zone of F-actin depletion at the former PPB site (termed as ADZ for actin-depletion zone) (Cleary et al., 1992; Liu and Palevitz, 1992), and this zone is further surrounded by enrichment of F-actin at the edge of ADZ (Cleary, 1995; Valster and Hepler, 1997). The ADZ persists until telophase and acts as a negative marker for positioning the new cell wall inserting (Wright and Smith, 2007). Thus, both the ADZ zone and PPB precisely predict the cell plane orientation. At the metaphase, F-actin surrounds the spindle and presumably maintain the spindle position (Lloyd and Traas, 1988). In late anaphase, phragmoplast arises as both MTs and F-actin align up with plus end pointing at the cell center. The F-actin transport vesicles containing cell wall materials to the expanding phragmoplast center to form the cell plate. In addition to F-actin, researches on myosins—an F-actin motor— also suggest a role of myosin in cell division (Molchan et al., 2002; Li et al., 2010).

3.1.3 Interaction between MTs and F-actin

MTs and F-actin form distinct networks to regulate various cellular processes. Even though performing separate functions, MTs and F-actin still coordinate in processes such as intracellular transport and cell division. During those processes, the integration of F-actin and MTs could involve in direct physical interaction, which was mediated by MAPs or actin-binding proteins (ABD) (Collings and Wasteneys, 2005; Collings, 2008; Sampathkumar et al., 2011).

Observations from both pharmacological approaches and microscopy find that F-actin dynamics is associated with MTs: the stabilized short F-actin aligns and move along MTs and the perturbation of actin dynamic leads to less ordered MT arrays in hypocotyl cells (Sampathkumar et al., 2011). The similar scenario was observed during PPB formation: single short actins align and attach to MTs at the initiation of PPB and elongate along MTs as the PPB matures (Takeuchi

et al., 2016). During the PPB formation, those short actins were proposed to serve as bridge linker to connect MTs together (Takeuchi et al., 2016).

Considering that F-actin and MTs cooperate tightly during either cell expansion or cell division, I hypothesized that the mutation of *Brk-1* gene might leads to abnormal MTs pattern during lobe formation and cell division defects in the pavement cells.

3.2 Results

3.2.1 No obvious F-actin defects were observed in the *brk-1* mutant.

Considering BRK1's functioning to promote ARP2/3-dependent branch actin nucleation, and that the *brk-1* mutant shows lobe formation defects, subsequent analysis was conducted to determine if the actin organization in the pavement cells in the *brk-1* mutant was affected. To examine actin organization in pavement cells, two actin reporter lines were used: *35S::GFP-ABD2-GFP*, which labels cortical and cytoplasmic F-actin (Dyachok et al., 2014); and *35S::Lifeact-Venus*, which decorates thick cytoplasmic F-actin bundles (Dyachok et al., 2014). I crossed these two lines into the *brk-1* mutant and then examined F-actin in pavement cells. Surprisingly, there were no obvious F-actin organization defects in the pavement cells in the *brk-1* mutant expressing either of reporter lines (Figure 3.1A&B). In particular, given that BRK1-YFP is enriched in the concave side of the lobe, where actin has also been reported to accumulate, I anticipated that the *brk-1* mutant might lack this enrichment. However, I observed no accumulation of actin in the concave side of the lobe in any of the lines examined, which is in contrast to Fu et al., (2002, 2005), but in agreement with several later reports (Armour et al., 2015; Belteton et al., 2018).

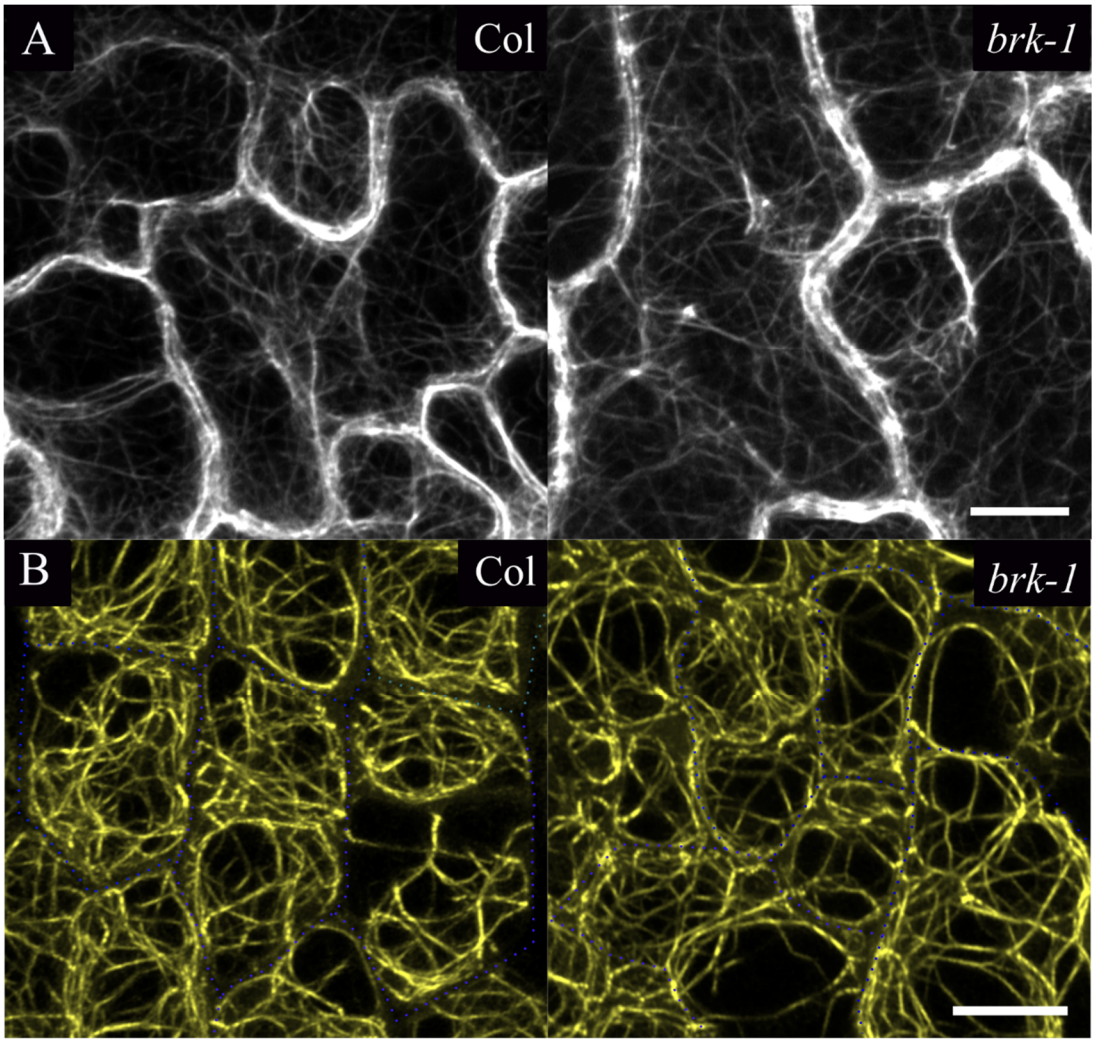

Figure 3.1 No obvious F-actin defect was observed in the *brk-1* mutant.

(A) F-actin in the pavement cells of wild type and the *brk-1* mutant expressing *35S::GFP-ABD2-GFP*. (B) F-actin in the pavement cells of wild type and the *brk-1* mutant expressing *35S:: Lifeact-Venus*. Blue lines mark the cell outline. Scale bar is 10 μm.

3.2.2 BRK1 and MT distribution do not overlap.

Given the lack of obvious defects in actin organization in the *brk-1* mutant, but the accumulation of BRK1-YFP at the concave side of the lobe (Figure 2.8), I hypothesized that BRK1 and MTs might distribute alternatively with each other in a cell. To investigate the localization of BRK1 and MTs, the MT marker line *UBQ1:: RFP-TUB6* was crossed into *BRK1:: BRK1-YFP*. With the double marker line, I investigated the localization of both MTs and BRK1 at the lobes. It turns out

that the localizations of BRK1-YFP and RFP-TUB6 did not overlap with each other in a cell (Figure 3.2). This was consistent with the known depletion of MTs from the concave side and their enrichment at the convex side of lobes.

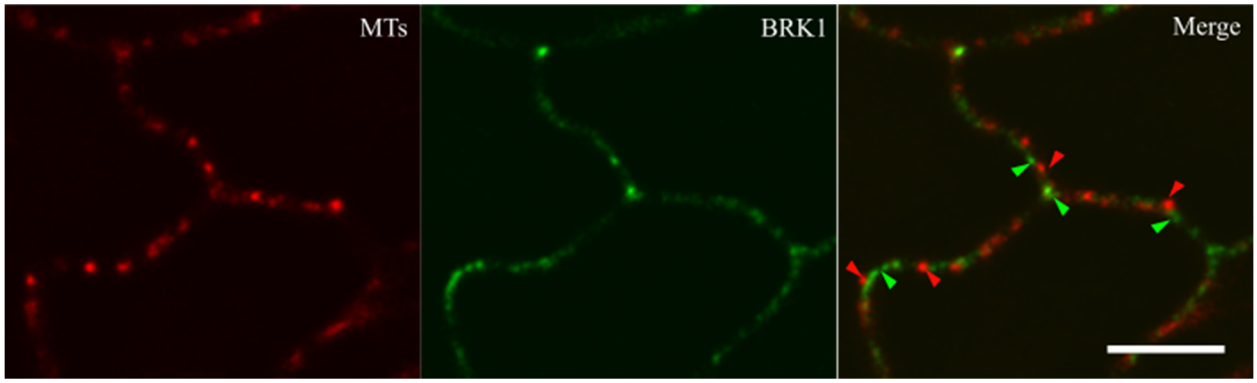

Figure 3.2 BRK1 localization at periclinal edges does not overlap with MTs.

BRK1 and MT localization were examined through plants co-expressing *UBQ1:: RFP-TUB6* (red) and *BRK1:: BRK1-YFP* (green). The green arrowhead marks BRK1 signal, and red arrowhead denotes MT. Scale bar is 5 μm.

3.2.3 The *brk-1* mutant exhibits anticlinal microtubule bundle (AMB) formation defect.

In plant cells, AMBs line the anticlinal walls at incipient lobing sites and wrap around to the outer periclinal face, where they splay out to populate the CMT array (Ambrose et al., 2011; Zhang et al., 2011). AMBs lead to localized wall thickening at the future convex side of the lobe, which coupled with the fan-like arrangement of cellulose microfibrils extending out the periclinal wall, will drive the lobe initiation (Panteris and Galatis, 2005; Szymanski, 2014). Since the *brk-1* mutant exhibits lobe formation defect phenotype, it is possible that the AMB structure is influenced in the *brk-1* mutant.

I checked the AMB formation in pavement cells in both wild type and the *brk-1* mutant. To this end, *UBQ1:: GFP-TUB6* was crossed into the *brk-1* mutant and a series of analysis on both CMT pattern, and dynamic were performed. It turns out, compared to wild type, fewer AMBs were observed in the *brk-1* mutant (Figure 3.3A). To quantify this, fluorescence intensity plots were generated corresponding to the cell perimeter (Figure 3.3B). Compared to wild type, the *brk-1* mutant exhibited fewer fluorescence peaks, which correspond to AMBs. Moreover, the AMB

fluorescence peaks in the *brk-1* mutant were broader and not as pointy as those in wild type, indicating relatively loose AMBs.

The AMB frequency in pavement cells was also measured through dividing AMB number in a cell by its cell perimeter. I only picked up the cells with lobe formed and measured 30 cells from wild type and the *brk-1* mutant respectively. Consistently, the AMB frequency in the *brk-1* mutant was lower than wild type (Figure 3.3C).

Combining with lobe initiation theory above mentioned, it is possible that the lobe defect in the *brk-1* mutant was attributed to the partial failure of AMB formation rather than a direct defect in F-actin organization.

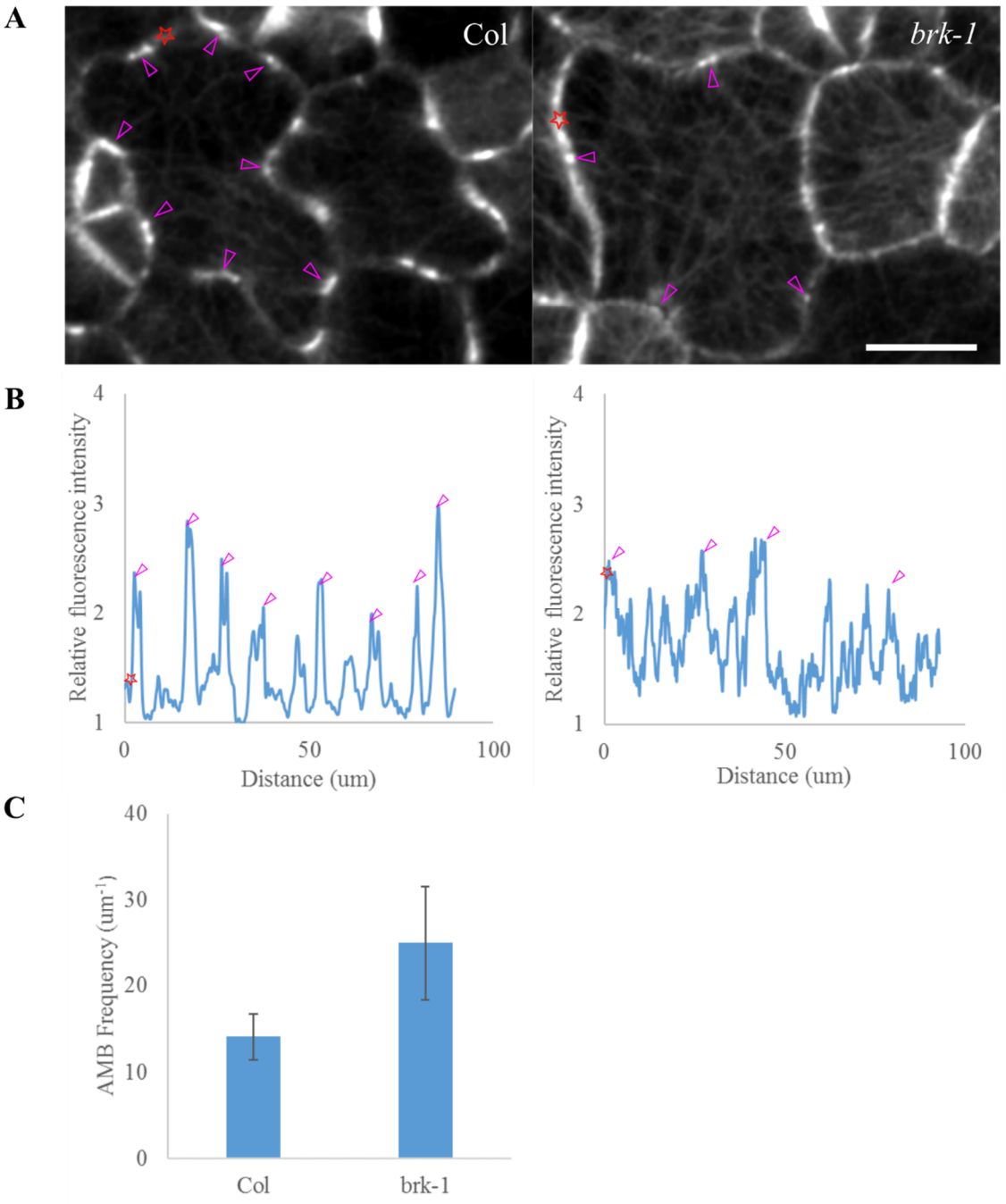

Figure 3.3 The brk-1 mutant exhibits AMB defects.

(A) examples of AMB bundles in both wild type and the *brk-1* mutant. Purple arrowheads label the AMB, and red stars mark the beginning of quantification of (B). Scale bar is 10 µm. (B) quantification of MT relative fluorescence intensity at the periclinal edge. To adjust the fluorescence intensity, MT fluorescence value was uniformed by minimal value and the ratio value reflects fluorescence relative intensity. (C) quantification of AMB frequency along the periclinal edge. Pavement cells with lobe were measured. For wild type, n=30 cells, 219 AMBs; for the *brk-1* mutant, n=30 cells, 143 AMBs.

3.2.4 CMTs exhibit strong alignment in the *brk-1* mutant.

Given that the *brk-1* mutant exhibits AMBs formation defects, and AMBs converge CMTs at the periclinal wall, I checked CMT organization in *brk-1* mutant leaves. Intriguingly, the CMT array in pavement cells in the *brk-1* mutant was highly aligned into parallel arrays while MT arrays in the wild type were organized more heterogeneously (Figure 3.4A). To quantify this, I measured CMT angles in both wild type and *brk-1* mutant leaf pavement cells and used the standard deviation of CMT angles as a measure of array order ((Chi and Ambrose, 2016);20 cells for each were sampled, see Methods section for CMT angle measurement). Consistent with the observation, periclinal CMTs in *brk-1* mutant showed a narrower range in standard deviations of MT angle, indicating a higher level of alignment compared to wild type, where the distribution of standard deviations was relatively broader (Figure 4.4B and C).

Given the results of the *brk-1* mutant exhibiting fewer AMBs, it is possible that the reduction of cell lobing in the *brk-1* mutant cells is due to MT defects, not actin defects. AMBs connect CMT and anticlinal MTs and converge them together. Due to the loss of AMBs, I think that CMTs in the *brk-1* mutant failed to form mixed orientations, which are necessary for multipolar growth.

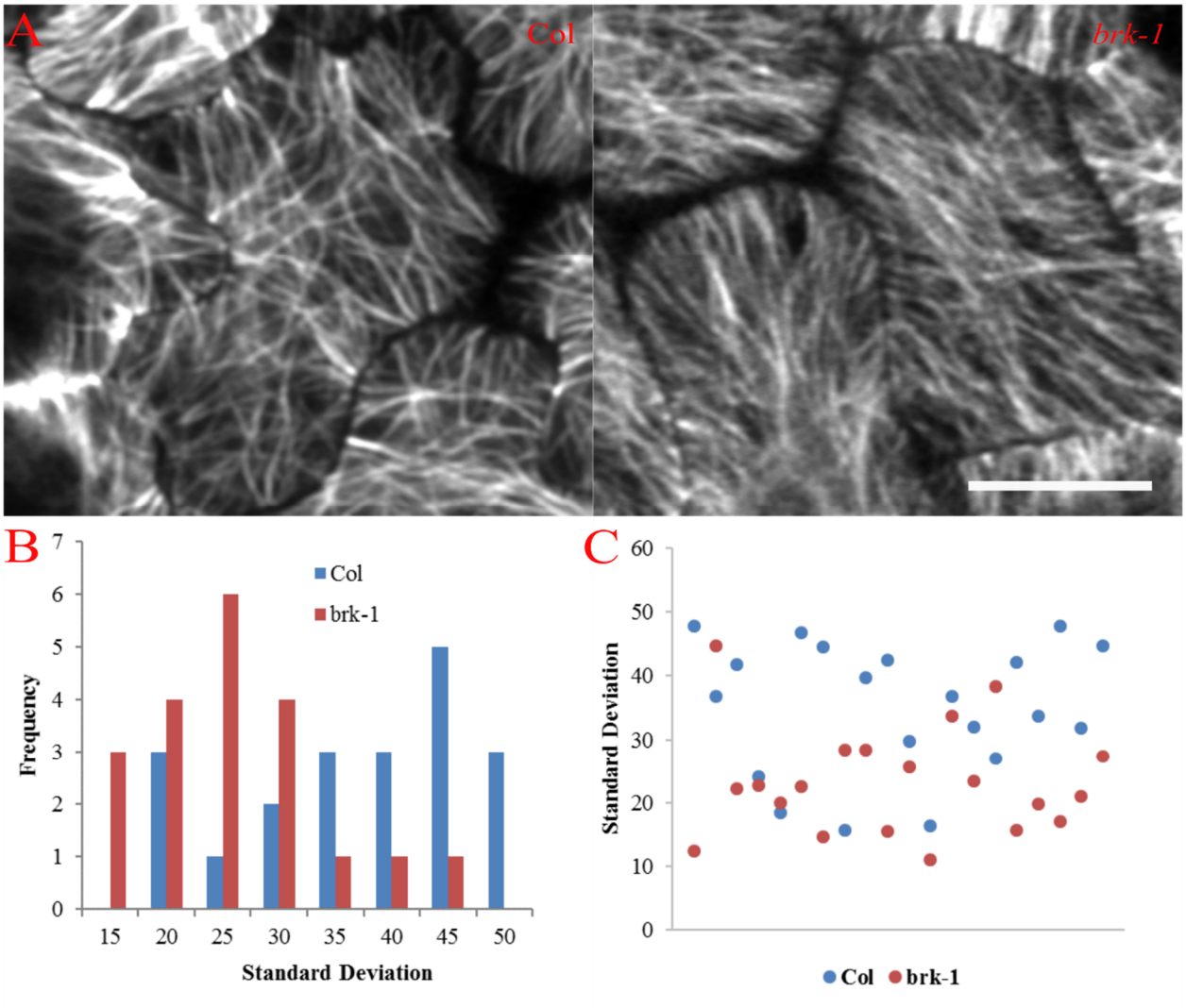

Figure 3.4 CMTs in the brk-1 mutant exhibit strong alignment.

(A): examples of MT array order in both wild type and the *brk-1* mutant. (B) and (C) quantification of MT array order in both wild type and the *brk-1* mutant. Scale bar is 10 µm.

3.2.5 CMTs array orientation in leaf pavement cells are more dynamic in the *brk-1* mutant.

MTs overall orientation in a cell changes even in lobed pavement cells, which might indicate a relationship between the orientations of both mechanical forces generated during cell expansion and CMT alignment (Sampathkumar et al., 2014b). For example, according to Figure 3.5A, the main CMT orientation changed from horizontal to vertical within one hour. Since the AMBs connect CMTs and anticlinal MTs and are stable over time, the loss of AMBs in the *brk-1* mutant would facilitate the MTs orientation change. In that case, CMTs would exhibit higher level of

dynamics. To verify that notion, CMTs orientation change was quantified in 30 wild type and the *brk-1* mutant cells, respectively. With the Fibril Tool plugin in Image J, the overall cell-wide orientation of CMT array was measured. Compared to MT arrays in wild type, which generally showed a small angle change, the MT arrays in the *brk-1* mutant exhibited a bigger angle change within the same period (Figure 3.5C). Therefore, compared to wild type, MT orientation changed more frequently in the *brk-1* mutant pavement cell.

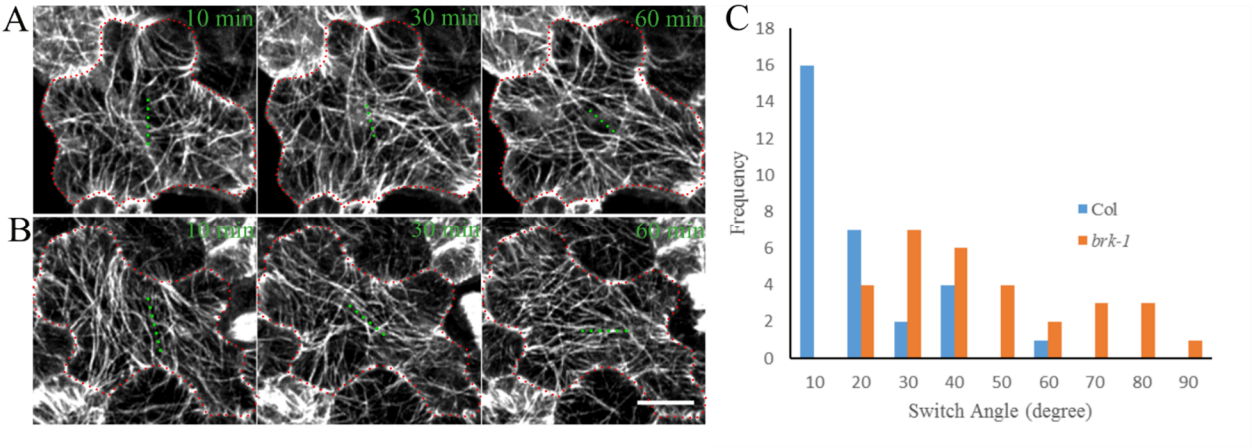

Figure 3.5 MT orientation in the brk-1 mutant change more frequently.

(A) and (B) MTs orientation change within one hour in wild type and the *brk-1* mutant respectively. Yellow broken line label the main orientation of MT array. Scale bar is 5 µm. (B) quantification of angle change in one hour in both wild type and *brk-1* mutant.

3.2.6 Pavement cells fail to avoid four-way junction in the *brk-1* mutant.

Previous analysis of asymmetric cell division (ACD) patterns during stomatal development in the maize *brk-1* mutant demonstrated that the mutation of BRK1 leads to actin patch defects, failed nuclear migration, and hence the failure of asymmetric cell division (Panteris et al., 2006). Considering the same function and similar phenotypes of *brk-1* in Arabidopsis, and the role of actin in cell division plane orientation (Vaskebova et al., 2018), it is conceivable that the Arabidopsis *brk-1* mutant might show cell division defects too. Intriguingly, during the analysis of cell shape in epidermal cells in the *brk-1* mutant, I noticed that there were lots of four-way junctions (Figure 3.6A). Avoidance of four-way junction is a recognized feature of plant cells, and

is thought to increase structural stability (Lloyd, 1991). To avoid four-way junction, during cytokinesis, cells with neighboring cell walls will shift the PPB and phragmoplast and then cell plate a bit, which will avoid the formation of the four-way junction (Figure 3.6A), while in Arabidopsis *brk-1* mutant the tilt of cell plate did not occur. To quantify the frequency of four-way junction in the *brk-1* mutant, junctions in cotyledon from both wild type (3680 junctions in 8 samples) and the *brk-1* mutant (2650 junctions in 6 samples) were examined. According to Figure 4.6B, the four-way junction frequency in wild type was obviously higher than the *brk-1* mutant. So far, the avoidance mechanism for four-way junction remains unclear yet (Flanders et al., 1990; Martinez et al., 2018), the aberrant increase of four-way junction in the *brk-1* mutant suggest an important role of BRK1 in the avoidance mechanism.

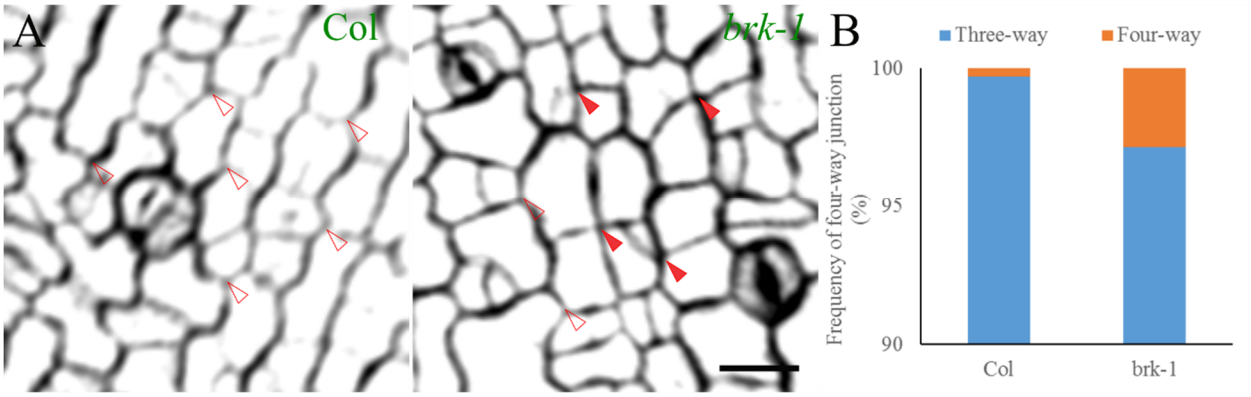

Figure 3.6 The failure of four-way junction avoidance in the brk-1 mutant.

(A) cell profiles in cotyledon in both wild type and the *brk-1* mutant. Sold red arrowheads point out the four-way junction and hollow red arrowheads point out the avoidance of four-way junction. Scale bar is 25 µm. (B) Quantification of four-way junction percentage in both wild type and the *brk-1* mutant.

3.2.7 Pavement cells exhibit asymmetric division defect in *brk-1* mutant.

Because the bulk of cell divisions in the leaf epidermis function in guard cell formation, it is plausible that the observed cytokinetic defects may be due to failed asymmetric cell divisions in the guard cell pathway. By monitoring MT structure during asymmetric division over the course of hours, I found that near 30% of asymmetric division events in epidermal cells of the *brk-1* mutant failed and ended as symmetric divisions.

More intriguingly, for the failed asymmetric division events, all of them exhibited nucleus migration defects (Figure 3.7B). As a series of former reports proved, during asymmetric division, the nucleus will migrate toward the future meristemoid cell and stay either around or pass the PPB (Figure 3.7A). The nucleus migration in maize was thought to result from the actin patch defect. However, in Arabidopsis *brk-1* mutant, some nuclei failed to migrate toward the future meristemoid cell, which might lead to the failure of asymmetric division (Figure 3.7B). Therefore, the observed cytokinesis defects in the *brk-1* mutant suggest an important role of BRK1 in orienting cell plate and guiding the nucleus. To quantify the observation, 15 complete asymmetric division events were observed in the first true leaf in the *brk-1* mutant and 5 of them exhibited nucleus migration defects whereas in wild type none of them showed similar defects.

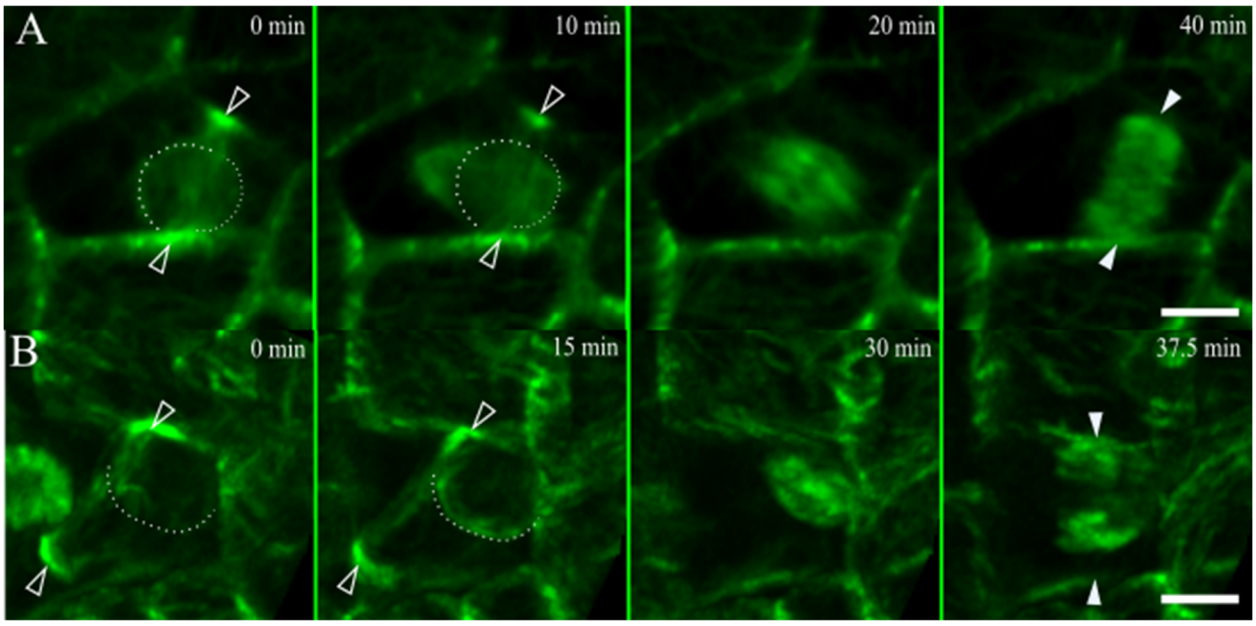

Figure 3.7 Pavement cell lineage in the *brk-1* mutant exhibits ACD related defect.

(A) an asymmetric division in wild type, (B) a failed asymmetric division in the *brk-1* mutant. White broken lines outline the nucleus, solid arrowheads mark phragmoplast and arrowheads mark PPB. Scale bar is 5 μm.

3.2.8 The *brk-1* mutant exhibits cytoplasmic defect.

In addition to plant cell shape regulation, F-actin is also involved in vacuole morphogenesis. Acting as a framework, F-actin associates with cytoplasmic strand and support its formation,

rearrangement and movement (Higaki et al., 2006). Moreover, actin nucleation system, especially the Arp2/3 is reported to regulate vacuole fusion in stomata (Li et al., 2013).

During my observation of MT dynamics in the *brk-1* mutant, I noticed striking abnormalities in the cytoplasmic organization and dynamics. In a typical plant cell with a large central vacuole, the cytoplasm is mostly appressed against the cell cortex, with occasional cytoplasmic strands running through the vacuole (i.e., transvacuolar strands). This was the case for wild-type leaf epidermal pavement cells. In the *brk-1* mutant, the cytoplasmic strands were enlarged greatly (often losing their "strand-like" morphology) and there was more internal cytoplasm in general, suggesting possible defects in vacuole function and/or loss of cytoplasmic integrity (Figure 3.8A). To verify the phenotype, vacuoles were quantified by measuring the vacuolar morphology index of the largest vacuole in a pavement cell (Figure 3.8B). The vacuolar morphology index was a value calculated by multiplying its longest and widest distance value (Lofke et al., 2015). According to Figure 3.8B, the *brk-1*pavement cells exhibited smaller vacuole morphology index than the wild type.

Time course analysis revealed that the internal cytoplasm was also much more mobile, and had more dynamic shape changes than those in wild type. For this experiment, I conducted a time course in 18 mins with 6 mins as time interval. Using ImageJ, maximum Z-projections were made for each timepoint, and then all three timepoints of these Z-projection were defined as different color and flattened into a single image using the Temporal Color Code function in ImageJ (Figure 3.8C). Generally, if the cytoplasm is stable, fewer strand mixture will be observed, but if they are highly dynamic, more strand mixture with different colors will be observed. Consistent with my notion, compared with wild type, the cytoplasmic strands in the *brk-1* mutant exhibited higher dynamics by showing a big size of mixed color strands, corresponding to a rapid movement and shape changes in cytoplasmic morphology strands. Therefore, the mutation of *Brk-1* affects cytoplasmic/vacuolar formation and movement, which would be consistent with a role of BRK1 in actin organization, as the actomyosin system is the primary controller of these processes.

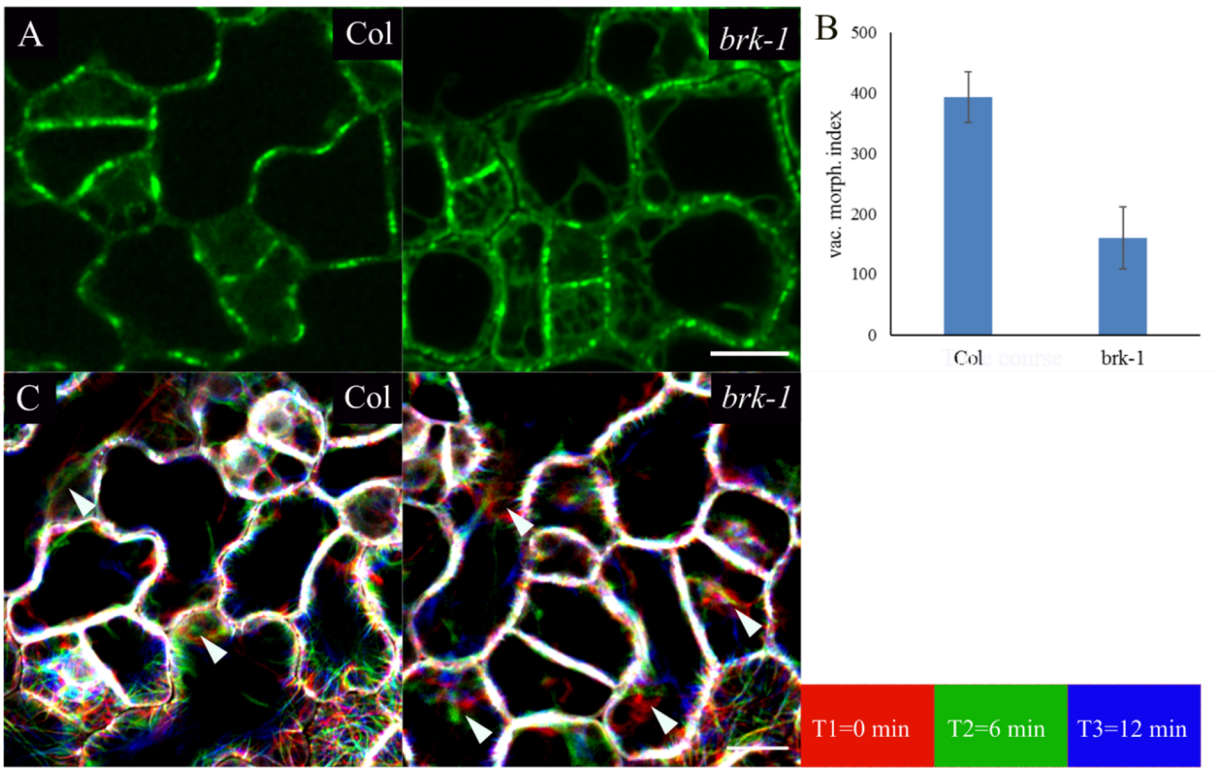

Figure 3.8 The *brk-1* mutant exhibits a cytoplasmic defect.

(A) Cytoplasm in both wild type and the *brk-1* mutant expressing *UBQ1::GFP-TUB6*. Scale bar is 10 µm. (B) Quantification of vacuolar morphology index. The index is defined as the largest luminal structure size by measuring the largest length and width and multiplying the values. n=30 cells for each. (C) Time course of cytoplasmic dynamics in both wild type and the *brk-1* mutant. Three timepoints are shown, each timepoint given a different color, and overlaid as a sum projection. The color pallet is on the right. Arrowheads point cytoplasmic strand mixture. Scale bar is 10 µm. Color bar correlates with cytoplasmic strand in different timepoint.

3.3 Discussion

In this chapter, I presented several cellular abnormalities in the *brk-1* mutant. In *brk-1* pavement cells, fewer AMBs form, CMT tend to strongly align in parallel and CMTs change orientation more frequently. Collectively, these defects may explain the reduction of cell lobing in the *brk-1* mutant.

The question is, does BRK1 act directly on MTs, or indirectly through its role in actin nucleation? While no obvious abnormalities in actin organization in the *brk-1* mutant were observed, this is based on static images and will require fine-scale analysis of F-actin dynamics in the *brk-1* mutant.

The abnormalities about AMBs and CMTs in the *brk-1* mutant were similar to the previous report of Lat B treatment on wheat mesophyll cells (Wernicke and Jung, 1992). In my experiment, the same influence of Lat B on AMBs was also observed in Arabidopsis pavement cells (Data not shown). Considering that F-actin forms a board cortical band encompassing the PPB as it narrows, and is required for PPB narrowing (Liu and Palevitz, 1992), it's conceivable that like PPB formation, AMBs formation is controlled by F-actin, which explains the AMB formation defect in the *brk-1* mutant. However, I have not found any PPB narrowing defect in the *brk-1* mutant.

Spanning the anticlinal wall, AMBs connects and converges CMT and drive the lobe initiation. Given the superparallel CMT and increased CMT orientation change, it is possible that CMT, especially CMT arrays are stabilized due to the formation of AMBs. By converging CMTs, AMBs mixes CMT on the outer periclinal wall and the stable AMBs partially prohibits CMT orientation change. Given that AMBs are stable over time in pavement cells, the formation of AMBs stabilizes CMT it connected. On the other hand, the local AMBs orchestrate global MT patterns (both CMTs and anticlinal MTs), which mimic the function of MTOCs.

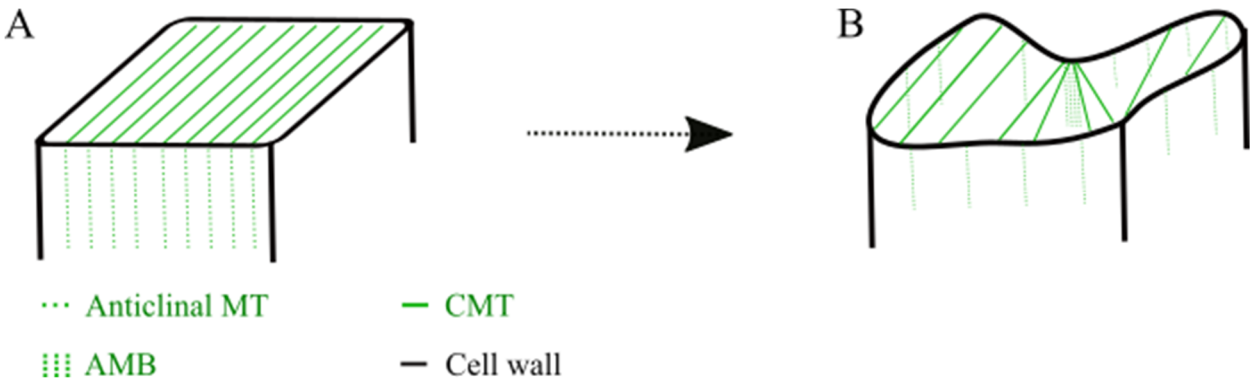

Figure 3.9 Schematic model of AMB formation.

A to B schematic depicting AMB formation during lobe formation: (A) newborn pavement cell; (B) pavement cell with initiated lobe formation.

Through re-assessing the cell lineage in cotyledon in the *brk-1* mutant, I realized that there is the cell plane orientation defect, which exhibits as a failure of four-way junction avoidance. This phenotype renders cell adhesion weaker and the cell structure less stable (Goodbody et al., 1991). Based on our results, I hypothesized that this defect is associated with the abnormal MT dictated

cell plane orientation. Moreover, the notion was further confirmed by the results that the *brk-1* mutant showed failed cell plane re-orientation and appropriate nucleus migration during asymmetric division. Considering actin patch in maize migrates nucleus to trigger the asymmetric division while similar mechanism has not been reported in Arabidopsis, it would be interesting to further investigate the possible mechanism for actin-involved cell plane orientating and nucleus migration (Panteris et al., 2006).

In addition to plant cell shape regulation, F-actin is also involved in vacuole morphogenesis. Acting as a framework, F-actin associates with cytoplasmic strand and support its formation, rearrangement and movement (Higaki et al., 2006). Moreover, actin nucleation system, especially the Arp2/3 is reported to regulate vacuole fusion in stomata (Li et al., 2013).

3.4 Materials and methods

3.4.1 Plant materials and growth conditions.

Arabidopsis thaliana ecotype Columbia 0 (Col-0) was used as wild type in this study. The transgenic line *UBQ1:: mRFP–TUB6* was described previously (Ambrose et al., 2011). *UBQ1:: mRFP–TUB6* was introduced into transgenic *brk1* expressing *BRK1:: BRK1-YFP* through crossing. The F-actin marker line *35S::GFP-ABD2-GFP* and *35S::Lifeact-Venus* were obtained from the Y. Wei lab (University of Saskatchewan). Both lines were introduced into the *brk1* mutant through crossing.

Seeds were sterilized with 70% ethanol, rinsed five times with sterilized water and plated onto Petri dishes containing ½ MS media, 1.0 % agar, 1 % sucrose and pH is 5.7. Plates were wrapped with parafilm (Bemis Inc.) and transferred to a 21 °C growth cabinet (with continuous light) and placed in the rack vertically. Young root, hypocotyl and cotyledon were imaged at 3–4 days after germination, and true leaf cells were imaged at 4–5 days after germination.

3.4.2 Tissue preparation and microscopy.

All observations were performed on living cells. For true leaf imaging, cotyledons were cut off at the base with fine scissors and the rest of seedlings were mounted. All the tissue samples were mounted in Nunc chambers (Lab-Tek) with Perfluoroperhydrophenanthrene (PP11) and covered by 2~3-mm-thick 0.7% Phytagel. All CLSM images were obtained via point-scan confocal microscopy: Zeiss Meta 510 with Zeiss Axiovert 200M microscope, 63X water immersion and

Zeiss 880 with Airyscan, both 40X and 63X water immersion. GFP fluorescence was detected with an excitation wavelength of 488nm from an argon laser and captured with emission wavelength of 495 – 550nm. LifeAct-Venus fluorescence was detected with an excitation wavelength of 488nm from an argon laser and captured with emission wavelength of 495 – 550nm. YFP was detected with an excitation wavelength of 514nm from an argon laser and captured with emission wavelength of 495 – 550nm. RFP was detected with an excitation wavelength of 543nm from an argon laser and captured with emission wavelength of 575 – 620nm. PI was detected with an excitation wavelength of 514nm from an argon laser and captured with emission wavelength of 570 – 640nm. The Z-stack interval varies from 0.2 μm to 0.4 μm. For sampling, more than 5 cotyledons or first pair of true leaves were picked and more than 10 cells for each sample were imaged.

3.4.3 Image analysis.

Images were processed with Image J software (http://rsb.info.nih.gov/ij/). The ClearVolume plugin (https://imagej.net/ClearVolume) (Royer et al., 2015) from Image J and Fluorender (http://www.sci.utah.edu/software/fluorender.html) (Wan et al., 2009) were used for 3D renderings and Fibril Tool plugin was used for CMT orientation analysis (Boudaoud and Burian, 2014). Figures were assembled using Corel Draw software (www.Corel.com; Corel System. Ottawa, ON, Canada), and Inkscape vector graphics software (www.inkscape.org). Statistical analysis was performed using Microsoft Excel (Microsoft, Edmond, WA).

3.4.4 CMT angle and array order measurements

For quantification of CMT array order, images were sampled by using five evenly-spaced horizontal rectangular boxes that were 2 μm high and as wide as the image. The narrow height was used to remove any ambiguity of MT angle that may arise due to MTs that are bent to varying degrees. MT angles were defined relative to the horizontal axis of the image. For this, a central area of the cell (away from edges) was sampled for up to 30 MTs.

3.4.5 PI staining.

To label the cell wall, Propidium Iodide (PI) (Invitrogen) was used. Four or five-day-old seedlings were incubated with 100μg/ml PI in 1.5ml Eppendorf tube and then centrifuged at 3381g for 1min. After centrifugation, keep incubating for 20 mins at room temperature. Stained samples were rinse gently with distilled water, mounted with PP11, and imaged in chambers as above.

Chapter 4 BRK1 is associated with plasmodesmata

4.1 Introduction

4.1.1 PD and pit field

To communicate with each other, neighboring cells form connecting channels such as gap junctions in animals and plasmodesmata (PD) in plants. According to their biogenesis mechanism, PDs can be classified into two types: during cytokinesis, endoplasmic reticulum left in the forming cell plate forms primary PDs while the secondary PDs are formed later in existing cell walls through cell wall thinning and plasma membrane insertion during cell expansion (Faulkner et al., 2008; Knox and Benitez-Alfonso, 2014). During cell growth, PDs tend to aggregate together in the certain region of cell wall termed as pit field.

Morphologically, the PD structure varies from a simple pore to branched structures (Faulkner et al., 2008; Fitzgibbon et al., 2013). PDs undergo dynamic changes to accommodate developmental and environmental signals. This includes changes in diameter and closing completely. To modulate the PD structure change, both cell wall mechanics and composition are modified: the cell wall surrounding PD is enriched with callose and specific pectins and reduced in cellulose (Faulkner et al., 2008). Series of analysis reported a preferential localization of both low-esterified pectin and related enzyme around PD region (Morvan et al., 1998; Orfila and Knox, 2000; Faulkner et al., 2008). Consistent with its function to glue cell wall components, low-esterified pectin insertion facilitates movement of things through PD by regulating PD aperture. Those observations were further confirmed by PD proteome analysis results, which identified a number of candidates involved in pectin biosynthesis and remodeling (Fernandez-Calvino et al., 2011; Knox and Benitez-Alfonso, 2014). Even though, the mechanism of specific pectin distribution around PD and its function is still an open question.

F-actin is associated with PD and implicated in trafficking through PD. To support the notion, actin was reported to localized to PD (Radford and White, 1998; Wang et al., 2002; Faulkner et al., 2009; Dong et al., 2011). Moreover, due to the technical barriers, the function of F-actin in the regulation of PD remain largely unknown. It's been suggested that F-actin was implicated in the PD-mediated trafficking regulation, which may be through regulation of permeability of PD (Su et al., 2010; Fernandez-Calvino et al., 2011). It's until recently, an actin nucleator —Formin 2 (FH2)—was found to localize with PD and mutation of FH2 leads to increased PD permeability

(Diao et al., 2018). Instead of nucleating actin, FH2 caps and stabilizes F-actin, which may facilitate F-actin anchoring and stabilization at PD (Diao et al., 2018).

4.1.2 Pectin and cell growth

Composed of a diverse class of galacturonic acid-rich polysaccharides, pectins are one of the most complicated cell wall components in nature and fulfill various functions such as morphogenesis, cell-cell adhesion, pit field formation and signaling (Ridley et al., 2001; Willats et al., 2001a).

Based on structure and function, five classes of pectins were reported: homogalacturonan (HG), xylogalacturonan (XGA), apiogalacturonan (AP), and rhamnogalacturonan I and II. Among them, HG is the prevalent pectin component and undergoes considerable chemical modification once it's deposited in the cell wall (Caffall and Mohnen, 2009). After polymerized in *cis* Golgi, HG is methyl-esterified in medial Golgi, substituted in *trans* Golgi and secreted in a highly methyl-esterified form (Zhang and Staehelin, 1992; Sterling et al., 2006). Methyl-esterified HG is transported to the wall and modified depending on the cell context.

The degree of methyl-esterification is critical to cell wall structure because generally highly methyl-esterificated HG often leads to decreased stiffness of cell wall structure while a low level of methyl-esterification associates with stiffer cell wall (Braybrook and Peaucelle, 2013). Exception also was reported as the highly methyl-esterified pectin linked with soft cell wall (Palin and Geitmann, 2012). Moreover, de-methyl-esterified HG can cross-link with calcium and further rigidify the cell wall structure (Liners et al., 1989). Thus, a low level of methyl esterification is often associated with reduced wall elasticity (Braybrook and Peaucelle, 2013). Interestingly, recent studies on pectin found that selective de-methyl esterification occurs before MT re-orientation, which indicated a predominant role of pectin on cell expansion (Peaucelle et al., 2015).

Various of immunostaining results confirm the enrichment of pectin (HG) at the pit field (Casero and Knox, 1995; Orfila and Knox, 2000). Interestingly, the biochemical status of HG accumulated in the pit field was identified as low methyl-esterified (Orfila and Knox, 2000). The HG-rich property of pit field is consistent with PD insertion and enlargement without causing major change to the cell wall structure.

Given that the *brk-1* mutant root exhibiting abnormal intercellular junction (Dyachok et al., 2008) and the role of F-actin in vesicle delivery of cell materials (including pectin), I hypothesized that

the cell adjunction in pavement cells could exhibit cell adhesion defect, which is vesicle trafficking-related. Since an actin nucleator –Formin2 was reported to co-localize with PD (Diao et al., 2018), I hypothesized that BRK1 could also associated with PD too.

4.2 Results

4.2.1 The *brk-1* mutant exhibits cell wall junction defects in leaf cells.

Given the three-way-junction localization pattern of BRK1-YFP and the junction defects in the *brk-1* mutant, it is conceivable that the mutation of BRK1 could lead to cell junction change. To verify that idea, a reporter line — YFP-Glycosylphosphatidylinositol-Anchored Lipid Transfer Protein (YFP-LTPG)—was crossed into *brk-1* mutant to examine the cell geometry. As an apoplastic protein, LTPG is secreted into the cell wall. In wild type, LTPG signal distributed along the anticlinal wall, showing enrichment in lobed regions and exclusion from the three-way junction (Figure 4.1A) (Ambrose et al., 2013). In contrast, YFP-LTPG accumulated strongly at the three-way junctions in the *brk-1* mutant (Figure 4.1A). To further confirm that, the intensity of signal fluorescence was quantified and compared (Figure 4.1B). Compared to wild type with a uniform distribution of LTPG signal along cell outline, *brk-1* mutant exhibited steep fluorescence peak at the three-way junction, indicating a prominent accumulation of YFP-LTPG. These results suggest a weakening or thinning of the three-way junction, and are consistent with my localization data showing BRK1-YFP enriched at the anticlinal cell edges that comprise a three-way junction.

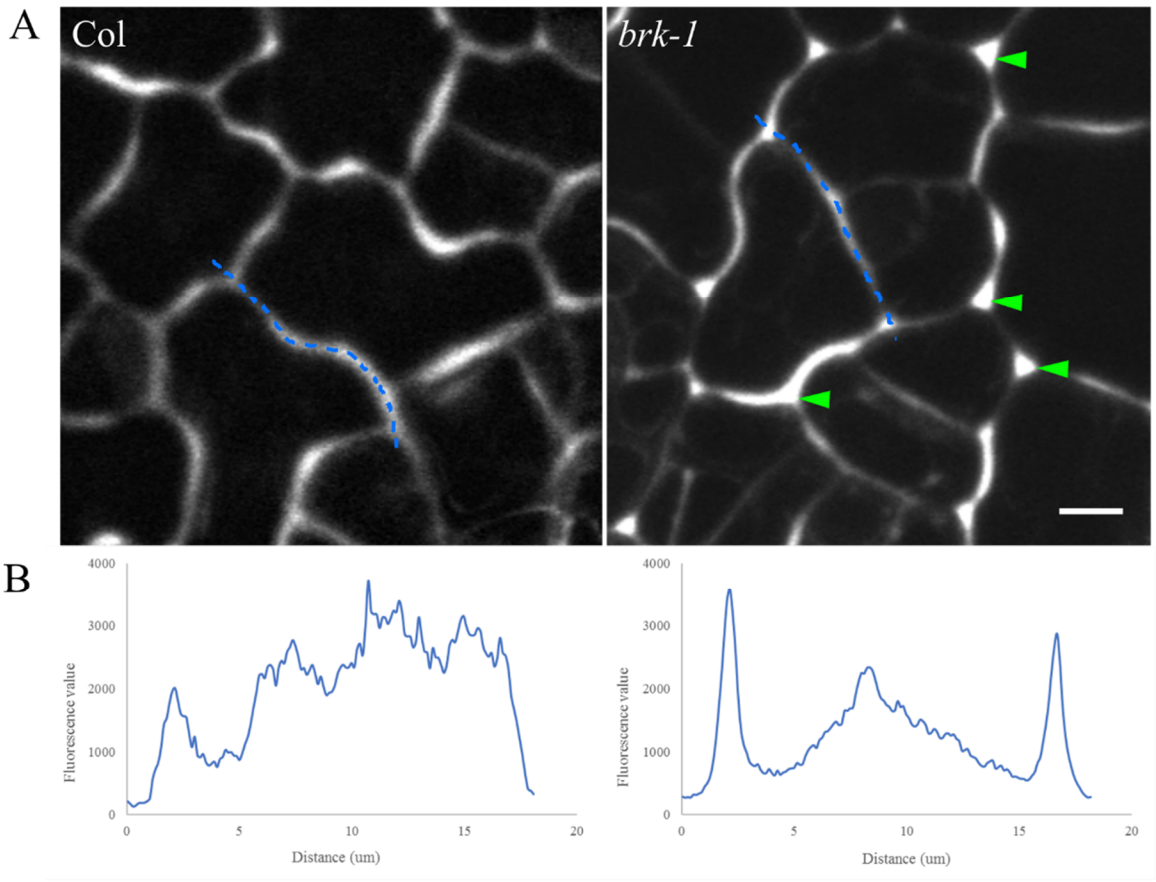

Figure 4.1 LTPG-YFP enriches in the three-way junction in the brk-1 mutant.

(A) examples showing an aberrant accumulation of LTPG in the three-way junction in the *brk-1* mutant. Green arrowheads denote the three-way junction with LTPG accumulation. Blue broken lines correspond to the quantification result in B. Scale bar is 5 µm. (B) Fluorescence intensity plots along broken blue lines in A. Intensity values are pixel grayscale level from 16-bit images.

4.2.2 BRK1 associates with actin-dependent vesicle trafficking.

In plant cells, the pectin-rich middle lamella protects cell integrity and mediate cell adhesion. The construction of middle lamella is mainly through the vesicle delivery of pectin and related proteins, which is actin-dependent (Micheli, 2001; Willats et al., 2001b; Daher and Braybrook, 2015). Combining with the above results of YFP-LTPG-labeled cell junction defect, it was conceivable that the vesicle trafficking in the *brk-1* mutant might be disturbed. To verify that notion, I treated both wild type and *brk-1* mutants with Brefeldin A (BFA), which blocks exocytosis, resulting in large intracellular aggregations of endoplasmic reticulum and Golgi, called BFA bodies. These are typically visualized using the endocytic fluorescent tracer dye FM4-64, which also labels plasma

membranes (Jelinkova et al., 2010). As shown in Figure 4.2A, *brk-1* mutant cells exhibited smaller BFA bodies compared to wild type. Further quantification of BFA body size in 20 cells confirmed that result, showing a roughly 40% reduction in BFA body size in the *brk-1* mutant (Figure 4.2B). Therefore, our results suggest that the mutation of *Brk1* leads to disturbed vesicle trafficking, which might affect the structure of the cell wall polymer framework, and then the cell adhesion.

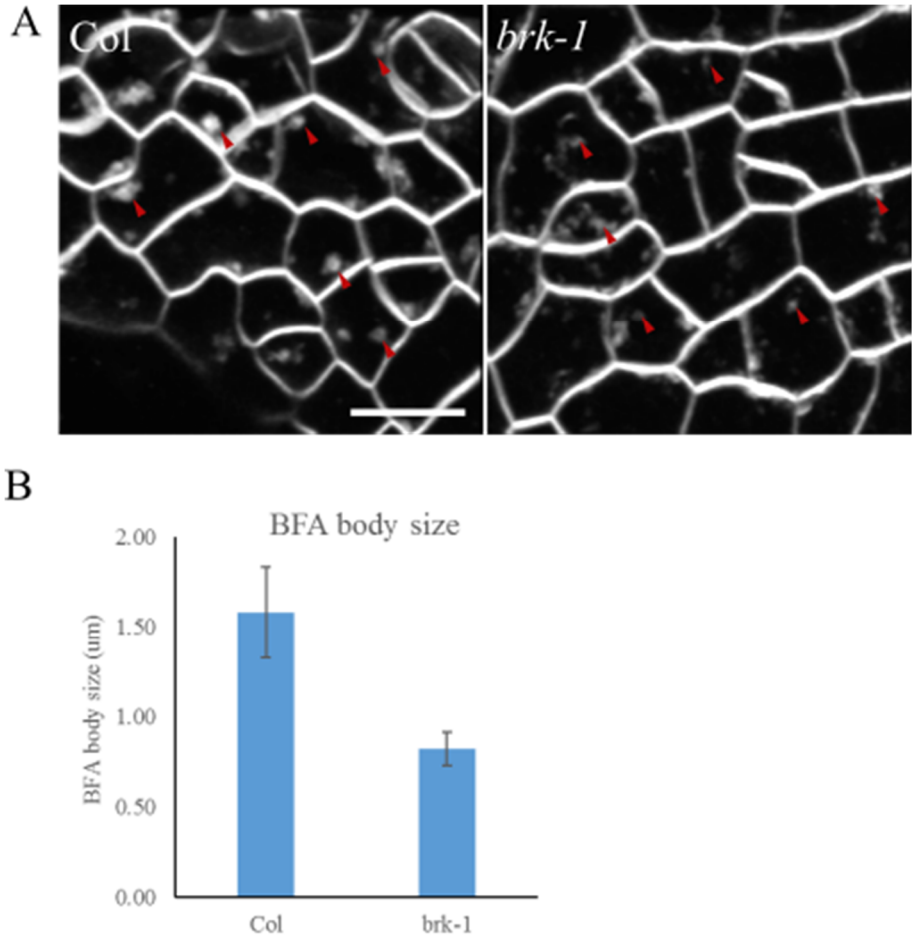

Figure 4.2 BFA body size decreases in the *brk-1* mutant.

(A) examples showing BFA body in both wild type and *brk-1* mutant after BFA treatment. (B) quantification result of BFA body size in both wild type and *brk-1* mutant after BFA treatment. Arrowheads denote BFA bodies. Scale bar is 10 μm.

4.2.3 BRK1-YFP associates with PD.

Prior characterization of BRK1 localization proved that BRK1 is localized to the plasma membrane in a SCAR-dependent way (Dyachok et al., 2008). To further investigate BRK1 dynamics on the plasma membrane, I conducted a series of plasmolysis experiment on BRK1-YFP. Consistently, after partial plasmolysis, plasma membrane detached from the cell wall and the majority of BRK1 signal particles associated with the plasma membrane (Figure 4.3A). However, a few BRK1 particles were found remaining outside of the plasma membrane, near the cell wall, and often at the three-way junction (Figure 4.3A). To verify whether the BRK1-YFP unattached from the plasma membrane, full plasmolysis experiments were performed with FM4-64 staining plasma membrane. It turns out that after full plasmolysis, some BRK1-YFP signal exhibited cell wall-associated localization at regions where FM4-64-labeled Hechtian strands attached to the cell wall (Figure 4.3C). Since the complex plasmodesmata (PD) was reported to initially insert at the three-way junction and some Hechtian strand traverse the cell wall through PD (Fitzgibbon et al., 2013; Cheng et al., 2017), it is conceivable that BRK1 associates with PD.

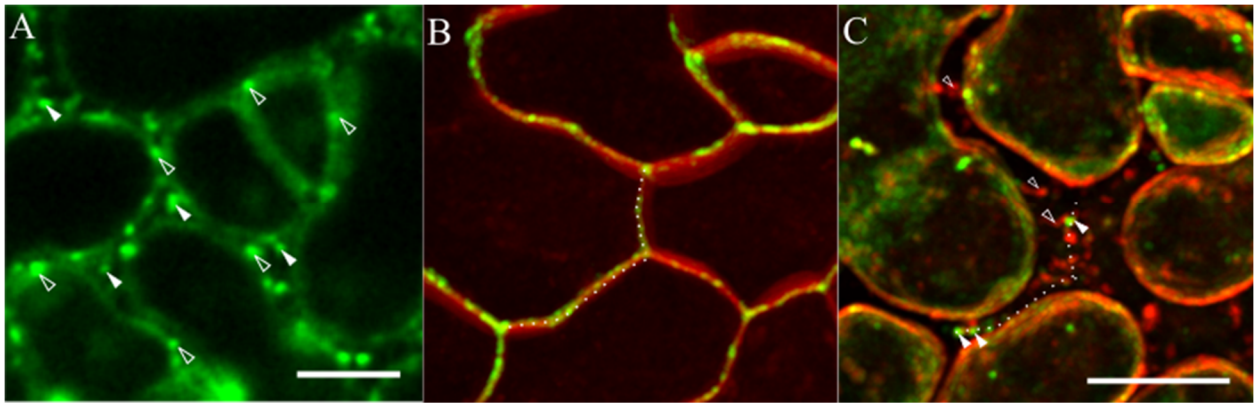

Figure 4.3 BRK1 signal pattern after plasmolysis.

(A) leaf cell with partial plasmolysis. Solid arrowheads mark the BRK1 at the plasma membrane, and hollow arrowheads point out the BRK1 at a three-way junction. (B) and (C) are same regions of leaf cells before and 9 mins after full plasmolysis respectively. Red signals are FM4-64 stained membrane and green are BRK1-YFP. Solid arrowheads mark the BRK1 associated with cell wall, and hollow arrowheads mark the FM4-64-stained Hechtian strands. White dashed lines indicate the cell wall location. Scale bar is 5 μm.

4.2.4 BRK1 signal localizes in the pit field at the anticlinal wall.

The punctate localization of BRK1-YFP to cell wall regions where Hechtian strands attach during plasmolysis suggested a possible association of BKR with PD. To determine if BRK1-YFP localized to PD, I visualized cell walls using PI staining. By examining the BRK1 signal along the anticlinal wall, I found that BRK1-YFP localized at regions where the PI staining was weaker. This was also found in mature cells of the hypocotyl epidermis (Figure 4.4) and cotyledon pavement cells (Data not shown). These regions were typically circular to roughly lenticular along the radial axis of the anticlinal walls, and are consistent with the morphology of primary pit fields (Buchanan et al., 2005). As a positive control, I used the PD marker plasmodesmata-located protein 1(PDLP1-GFP) (Thomas et al., 2008), which showed a similar pattern to BRK1-YFP (Figure 4.5). Unfortunately, I did not have time to generate lines for colocalization of BRK1 and PDLP1, but the similarity in localization pattern strongly suggests a PD localization for BRK1-YFP.

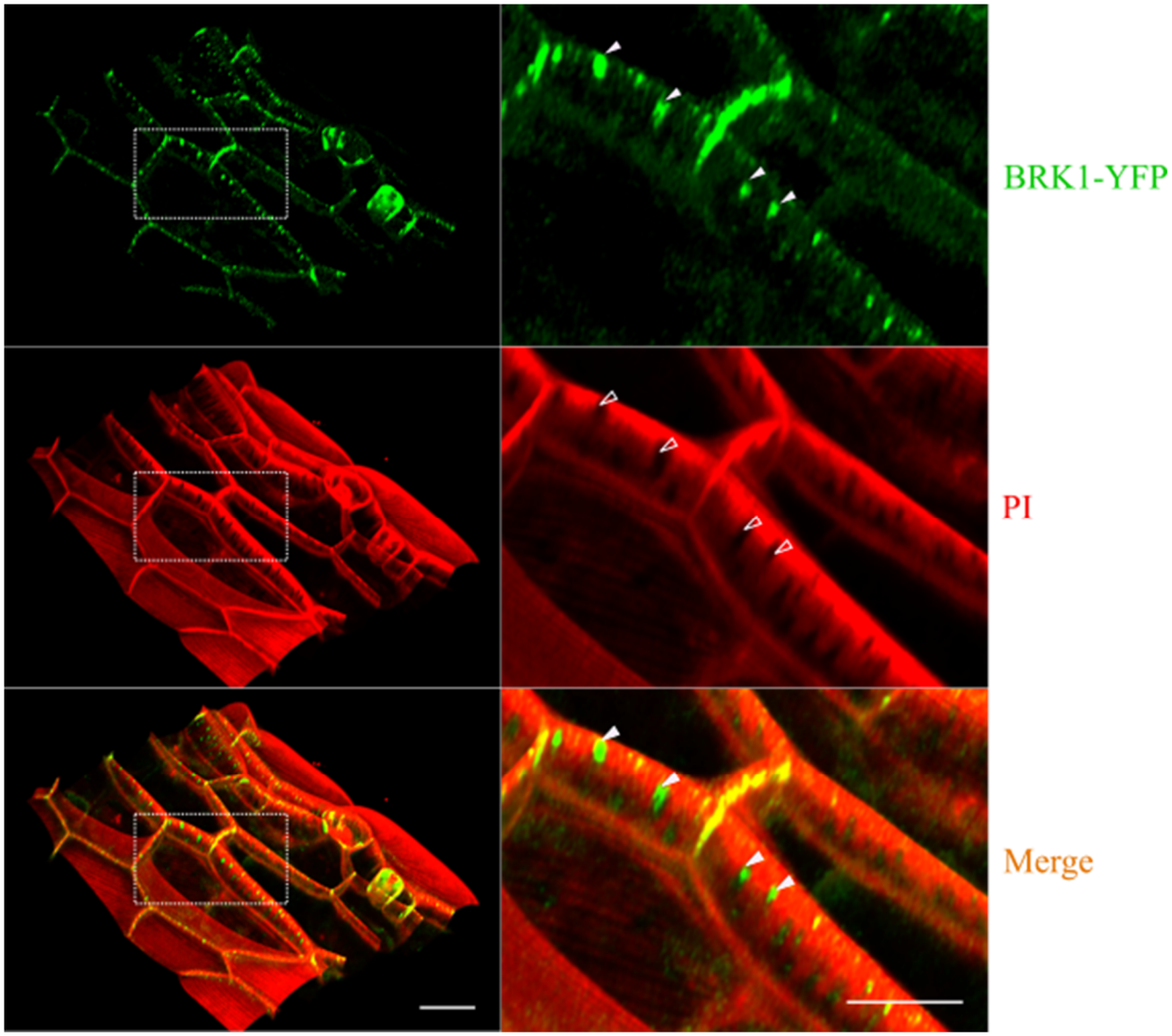

Figure 4.4 BRK1 localization at the anticlinal wall.

The left panel is hypocotyl cells with PI staining and the white box marked in the left column are enlarged in the right column. Solid arrowheads mark BRK1-YFP particles, and hollow arrowheads denote pit fields. Scale bars are 20 µm.

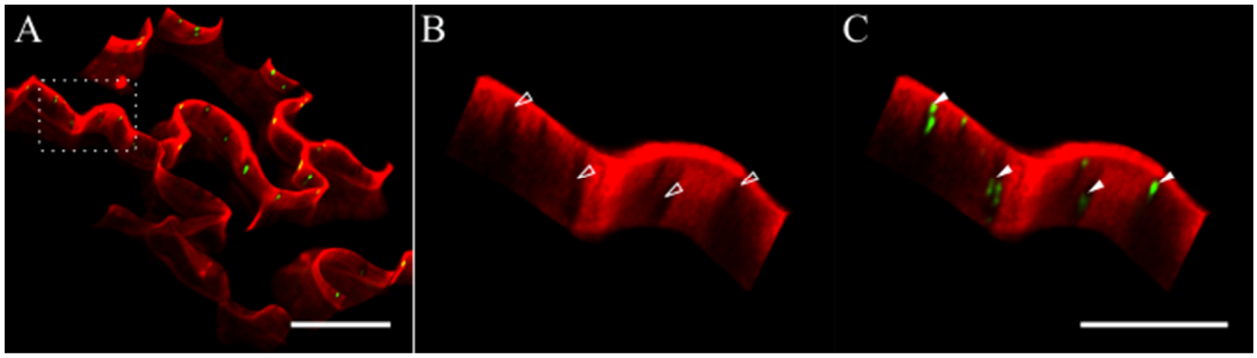

Figure 4.5 PDLP1-GFP localization at pit fields the anticlinal wall.

(A) cotyledon anticlinal walls stained with PI. Scale bar is 20 µm. The white box marked in A is enlarged at B and C. (B) anticlinal wall with PI staining. (C) PDLP1 localization at the anticlinal wall. Hollow arrowheads mark pit fields and solid arrowheads denote PDLP1-GFP. Scale bar is 10 µm.

4.2.5 Actin localizes in pit field at the anticlinal wall.

Previous studies showed F-actin at PD and crossing adjacent cell walls through PD (Dong et al., 2011; Wang et al., 2002; White et al., 1994). Since BRK1 functions in branch actin nucleation, I also checked the organization of F-actin at the pits in PI-labeled cells. Plants stably expressing the F-actin reporter *35S::ABD2-GFP* were stained with PI and imaged (Dyachok et al., 2014). Consistently, F-actin was detected in the pit regions but did not appear to be any more common than non-pit regions (Figure 4.6). This observation further supports our results of BRK1 localizing in the pit region.

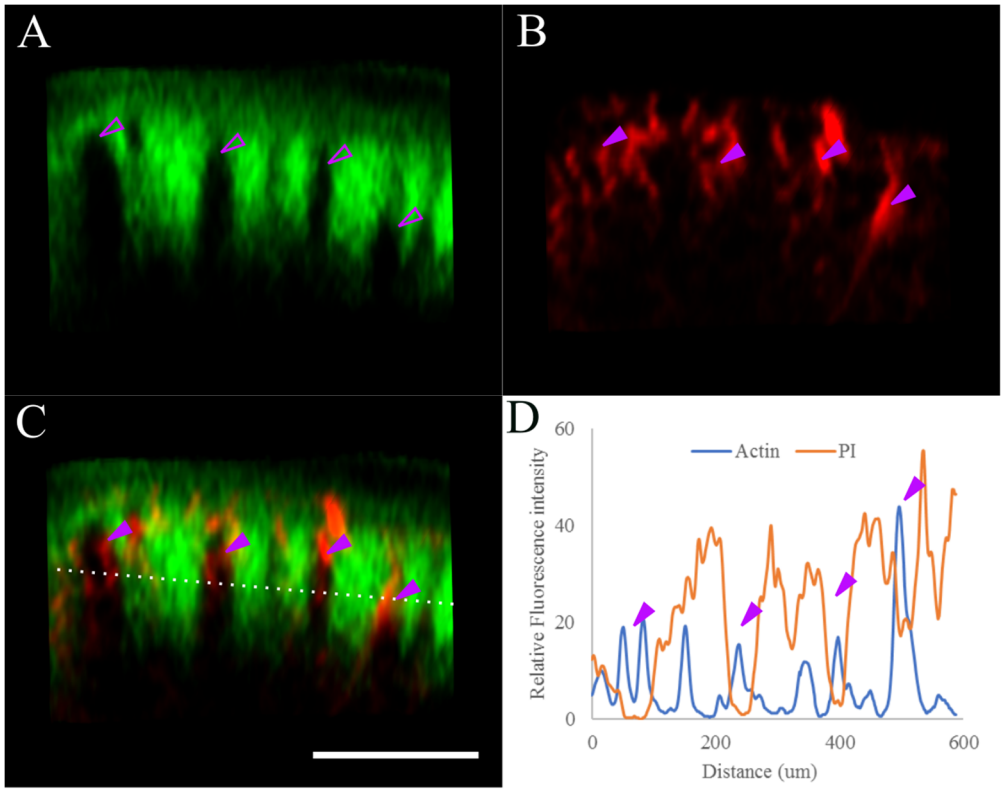

Figure 4.6 F-actin localizes in the pit region.

Hypocotyl cells stained with PI. (A) PI, (B) actin, (C) merge. Hollow arrowheads mark the pit at the anticlinal wall, and solid arrowheads label the F-actin in the pit region. Scale bar is 10 µm. (D) Quantification of fluorescence value along the white dot lines in (C). Arrowheads correspond to the one in (C).

4.2.6 MTs surround the pits area at the anticlinal wall.

In plant cell wall, anticlinal wall exhibits PD-containing pit field with microfibril surrounded in a circular way (Fujita and Wasteneys, 2014; Mueller and Brown, 1982). Since the pit field in xylem was reported to be surrounded by re-arranged MTs (Sasaki et al., 2017), it is plausible that MT could form a similar pattern around the pit area I found on the anticlinal wall. To verify that notion, MT was analyzed for their arrangement pattern on the anticlinal wall in both cotyledon and hypocotyl cells with PI staining. It turns out that in the wild type, most MTs arranged vertically along the wall, thus parallelly surrounded the pit and do not cross the pit (Figure 4.7). In the *brk-1* mutant, however, a few MT bundles came directly across the pit (Figure 4.7 A). This result was further confirmed by quantification (Figure 4.7 B).

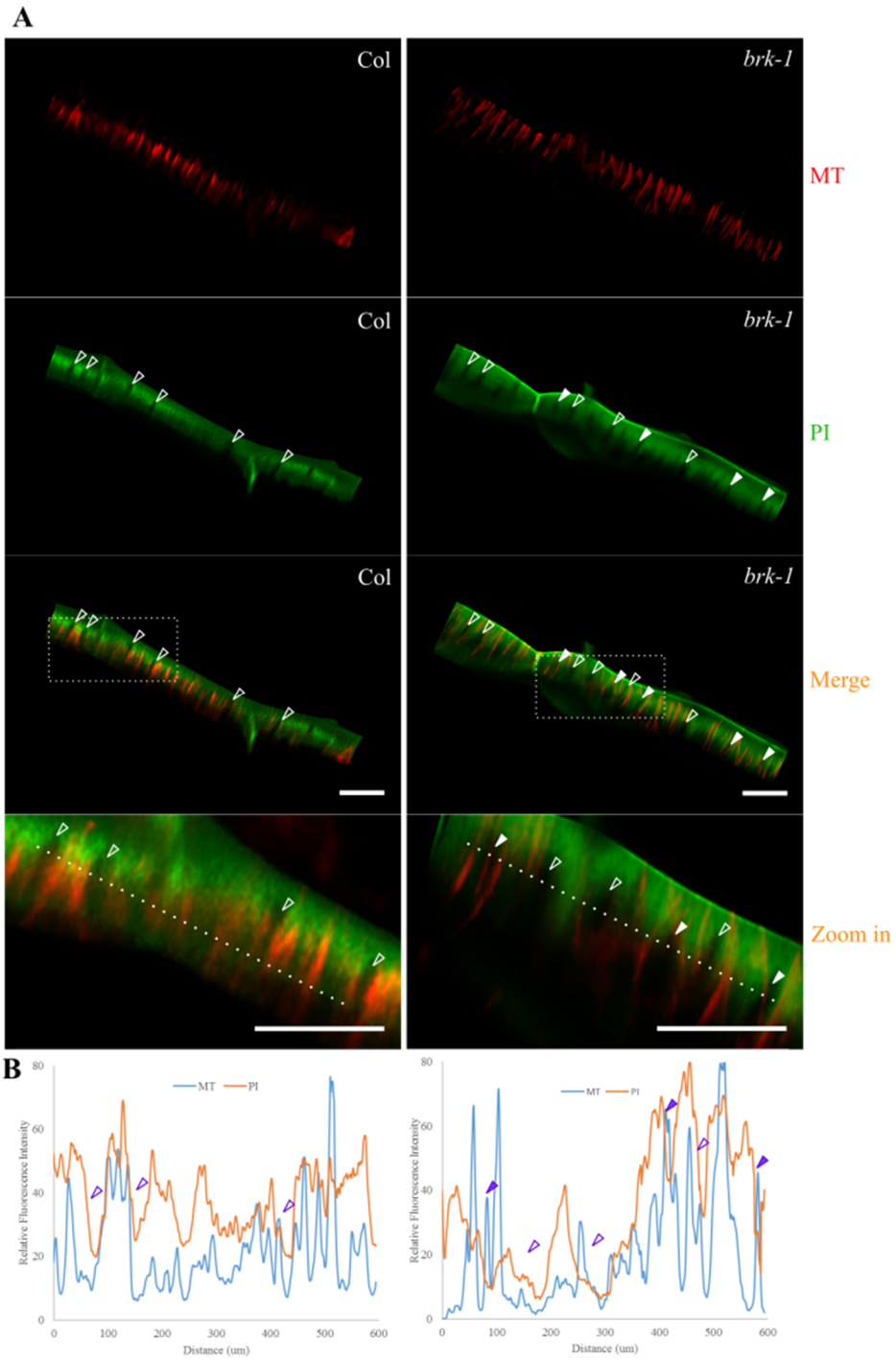

Figure 4.7 Pits were surrounded by MTs.

(A) The left panel shows the MT arrangement on the anticlinal wall in wild type and right panel in the *brk-1* mutant. Hollow arrowheads label pits with MT surrounding it and solid arrowhead points pits with MT crossing it. The white boxes marked in both columns are enlarged in the bottom. Scale bar is 20 µm. (B) Quantification of fluorescence value along the white dot lines in (A). Arrowheads correspond to the one in (A).

4.3 Discussion

During cell expansion, pectin undergoes dramatic modification to remold cell wall texture and mechanic property, and the modification is mainly through methyl-esterification (Pelloux et al., 2007). After transported to the cell wall, pectin is non-uniformly de-methyl-esterified to soften local cell wall (Braybrook and Peaucelle, 2013). Moreover, de-methyl-esterified pectin can cross-link with calcium and further rigidify the cell wall structure (Liners et al., 1989). Interestingly, recent studies on PI found that PI could compete with calcium to bind with pectin (Rounds et al., 2011). In my experiments, after the PI staining, pit-like regions across the anticlinal wall were observed and both BRK1-YFP and PDLP1-GFP were detected in the pits.

Since it has been confirmed that the cell wall around PD is enriched with methyl-esterified pectins, combined with our results, it's conceivable that BRK1, just like FH2, may colocalize with plasmodesmata in the pit field (Diao et al., 2018). Different from FH2, which caps and attaches F-actin at PDs, BRK1 activates Arp2/3 to produce branched actin, it's tempting that both BRK1 and FH2 are among the same pathway—BRK1 in pit field activates Arp2/3 to generate F-actin, which are stabilized and attached on the PDs by FH2. The mechanism of BRK1 localizing at PD is still an open question, however, I may get some clues from previous reports about the SCAR system localizing at the ER surface (Zhang et al., 2013b). As we know, during cytokinesis, remnants of ER get traversing it, thus it is possible that the distribution of BKR1 at PD associates with the SCAR localization at ER.

The presence of F-actin at PD has been reported for decades, and the related mechanism remain controversial due to the difficulty of F-actin observation inside the cell wall and manipulating F-actin dynamics at PD. Now I found that BRK1 also localized at PDs, and I assume that the related mutant will open a window for F-actin dynamic manipulation.

4.4 Materials and methods

4.4.1 Plant materials and growth conditions.

Arabidopsis thaliana ecotype Columbia 0 (Col-0) was used as wild type in this study. The transgenic line *PDLP1:: PDLP1-GFP* (Thomas et al., 2008) was obtained from the Y. Wei lab (University of Saskatchewan). The transgenic line *LTPG:: YFP–LTPG* was described previously

(DeBono et al., 2009; Ambrose et al., 2013) and was introduced into the *brk1* mutant through the crossing.

Seeds were sterilized with 70% ethanol, rinsed five times with sterilized water and plated onto Petri dishes containing ½ MS media, 1.0 % agar, 1 % sucrose and pH is 5.7. Plates were wrapped with parafilm (Bemis Inc.) and transferred to a 21 °C growth cabinet (with continuous light) and placed in the rack vertically. Young root, hypocotyl and cotyledon were imaged at 3–4 days after germination, and true leaf cells were imaged at 4–5 days after germination.

4.4.2 Tissue preparation and microscopy.

All observations were performed on living cells. For true leaf imaging, cotyledons were cut off at the base with fine scissors and the rest of seedlings were mounted. All the tissue samples were mounted in Nunc chambers (Lab-Tek) with 10 ul Perfluoroperhydrophenanthrene (PP11) and covered by 2~3-mm-thick 0.7% Phytagel. All CLSM images were obtained via point-scan confocal microscopy: Zeiss Meta 510 with Zeiss Axiovert 200M microscope, 63X water immersion and Zeiss 880 with Airyscan, both 40X and 63X water immersion. GFP fluorescence was detected with an excitation wavelength of 488nm from an argon laser and captured with emission wavelength of 495 – 550nm. YFP was detected with an excitation wavelength of 514nm from an argon laser and captured with emission wavelength of 495 – 550nm. FM4-64 was detected with an excitation wavelength of 514nm from an argon laser and captured with emission wavelength of 570 – 645nm. PI was detected with an excitation wavelength of 514nm from an argon laser and captured with emission wavelength of 570 – 640nm. The Z-stack interval varies from 0.2 µm to 0.4 µm. For sampling, more than 5 cotyledons or first pair of true leaves were picked and more than 10 cells for each sample were imaged.

4.4.3 Image analysis.

Images were processed with Image J software (http://rsb.info.nih.gov/ij/). The ClearVolume plugin (https://imagej.net/ClearVolume) (Royer et al., 2015) from Image J and Fluorender (http://www.sci.utah.edu/software/fluorender.html) (Wan et al., 2009) were used for 3D renderings. Figures were assembled using Corel Draw software (www.Corel.com; Corel System. Ottawa, ON, Canada), and Inkscape vector graphics software (www.inkscape.org). Statistical analysis was performed using Microsoft Excel (Microsoft, Edmond, WA).

4.4.4 BFA treatment.

8-day-old seedlings of both wild type and the brk-1 mutant grew on ½ MS media, media with 1 % sucrose, 1.0 % agar and pH is 5.7. Seedlings were incubated with either 50 μM BFA (Sigma-Aldrich) in 50 μM FM4-64 (Sigma-Aldrich) or with 50 μM FM4-64 only as a control (Dettmer et al., 2006). After 5 minutes, the seedlings were mounted into Nunc chambers and the BFA bodies in the true leaves were imaged via confocal microscopy.

4.4.5 PI and FM4-64 staining.

To label the plasma membrane, FM4-64 (Sigma-Aldrich) was used. Five-day-old seedlings were incubated with 10μM FM4-64 in 1.5ml Eppendorf tube and then centrifuged at 3381g for 1min. After centrifugation, keep incubating for 20mins at room temperature. Stained samples were rinsed gently with distilled water, mounted with PP11, and imaged in chambers as above.

To label the cell wall, Propidium Iodide (PI) (Invitrogen) was used. Four or five-day-old seedlings were incubated with 100μg/ml PI in 1.5ml Eppendorf tube and then centrifuged at 3381g for 1min. After centrifugation, keep incubating for 20 mins at room temperature. Stained samples were rinse gently with distilled water, mounted with PP11, and imaged in chambers as above.

Chapter 5 Conclusions and Future Perspectives

Cell wall geometry includes features such as cell wall faces, corners and edges, and can be sensed and partially modulated by intracellular modules. Among the geometry features, cell edges have been shown to be enriched in CLASP, GCP2/3 and RAB-GTPase (Ambrose and Wasteneys, 2011a; Ambrose et al., 2011a; Kirchhelle et al., 2016). To further our understanding of the mechanisms of cell edge regulation, I conducted a screen of additional cell edge proteins, identified five, and performed a detailed characterization of one of them —BRK1.

In this project, I examined the function of BRK1 by focusing on its localization pattern formation and its regulation on cell geometry. The analysis revealed a relationship between BRK1 and cell edge geometry.

The characterization of BRK1 started from the investigation of BRK1 protein localization and the mechanism behind it. Preferentially, BRK1 localized to the anticlinal and periclinal edges exhibiting high curvatures in different cell types such as pavement, mesophyll and hypocotyl cells. BRK1 at both edges exhibited slow dynamics and low turnover and motility. This particular pattern gradually formed after cytokinesis and is correlates with cell wall maturity. The pattern formation suggests that BRK1 may be able to sense the cell edge curvature, which then orchestrates its localization.

The localization mechanism of BRK1 and the whole SCAR system it belongs has been investigated extensively. During trichome development, SCAR system (including BRK1) is recruited by a guanine nucleotide exchange factor– SPIKE1 to the trichome apex. Here, BRK1 stabilizes SCAR at the plasma membrane, and BRK1's localization, in turn, is SCAR-dependent (Dyachok et al., 2008; Le et al., 2006). SCAR localizing at the trichome apex is further dependent on MTs (Yanagisawa et al., 2018). Our results did not support such a pattern because depolymerization of either actin or MTs did not affect BRK1 localization pattern at edges, at least on the time scale of hours. This inconsistency may also be due to trichomes operating by a different mechanism than pavement cells, or that the treatment used here were insufficient to cause obvious changes in BRK1-YFP localization. An experiment tested with different concentration of MTs depolymerization drug would clarify that.

Still, given my result that MTs and BRK1 are alternatively localized, it would be interesting to see if MTs are involved in BRK1 localization in pavement cells and how BRK1 localization links to cell edge geometrical change.

The *brk-1* mutant has weakened three-way junction and bulgier outer periclinal walls (Dyachok et al., 2008; Frank et al., 2003). In the context of my data, bulging cells have rounded periclinal cell edges (i.e. having reduced curvature). The reduced periclinal curvature may be due to partial loss of cell adhesion at the cell edges, as with the case with three-way junction, or it may result from loss of local strengthening of cell edge wall. Considering the function of BRK1 in actin organization along with my observation of aberrant vesicle trafficking in the *brk-1* mutant, it is conceivable that the defects in secretion of cell wall compounds may be the cause of the weaker cell adhesion and loss of edge sharpness.

In addition to the cell junction region, MTs on both periclinal and anticlinal wall in the *brk-1* mutant also exhibited global changes, including both abnormal periclinal MTs pattern and AMB number. The mechanism behind those CMTs structure changes haven't been elucidated yet. However, considering the similarities between AMBs and PPB, it's possible that actin could also bridge and narrow down the anticlinal MTs into AMBs, which is similar to its function during PPB formation. And due to fewer AMBs formed, the periclinal MTs, especially the one connected with AMBs, might tend to align, instead of mixing with each other. Therefore, those CMT structure changes resulted in the reduced lobing phenotype in the *brk-1* mutant. Moreover, the geometry changes in *brk-1* mutant, the lobe formation defect, for example, also exert certain influence on AMBs structure. As the lobe formed, both side of lobe undergoes curvature change: the edge curvature at the convex side reduces and therefore the anticlinal MTs get permission to bypass the edges and from AMBs while at the concave side the AMBs formation is rare because the edge still remains sharp. In the *brk-1* mutant, the failure of lobe formation further prevents the AMBs formation because both sides keep their sharp edge due to the loss of lobe formation. Since lobe formation is long process and numerous factors get involved, the mechanism of symmetry growth breaking and the exact role of cytoskeleton during lobe formation remain unclear. Still, the abnormal CMT structure is, at least partly, responsible for the lobe defect in the *brk-1* mutant pavement cells. Also, given that BRK1 promotes actin nucleation and actin facilitates vesicle

trafficking containing cell wall materials, it's also possible that the cell wall ingredient pattern around the lobe in the *brk-1* mutant pavement cells also changes.

Interestingly, such an interaction scenario between edge curvature and BRK1 also works for characterized edge protein CLASP1, GCP2/3, and Rab A5c. Like BRK1, all these edge proteins accumulate at the incipient cell edge exhibiting higher edge curvature after cytokinesis and the mutation of edge proteins cause reduction of cell edge curvature (Ambrose and Wasteneys, 2011; Ambrose et al., 2011; Kirchhelle et al., 2016). Since these edge proteins obviously work in different pathways and the little overlap was found among those pathways, it would be interesting to further figure out the mechanisms of how edge proteins sense and are delivered to the edge.

Besides, the localization of BRK1 at the anticlinal wall partially overlap with PD, indicating a novel relationship between BRK1 (the Arp2/3 nucleation system) and PD, which have not been described yet. Given a previous report showed that FH2 regulate the size exclusion limit (SEL) through F-actin stabilization (Diao et al., 2018), it's highly possible that BRK1 localizes at the membrane of PD and recruit the Arp2/3 system to nucleate F-actin, which is critical for SEL regulation.

I have still left questions from different aspects:

1) the mechanism of BRK1 association with high curvature edge: how may BRK1 sense the edge curvature, and how it is recruited to the edge. Since the inconsistency between Yanagisawa et al., 2018 and my results could be due to either different mechanism or different dosage response, it would be interesting to see whether and how MTs are involved in BRK1 localizing in pavement cells. Moreover, according to pervious report, SPIKE1 is a peripheral membrane protein and exhibits slightly enrichment at the concave side of lobe (Zhang et al., 2010). Given SPIKE's role in BRK1 localization in trichomes, it will be worth determining if the SPIKE1 pathway works for BRK1 cell edge localization in pavement cells. To test that, a double line expressing both SPIKE1 and BRK1 will be necessary and further 4-D observation will clarify if similar scenario occurs during BRK1 localizing at the edges.

   Experimental manipulation of cell edge curvature could be used to assess the interaction between BRK1 localization and cell edge curvature. For example, cell edge curvature could

be artificially increased during imaging by pressing the cover slip down onto rounded cell to create flattening and associated sharp boundaries of the flattened areas. By measuring the fluorescence intensity change of BRK1-YFP at these new high-curvature regions, we could figure out if the BRK1 pattern changes as the edge curvature changes. Based on my timelapse and FRAP data, this flattening experiment may require hours to induce any changes in BRK1-YFP localization.

2) the mechanism of F-actin influencing MT for lobe initiation. How to periclinal and anticlinal MTs orchestrate to trigger and carry on the lobe initiation and formation and what is the role of F-actin during those process. Previous reports have already shown that blocking F-actin could stop the PPB narrowing (Mineyuki and Palevitz, 1990; Li et al., 2006). Given the AMBs and PPBs share lots of similarities, and given that actin could bridge CMTs to form the PPB (Takeuchi et al., 2016), it is possible that F-actin functions during lobe formation in a similar way as PPB formation. To test that, a double line labeling both MT and F-actin is necessary and 4-D observation with super resolution will clarify if F-actin could bridge CMTs to form the AMBs.
3) Connection between BRK1, actin and PD: based on our results, it is possible that both BRK1 (and the Arp2/3 system) and formins nucleate and stabilize F-actin at the PD. It would be intriguing to see first if the *brk-1* mutants have any PD abnormalities. I have crossed a PD marker line into the *brk-1* mutant to check this. Further test of PD size exclusion limit (SEL) in the *brk-1* mutant will confirm the function of BRK1 on PD regulation. Besides, ultrastructure analysis of PD through TEM also could provide valuable information and clarify the function of BRK1 on PD regulation.
4) the function of BRK1 on cytoplasmic organization and streaming. Due to the limited time, I did not check the cytoplasmic strand phenotype in the *brk-1* mutant with other organelle markers, such as those which label ER, Golgi or tonoplst. By crossing those marker lines into the *brk-1* mutant and checking dynamics of those markers, I could get a big picture of cytoplasm in *brk-1* mutant.

References

Al-Bassam, J., Kim, H., Brouhard, G., van Oijen, A., Harrison, S.C., and Chang, F. (2010). CLASP promotes microtubule rescue by recruiting tubulin dimers to the microtubule. Dev Cell *19*, 245–258.

Allard, J.F., Wasteneys, G.O., and Cytrynbaum, E.N. (2010). Mechanisms of self-organization of cortical microtubules in plants revealed by computational simulations. Mol Bio Cell *21*, 278–286.

Ambrose, C., and Wasteneys, G.O. (2011). Cell edges accumulate gamma tubulin complex components and nucleate microtubules following cytokinesis in Arabidopsis thaliana cells. PLoS ONE *6*, e27423.

Ambrose, C., and Wasteneys, G.O. (2014). Microtubule initiation from the nuclear surface controls cortical microtubule growth polarity and orientation in Arabidopsis thaliana. Plant Cell Physiol *55*, 1636–1645.

Ambrose, J.C., and Wasteneys, G.O. (2008). CLASP modulates microtubule-cortex interaction during self-organization of acentrosomal microtubules. Molecular Biology of the Cell *19*, 4730–4737.

Ambrose, C., Allard, J.F., Cytrynbaum, E.N., and Wasteneys, G.O. (2011). A CLASP-modulated cell edge barrier mechanism drives cell-wide cortical microtubule organization in Arabidopsis. Nat Commun *2*, 430.

Ambrose, C., DeBono, A., and Wasteneys, G. (2013). Cell geometry guides the dynamic targeting of apoplastic GPI-linked lipid transfer protein to cell wall elements and cell borders in Arabidopsis thaliana. PLoS ONE *8*, e81215.

Angelini, J., Vosolsobe, S., Skupa, P., and Marc, J. (2018). Phospholipase Dδ assists to cortical microtubule recovery after salt stress. Protoplasma *255*, 1195–1204.

Armour, W.J., Barton, D.A., Law, A.M., and Overall, R.L. (2015). Differential growth in periclinal and anticlinal walls during lobe formation in Arabidopsis cotyledon pavement cells. Plant Cell *27*, 2484–2500.

Baskin, T.I. (2001). On the alignment of cellulose microfibrils by cortical microtubules: a review and a model. Protoplasma *215*, 150–171.

Baskin, T.I. (2005). Anisotropic expansion of the plant cell wall. Annu Rev Cell Dev Biol *21*, 203–222.

Basu, D., El-Assal, S.D., Le, J., and Szymanski, D.B. (2004). Interchangeable functions of Arabidopsis PIROGI and the human WAVE complex subunit SRA1 during leaf epidermal development. Development *131*, 4345–4355.

Basu, D., Le, J., El-Essal, S.E.-D., Huang, S., Zhang, C., Mallery, E.L., Koliantz, G., Staiger, C.J., and Szymanski, D.B. (2005). DISTORTED3/SCAR2 is a putative arabidopsis WAVE

complex subunit that activates the Arp2/3 complex and is required for epidermal morphogenesis. The Plant Cell *17*, 502–524.

Baulin, V.A., Marques, C.M., and Thalmann, F. (2007). Collision induced spatial organization of microtubules. Biophysical Chemistry *128*, 231–244.

Belteton, S.A., Sawchuk, M.G., Donohoe, B.S., Scarpella, E., and Szymanski, D.B. (2018). Reassessing the roles of PIN proteins and anticlinal microtubules during pavement cell morphogenesis. Plant Physiol *176*, 432–449.

Besson, S., and Dumais, J. (2011). Universal rule for the symmetric division of plant cells. Proc Natl Acad Sci U S A *108*, 6294–9299.

Binarova, P., Cenklova, V., Prochazkova, J., Doskocilova, A., Volc, J., Vrlik, M., and Bogre, L. (2006). Gamma-tubulin is essential for acentrosomal microtubule nucleation and coordination of late mitotic events in Arabidopsis. Plant Cell *18*, 1199–1212.

Bloch, D., Pleskot, R., Pejchar, P., Potocky, M., Yalovsky, S., and Zarsky, V. (2016). Exocyst SEC3 and phosphoinositides define sites of exocytosis in pollen tube initiation and growth. Plant Physiol *172*, 980–1002.

Bompard, G., and Caron, E. (2004). Regulation of WASP/WAVE proteins: making a long story short. J Cell Biol *166*, 957–962.

Boudaoud, A., and Burian, A. (2014). FibrilTool, an ImageJ plug-in to quantify fibrillar structures in raw microscopy images. Nat Protoc *9*, 457–463.

Bratman, S.V., and Chang, F. (2007). Stabilization of overlapping microtubules by fission yeast CLASP. Dev Cell *13*, 812–827.

Braybrook, S., and Jonsson, H. (2016). Shifting foundations: the mechanical cell wall and development. Curr Opin Plant Biol *29*, 115–120.

Braybrook, S., and Peaucelle, A. (2013). Mechano-chemical aspect of organ formation in Arabidopsis thaliana: the relationship between auxin and pectin. PLoS ONE *8*, E57813.

Brown, R.C., and Lemmon, B.E. (2007). The pleiomorphic plant MTOC: An evolutionary perspective. J Integ Plant Biol *49*, 1142–1153.

Buchanan, B.B., Gruissem, W., and Jones, R.L. (2005). Biochemistry & molecular biology of plants. (Rockville: American Society of Plant Physiologists).

Burk, D.H., and Ye, Z.H. (2002). Alteration of oriented deposition of cellulose microfibrils by mutation of a katanin-like microtubule-severing protein. Plant Cell *14*, 2145–2160.

Burk, D.H., Liu, B., Zhong, R., Morrison, W.H., and Ye, Z.H. (2001). A katanin-like protein regulates normal cell wall biosynthesis and cell elongation. Plant Cell *13*, 807–827.

Burnette, D.T., Sengupta, P., Dai, Y., Lippincott-Schwartz, J., and Kachar, B. (2011). Bleaching/blinking assisted localization microscopy for superresolution imaging using standard fluorescent molecules. Proc Natl Acad Sci U S A *108*, 21081–21086.

Buschmann, H., Fabri, C.O., Hauptmann, M., Hutzler, P., Laux, T., Lloyd, C.W., and Schaffner, A.R. (2004). Helical growth of the Arabidopsis mutant tortifolia1 reveals a plant-specific microtubule-associated protein. Curr Biol *14*, 1515–1521.

Buschmann, H., Chan, J., Sanchez-Pulido, L., Andrade-Navarro, M.A., Doonan, J.H., and Lloyd, C.W. (2006). Microtubule-associated AIR9 recognizes the cortical division site at preprophase and cell-plate insertion. Curr Biol *16*, 1938–1943.

Caffall, K.H., and Mohnen, D. (2009). The structure, function, and biosynthesis of plant cell wall pectic polysaccharides. Carbohydr Res *344*, 1879–1900.

Caillaud, M.C., Lecomte, P., Jammes, F., Quentin, M., Pagnotta, S., Andrio, E., de Almeida, E.J., Marfaing, N., Abad, P., Gounon, P., et al. (2008). MAP65-3 Microtubule-Associated Protein is essential for nematode-induced giant cell ontogenesis in Arabidopsis. Plant Cell *20*, 423–437.

Casero, P.J., and Knox, J.P. (1995). The monoclonal antibody JIM5 indicates patterns of pectin deposition in relation to pit fields at the plasma-membrane-face of tomato pericarp cell walls. Protoplasma *188*, 133–137.

Castellano, M.M., and Sablowski, R. (2008). Phosducin-Like Protein 3 is required for microtubule-dependent steps of cell division but not for meristem growth in Arabidopsis. Plant Cell *20*, 969–981.

Chakrabortty, B., Blilou, I., Scheres, B., and Mulder, B.M. (2018). A computational framework for cortical microtubule dynamics in realistically shaped plant cells. PLoS Comput Biol *14*, 1–26.

Chan, J., Sambade, A., Calder, G., and Lloyd, C. (2009). Arabidopsis cortical microtubules are initiated along, as well as branching from, existing microtubules. Plant Cell *21*, 2298–2306.

Chan, J., Eder, M., Crowell, E.F., Hampson, J., Calder, G., and Lloyd, C. (2011). Microtubules and CESA tracks at the inner epidermal wall align independently of those on the outer wall of light-grown Arabidopsis hypocotyls. J Cell Sci *124*, 1088–1094.

Chen, Z., Borek, D., Padrick, S.B., Gomez, T.S., Metlagel, Z., Ismail, A.M., Umetani, J., Billadeau, D.D., Otwinowski, Z., and Rosen, M.K. (2010). Structure and control of the actin regulatory WAVE complex. Nature *468*.

Cheng, X., Lang, I., Adeniji, O.S., and Griffing, L. (2017). Plasmolysis-deplasmolysis causes changes in endoplasmic reticulum form, movement, flow, and cytoskeletal association. J Exp Bot *68*, 4075–4087.

Chi, Z., and Ambrose, C. (2016). Microtubule encounter-based catastrophe in Arabidopsis cortical microtubule arrays. BMC Plant Biol *16*, 18.

Clayton, L., Black, C.M., and Lloyd, C.W. (1985). Microtubule nucleating sites in higher plant cells identified by an auto-antibody against pericentriolar material. J Cell Biol *101*, 319–324.

Cleary, A.L. (1995). F-Actin Redistributions at the Division Site in Living Tradescantia Stomatal Complexes as Revealed by Microinjection of Rhodamine-Phalloidin. Protoplasma *185*, 152–165.

Cleary, A.L., Gunning, B.E.S., Wasteneys, G.O., and Hepler, P.K. (1992). Microtubule and F-Actin Dynamics at the Division Site in Living Tradescantia Stamen Hair-Cells. Journal of Cell Science *103*, 977–988.

Collings, D.A. (2008). Crossed wires: Interactions and cross-talk between the microtubule and microfilament networks in plants. In Plant Cell Monographs: Plant Microtubules, Development, and Flexibility., pp. 47–82.

Collings, D.A., and Wasteneys, G.O. (2005). Actin microfilament and microtubule distribution patterns in the expanding root of Arabidopsis thaliana. Can J Bot *83*, 579–590.

Cosgrove, D.J. (2005). Growth of the plant cell wall. Nat Rev Mol Cell Biol *6*, 850–861.

Crowell, E.F., Bischoff, V., Desprez, T., Rolland, A., Stierhof, Y.-D., Schumacher, K., Gonneau, M., Hofte, H., and Vernhettes, S. (2009). Pausing of golgi bodies on microtubules regulates secretion of cellulose synthase complexes in Arabidopsis. Plant Cell *21*, 1141–1154.

Daher, F.B., and Braybrook, S. (2015). How to let go: pectin and plant cell adhesion. Front Plant Sci *6*, 1–8.

DeBolt, S., Gutierrez, R., Ehrhardt, D.W., Melo, C.V., Ross, L., Cutler, S.R., Somerville, C., and Bonetta, D. (2007). Morlin, an inhibitor of cortical microtubule dynamics and cellulose synthase movement. Proc Natl Acad Sci U S A *104*, 5854–5859.

DeBono, A., Yeats, T.H., Rose, J.K.C., Bird, D., Jetter, R., Kunst, L., and Samuels, L. (2009). Arabidopsis LTPG Is a Glycosylphosphatidylinositol-Anchored Lipid Transfer Protein Required for Export of Lipids to the Plant Surface. THE PLANT CELL ONLINE *21*, 1230–1238.

Deeks, M.J., Hussey, P.J., and Davies, B. (2002). Formins: intermediates in signaltransduction cascades that affect cytoskeletal reorganization. Trends Plant Sci *7*, 492–498.

Deeks, M.J., Kaloriti, D., Davies, B., and Hussey, P.J. (2004). Arabidopsis NAP1 is essential for Arp2/3-dependent trichome morphogenesis. Curr Biol *14*, 1410–1414.

Deinum, E.E., and Mulder, B.M. (2013). Modelling the role of microtubules in plant cell morphology. Cell Biology *16*, 688–692.

Deinum, E.E., Tindemans, S.H., and Mulder, B.M. (2011). Taking directions: the role of microtubule-bound nucleation in the self-organization of the plant cortical array. Phys Biol *8*, 056002.

Demidov, D., Van Damme, D., Geelen, D., Blattner, F.R., and Houben, A. (2005). Identification and dynamics of two classes of Aurora-like kinases in Arabidopsis and other plants. Plant Cell *17*, 836–848.

Desai, A., and Mitchison, T.J. (1997). Microtubule polymerization dynamics. Annu Rev Cell Dev Biol *13*, 83–117.

Dettmer, J., Hong-Hermesdorf, A., Stierhof, Y.D., and Schumacher, K. (2006). Vacuolar H+-ATPase Activity Is Required for Endocytic and Secretory Trafficking in Arabidopsis. Plant Cell *18*, 715–730.

Dhonukshe, P., and Gadella, T.W.J. (2003). Alteration of microtubule dynamic instability during preprophase band formation revealed by yellow fluorescent protein-CLIP170 microtubule plus-end labeling. Plant Cell *15*, 597–611.

Diao, M., Ren, S., Wang, Q., and Huang, S. (2018). Arabidopsis formin 2 regulates cell-to-cell trafficking by capping and stabilizing actin filaments at plasmodesmata. ELife *7*, e36316.

Dixit, R., and Cyr, R. (2004a). The cortical microtubule array: From dynamics to organization. Plant Cell *16*, 2546–2552.

Dixit, R., and Cyr, R. (2004b). Encounters between dynamic cortical microtubules promote ordering of the cortical array through angle-dependent modifications of microtubule behavior. Plant Cell *16*, 3274–3284.

Djakovic, S., Smith, L., Dyachok, J., Burke, M., and Frank, M. (2006). BRICK1/HSPC300 functions with SCAR and the ARP2/3 complex to regulate epidermal cell shape in Arabidopsis.

Dogterom, M., and Yurke, B. (1997). Measurement of the Force-Velocity Relation for Growing Microtubules. Science *278*, 856–860.

Dong, Y., Liu, N., Liu, G., Li, W., Yan, A., and Wang, D.M. (2011). Actin and myosin co-localize in plasmodesmata and ectodesmata-like structure. Agri Sci China *10*, 845–849.

Dyachok, J., Shao, M.R., Vaughn, K., Bowling, A., Facette, M., Djakovic, S., Clark, L., and Smith, L. (2008). Plasma membrane-associated SCAR complex subunits promote cortical F-actin accumulation and normal growth characteristics in Arabidopsis roots. Mol Plant *1*, 990–1006.

Dyachok, J., Sparks, J.A., Liao, F., Wang, Y.-S., and Blancaflor, E.B. (2014). Fluorescent protein-based reporters of the actin cytoskeleton in living plant cells: fluorophore variant, actin binding domain, and promoter considerations. Cytoskeleton (Hoboken, N.J.) *71*, 311–327.

Ehrhardt, D.W., and Shaw, S.L. (2006). Microtubule dynamics and organization in the plant cortical array. Annu Rev Plant Biol *57*, 859–875.

Eng, R.C., and Wasteneys, G.O. (2014). The microtubule plus-end tracking protein ARMADILLO-REPEAT KINESIN1 promotes microtubule catastrophe in Arabidopsis. Plant Cell *26*, 3372–3386.

Eren, E.C., Dixit, R., and Gautam, N. (2010). A three-dimensional computer simulation model reveals the mechanisms for self-organization of plant cortical microtubules into oblique arrays. Mol Biol Cell *21*, 2674–2684.

Eren, E.C., Gautam, N., and Dixit, R. (2012). Computer simulation and mathematical models of the noncentrosomal plant cortical microtubule cytoskeleton. Cytoskeleton (Hoboken, N.J.) *69*, 144–154.

Erhardt, M., Stoppin-Mellet, V., Campagne, S., Canaday, J., Mutterer, J., Fabian, T., Sauter, M., Muller, T., Peter, C., Lambert, A.M., et al. (2002). The plant Spc98p homologue colocalizes with gamma-tubulin at microtubule nucleation sites and is required for microtubule nucleation. Journal of Cell Science *115*, 2423–2431.

Errera, L. (1886). Sur une condition fondamentale d'equilibre des cellules vivantes. C R Hebd Seances Acad Sci *103*, 822–824.

Escobar, B., Carecer, G., Fernandez-Miranda, G., Cascon, A., Bravo-Cordero, J., Montoya, M., Robledo, M., Canamero, M., and Malumbres, M. (2010). Brick1 is an essential regulator of actin cytoskeleton required for embryonic development and cell transformation. Cancer Res *70*, 9349–9359.

Facette, M., Park, Y., Sutimantanapi, D., Luo, A., Cartwright, H., Yang, B., Bennett, E.J., Sylvester, A.W., and Smith, L.G. (2015). The SCAR/WAVE complex polarizes PAN receptors and promotes division asymmetry in maize. Nat Plants *1*.

Facette, M., Rasmussen, C.G., and Van Norman, J.M. (2018). A plane choice: coordinating timing and orientation of cell division during plant development. Curr Opin Plant Biol *47*, 47–55.

Faulkner, C., Akman, O., Bell, K., Jeffree, C., and Oparka, K. (2008). Peeking into pit fields: a multiple twinning model of secondary plasmodesmata formation in tobacco. Plant Cell *20*, 1504–1518.

Faulkner, C.R., Blackman, L.M., Collings, D.A., Cordwell, S.J., and Overall, R.L. (2009). Anti-tropomyosin antibodies co-localise with actin microfilaments and label plasmodesmata. Eur J Cell Biol *88*, 357–369.

Fernandez-Calvino, L., Faulkner, C., Walshaw, J., Saalbach, G., Bayer, E., and Benitez-Alfonso, Y. (2011). Arabidopsis plasmodesmal proteome. PloS ONE *6*, e18880.

Fitzgibbon, J., Beck, M., Zhou, J., Faulkner, C., Robatzek, S., and Oparka, K. (2013). A developmental framework for complex plasmodesmata formation revealed by large-scale imaging of the Arabidopsis leaf epidermis. Plant Cell *25*, 57–70.

Flanders, D.J., Rawlins, D.J., Shaw, P.J., and Lloyd, C.W. (1990). Nucleus-associated microtubules help determine the division plane of plant epidermal cells: avoidance of four-way junctions and the role of cell geometry. J Cell Biol *110*, 1111–1122.

Frank, M.J., and Smith, L.G. (2002). A small, novel protein highly conserved in plants and animals promotes the polarized growth and division of Maize leaf epidermal cells. Curr Biol *12*, 849–853.

Frank, M., Cartwright, H.N., and Smith, L.G. (2003). Three Brick genes have distinct functions in a common pathway promoting polarized cell division and cell morphogenesis in the maize leaf epidermis. Development *130*, 753–762.

Fu, Y., Li, H., and Yang, Z. (2002). The ROP2 GTPase controls the formation of cortical fine F-actin and the early phase of directional cell expansion during Arabidopsis organogenesis. Plant Cell *14*, 777–794.

Fu, Y., Gu, Y., Zheng, Z.L., Wasteneys, G., and Yang, Z.B. (2005). Arabidopsis interdigitating cell growth requires two antagonistic pathways with opposing action on cell morphogenesis. Cell *120*, 687–700.

Fujita, M., and Wasteneys, G.O. (2014). A survey of cellulose microfibril patterns in dividing, expanding, and differentiating cells of Arabidopsis thaliana. Protoplasma *251*, 687–698.

Galva, C., Kirik, V., Lindeboom, J.J., Kaloriti, D., Rancour, D., Hussey, P., and Sedbrook, J.C. (2014). The microtubule plus-end tracking proteins SPR1 and EB1b interact to maintain polar cell elongation and directional organ growth in Arabidopsis. Plant Cell *26*, 4409–4425.

Gardiner, J.C., Taylor, N.G., and Turner, S.R. (2003). Control of cellulose synthase complex localization in developing xylem. Plant Cell *15*, 1740–1748.

Gautreau, A., Ho, H.H., Li, J., and Kirschner, M.W. (2004). Purification and architecture of the ubiquitous Wave complex. Proc Natl Acad Sci U S A *101*, 4379–4383.

Geisler, D.A., Sampathkumar, A., Mutwil, M., and Persson, S. (2008). Laying down the bricks: logistic aspects of cell wall biosynthesis. Curr Opin Plant Biol *11*, 647–652.

Goodbody, K.C., Venverloo, C.J., and Lloyd, C.W. (1991). Laser microsurgery demonstrates that cytoplasmic strands anchoring the nucleus across the vacuole of premitotic plant-cells are under tension - implications for division plane alignment. Development *113*, 931–939.

Green, P.B. (1962). Mechanism for Plant Cellular Morphogenesis. Science *138*, 1404–1405.

Guerriero, G., Hausman, J.-F., and Cai, G. (2014). No Stress! Relax! Mechanisms Governing Growth and Shape in Plant Cells. Int J Mol Sci *15*, 5094–5114.

Gundersen, G.G., Gomes, E.R., and Wen, Y. (2004). Cortical control of microtubule stability and polarization. Curr Opin Cell Biol *16*, 106–112.

Gutierrez, R., Lindeboom, J.J., Paredez, A.R., Emons, A.M.C., and Ehrhardt, D.W. (2009). Arabidopsis cortical microtubules position cellulose synthase delivery to the plasma membrane and interact with cellulose synthase trafficking compartments. Nat Cell Biol *11*, 797–806.

Hamant, O., Heisler, M.G., Jonsson, H., Krupinski, P., Uyttewaal, M., Bokov, P., Corson, F., Sahlin, P., Boudaoud, A., Meyerowitz, E.M., et al. (2008). Developmental Patterning by Mechanical Signals in Arabidopsis. Science *322*, 1650–1655.

Hannak, E., and Heald, R. (2006). Xorbit/CLASP links dynamic microtubules to chromosomes in the Xenopus meiotic spindle. J Cell Biol *172*, 19–25.

Hashimoto, T., and Kato, T. (2006). Cortical control of plant microtubules. Current Opinion in Plant Biology *9*, 5–11.

Hawkins, R.J., Tindemans, S.H., and Mulder, B.M. (2010). Model for the orientational ordering of the plant microtubule cortical array. Phys Rev E Stat Nonlin Soft Matter Phys *82*, 11911.

Hejnowicz, Z., Rusin, A., and Rusin, T. (2000). Tensile Tissue Stress Affects the Orientation of Cortical Microtubules in the Epidermis of Sunflower Hypocotyl. Journal of Plant Growth Regulation *19*, 31–44.

Hepler, P.K., Vidali, L., and Cheung, A. (2001). Polarized cell growth in higher plants. Annu Rev Cell Dev Biol *17*, 159–187.

Hepworth, C., Caine, R.S., Harrison, E.L., Sloan, J., and Gray, J.E. (2018). Stomatal development: focusing on the grasses. Current Opinion in Plant Biology *41*, 1–7.

Herrmann, A., Livanos, P., Lipka, E., and Muller, S. (2018). Dual localized kinesin-12 POK2 plays multiple roles during cell division and interacts with MAP65-3. EMBO Rep *19*, e46085.

Higaki, T., Kutsuna, N., Okubo, E., Sano, T., and Hasezawa, S. (2006). Actin Microfilaments Regulate Vacuolar Structures and Dynamics: Dual Observation of Actin Microfilaments and Vacuolar Membrane in Living Tobacco BY-2 Cells. Plant Cell Physiol *47*, 839–852.

Himmelspach, R., Williamson, R.E., and Wasteneys, G.O. (2003). Cellulose microfibril alignment recovers from DCB-induced disruption despite microtubule disorganization. Plant J *36*, 565–575.

Ho, C.M.K., Hotta, T., Guo, F., Roberson, R.W., Lee, Y.R., and Liu, B. (2011). Interaction of antiparallel microtubules in the phragmoplast is mediated by the microtubule-associated protein MAP65-3 in Arabidopsis. Plant Cell *23*, 2909–2923.

Hofmeister, W. (1863). Zusatze und berichtigungen zu den 1851 veröffentlichen untersuchungen der entwicklung höherer kryptogamen. Jahrbucher Fur Wissenschaft Und Botanik *3*, 259–293.

Hussey, P.J., Hawkins, T.J., Igarashi, H., Kaloriti, D., and Smertenko, A. (2002). The plant cytoskeleton: recent advances in the study of the plant microtubule-associated proteins MAP-65, MAP-190 and the Xenopus MAP215-like protein, MOR1. Plant Mol Biol *50*, 915–924.

Innocenti, M., Zucconi, A., Disanza, A., and Scita, G. (2004). Abi1 is essential for the formation and activation of a WAVE2 signalling complex. Nat Cell Biol *6*, 319–327.

Inoue, Y.H., do Carmo Avides, M., Shiraki, M., Deak, P., Yamaguchi, M., Nishimoto, Y., Matsukage, A., and Glover, D.M. (2000). Orbit, a novel microtubule-associated protein essential for mitosis in Drosophila melanogaster. J Cell Biol *149*, 153–166.

Ismail, A.M., Padric, S.B., Chen, B., and Rosen, M.K. (2009). The WAVE regulatory complex is inhibited. Nat Struct Mol Biol *16*, 561–563.

Janson, M.E., and Dogterom, M. (2004). Scaling of microtubule force-velocity curves obtained at different tubulin concentrations. Phys Rev Lett *92*, 2723–2736.

Janson, M.E., de Dood, M.E., and Dogterom, M. (2003). Dynamic instability of microtubules is regulated by force. Journal of Cell Biology *161*, 1029–1034.

Jelinkova, A., Malinska, K., Simon, S., Kleine-Vehn, J., Parezova, M., Pejchar, P., Kubes, M., Martinec, J., Friml, J., Zazimalova, E., et al. (2010). Probing plant membranes with FM dyes: tracking, dragging or blocking? Plant J *61*, 883–892.

Job, D., Valiron, O., and Oakley, B. (2003). Microtubule nucleation. Curr Opin Cell Biol *15*, 111–117.

Karahara, I., Suda, J., Tahara, H., and Mineyuki, Y. (2009). The preprophase band is a localized center of clathrin-mediated endocytosis in late prophase cells of the onion cotyledon epidermis. Plant Journal *57*, 819–831.

Kawamura, E., and Wasteneys, G.O. (2008). MOR1, the Arabidopsis thaliana homologue of Xenopus MAP215, promotes rapid growth and shrinkage, and suppresses the pausing of microtubules in vivo. J Cell Sci *121*, 4114–4123.

Keerthissinghe, S., Nadeau, J.A., Lucas, J.R., and Sack, F.D. (2015). The Arabidopsis leucine-rich repeat receptor-like kinase MUSTACHES enforces stomatal bilateral symmetry inArabidopsis. Plant J *81*, 684–694.

Ketelaar, T., Faivre-Moskalenko, C., Esseling, J.J., de Ruijter, N.C.A., Grierson, C.S., Dogterom, M., and Emons, A.M.C. (2002). Positioning of nuclei in Arabidopsis root hairs: an actin-regulated process of tip growth. The Plant Cell *14*, 2941–2955.

Kirchhelle, C., Chow, C.M., Foucart, C., Neto, H., Stierhof, Y.D., Kalde, M., Walton, C., Fricker, M., Smith, R.S., Jerusalem, A., et al. (2016). The specification of geometric edges by a plant Rab GTPase is an essential cell-patterning principle during organogenesis in Arabidopsis. Dev Cell *36*, 386–400.

Knox, J.P., and Benitez-Alfonso, Y. (2014). Roles and regulation of plant cell walls surrounding plasmodesmata. Curr Opin Plant Biol *22*, 93–100.

Komaki, S., Abe, T., Coutuer, S., Inze, D., Russinova, E., and Hashimoto, T. (2010). Nuclear-localized subtype of end-binding 1 protein regulates spindle organization in Arabidopsis. J Cell Sci *123*, 451–459.

Komarova, Y.A., Vorobjev, I.A., and Borisy, G.G. (2002). Life cycle of MTs: persistent growth in the cell interior, asymmetric transition frequencies and effects of the cell boundary. J. Cell. Sci. *115*, 3527–3539.

Komis, G., Mistrik, M., Samajova, O., Doskocilova, A., Ovecka, M., Illes, P., Bartek, J., and Samaj, J. (2014). Dynamics and Organization of Cortical Microtubules as Revealed by Superresolution Structured Illumination Microscopy. Plant Physiology *165*, 129–148.

Konopka, C.A., Backues, S.K., and Bednarek, S.Y. (2008). Dynamics of Arabidopsis Dynamin-Related Protein 1C and a Clathrin Light Chain at the Plasma Membrane. The Plant Cell *20*, 1363–1380.

Kroeger, J.H., Zerzour, R., and Geitmann, A. (2011). Regulator or Driving Force? The Role of Turgor Pressure in Oscillatory Plant Cell Growth. PLoS ONE *6*, e18549.

Kumagai, F., Nagata, T., Yahara, N., Moriyama, Y., Horio, T., Naoi, K., Hashimoto, T., Murata, T., and Hasezawa, S. (2003). Gamma-tubulin distribution during cortical microtubule reorganization at the M/G1 interface in tobacco BY-2 cells. European Journal of Cell Biology *82*, 43–51.

Kumar, M., Campbell, L., and Turner, S. (2016). Secondary cell wall: biosynthesis and manipulation. J Exp Bot *67*, 515–531.

Kutschera, U. (2008). The growing outer epidermal wall: design and physiological role of a composite structure. Ann Bot *101*, 615–621.

Laan, L., Husson, J., Munteanu, E.L., Kerssemakers, J.W.J., and Dogterom, M. (2008). Force-generation and dynamic instability of microtubule bundles. Proc Natl Acad Sci U S A *105*, 8920–8925.

Lansbergen, G., Grigoriev, I., Mimori-Kiyosue, Y., Ohtsuka, T., Higa, S., Kitajima, I., Demmers, J., Galjart, N., Houtsmuller, A.B., Grosveld, F., et al. (2006). CLASPs attach microtubule plus ends to the cell cortex through a complex with LL5beta. Dev Cell *11*, 21–32.

Le, J., El-Assal, S.D., Basu, D., Saad, M.E., and Szymanski, D.B. (2003). Requirements for Arabidopsis ATARP2 and ATARP3 during epidermal development. Curr Biol *13*, 1341–1347.

Le, J., Mallery, E.L., Zhang, C., Brankle, S., and Szymanski, D.B. (2006). Arabidopsis BRICK1/HSPC300 is an essential WAVE-complex subunit that selectively stabilizes the Arp2/3 Activator SCAR2. Curr Biol *16*, 895–901.

Ledbetter, M.C., and Porter, K.R. (1963). A “Microtubule” in Plant Cell Fine Structure. J Cell Biol *19*, 239–250.

Lemos, C.L., Sampaio, P., Maiato, H., Costa, M., Omel’yanchuk, L.V., Liberal, V., and Sunkel, C.E. (2000). Mast, a conserved microtubule-associated protein required for bipolar mitotic spindle organization. EMBO J *19*, 3668–3682.

Lerouxel, O., Cavalier, D.M., Liepman, A.H., and Keegstra, K. (2006). Biosynthesis of plant cell wall polysaccharides - a complex process. Current Opinion in Plant Biology *9*, 621–630.

Li, C., Chen, Z., and Yuan, M. (2006). Actomyosin is Involved in the Organization of the Microtubule Preprophase Band in Arabidopsis Suspension Cultured Cells. J Integrative Plant Biol *48*, 53–61.

Li, L., Ren, F., Gao, X., Wei, P., and Wang, X. (2013). The reorganization of actin filaments is required for vacuolar fusion of guard cells during stomatal opening in Arabidopsis. Plant Cell and Environment *36*, 484–497.

Li, S., Lei, L., Somerville, C.R., and Gu, Y. (2012). Cellulose synthase interactive protein 1 (CSI1) links microtubules and cellulose synthase complexes. Proceedings of the National Academy of Sciences *109*, 185–190.

Li, Y., Shen, Y., Cai, C., Zhong, C., Zhu, L., and Ren, H. (2010). The type II Arabidopsis formin14 interacts with microtubules and microfilaments to regulate cell division. Plant Cell *22*, 2710–2726.

Lin, D., Cao, L., Zhou, Z., and Fu, Y. (2013). Rho GTPase signaling activates microtubule severing to promote microtubule ordering in arabidopsis. Curr Biol *23*, 290–297.

Lindeboom, J.J., Nakamura, M., Hibbel, A., Shundyak, K., Gutierrez, R., Ketelaar, T., Emons, A.M.C., Mulder, B.M., Kirik, V., and Ehrhardt, D.W. (2013). A mechanism for reorientation of cortical microtubule arrays driven by microtubule severing. Science (New York, N.Y.) *342*, 1245533.

Liners, E., Letesson, J.J., Didembourg, C., and Van Cutsem, P. (1989). Monoclonal antibodies against pectin: recognition of a conformation induced by calcium. Plant Physiol *91*, 1419–1424.

Linkner, J., Witte, G., Stradal, T., and Faix, J. (2011). High-Resolution X-Ray Structure of the Trimeric Scar/WAVE-Complex Precursor Brk1. PLoS One *6*, e21327.

Lipka, E., Gadeyne, A., Stockle, D., and Muller, S. (2014). The Phragmoplast-Orienting Kinesin-12 class proteins translate the positional information of the preprophase band to establish the cortical division zone in Arabidopsis thaliana. Plant Cell *26*, 2617–2632.

Littlejohn, G.R., Mansfield, J.C., Christmas, J.T., Witterick, E., Fricker, M.D., Grant, M.R., Smirnoff, N., Everson, R.M., Moger, J., and Love, J. (2014). An update: improvements in imaging perfluorocarbon-mounted plant leaves with implications for studies of plant pathology, physiology, development and cell biology. Front Plant Sci *5*, 1–8.

Liu, B., and Palevitz, B.A. (1992). Organization of cortical microfilaments in dividing root-cells. Cell Motil Cytoskeleton *23*, 252–264.

Liu, B., Marc, J., Joshi, H.C., and Palevitz, B.A. (1993). A gamma-tubulin-related protein associated with the microtubule arrays of higher plants in a cell cycle-dependent manner. J Cell Sci *104 (Pt 4)*, 1217–1228.

Liu, B., Joshi, H.C., Wilson, T.J., Silflow, C.D., Palevitz, B.A., and Snustad, D.P. (1994). gamma-Tubulin in Arabidopsis: gene sequence, immunoblot, and immunofluorescence studies. Plant Cell *6*, 303–314.

Lloyd, C.W. (1991). How does the cytoskeleton read the laws of geometry in aligning the division plane of plant cells? Development *113*, 55–65.

Lloyd, C.W., and Traas, J. (1988). The role of F-actin in determining the division plane of carrot suspension cells. Drug studies. Development *102*, 211–221.

Lofke, C., Dunser, K., Scheuring, D., and Kleine-Vehn, J. (2015). Auxin regulates SNARE-dependent vacuolar morphology restricting cell size. ELife *4*, 1–16.

Maiato, H., Fairley, E.A., Rieder, C.L., Swedlow, J.R., Sunkel, C.E., and Earnshaw, W.C. (2003). Human CLASP1 is an outer kinetochore component that regulates spindle microtubule dynamics. Cell *113*, 891–904.

Majda, M., Grones, P., Sintorn, I.M., and Mellerowicz, E.J. (2017). Mechanochemical polarization of contiguous cell walls shapes plant pavement cells. Dev Cell *43*, 290–304.

Marc, J. (1997). Microtubule-organizing centres in plants. Trends Plant Sci *2*, 223–230.

Martinez, P., Allsman, L.A., Brakke, K.A., and Rasmussen, C.G. (2018). Predicting division planes of three-dimensional cells by soap-film minimization. Plant Cell DOI: https://doi.org/10.1105/tpc.18.00401.

Masoud, K., Herzog, E., Chaboute, M.E., and Schmit, A.C. (2013). Microtubule nucleation and establishment of the mitotic spindle in vascular plant cells. Plant Journal *75*, 245–257.

Mathur, J., Mathur, N., Kirik, V., Kernebeck, B., Srinivas, B.P., and Hulskamp, M. (2003a). Arabidopsis CROOKED encodes for the smallest subunit of the ARP2/3 complex and controls cell shape by region specific fine F-actin formation. Development *130*, 3137–3146.

Mathur, J., Mathur, N., Kernebeck, B., and Hulskamp, M. (2003b). Mutations in actin-related proteins 2 and 3 affect cell shape development in Arabidopsis. Plant Cell *15*, 1632–1645.

Mathur, J., Mathur, N., Kernebeck, B., Srinivas, B.P., and Hulskamp, M. (2003c). A novel localization pattern for an EB1-like protein links microtubule dynamics to endomembrane organization. Curr Biol *13*, 1991–1997.

McNeil, M., Darvill, A., Fry, S.C., and Albersheim, P. (1984). Structure and function of the primary cell walls of plants. Ann Rev Biochem *53*, 625–663.

Micheli, F. (2001). Pectin methylesterases: cell wall enzymes with important roles in plant physiology. Trends Plant Sci *6*, 414–419.

Mimori-Kiyosue, Y., Grigoriev, I., Lansbergen, G., Sasaki, H., Matsui, C., Severin, F., Galjart, N., Grosveld, F., Vorobjev, I., Tsukita, S., et al. (2005). CLASP1 and CLASP2 bind to EB1 and regulate microtubule plus-end dynamics at the cell cortex. Journal of Cell Biology *168*, 141–153.

Mineyuki, Y., and Palevitz, B.A. (1990). Relationship between preprophase band organization, F-Actin and the division site in Allium - Fluorescence and morphometric studies on cytochalasin-treated cells. Journal of Cell Science *97*, 283–295.

Mitchison, T., and Kirschner, M. (1984). Dynamic instability of microtubule growth. Nature *312*, 237–242.

Molchan, T.M., Valster, A.H., and Hepler, P.K. (2002). Actomyosin promotes cell plate alignment and late lateral expansion in Tradescantia stamen hair cells. Planta *214*, 683–693.

Morgan, J.L., Strumillo, J., and Zimmer, J. (2013). Crystallographic snapshot of cellulose synthesis and membrane translocation. Nature *493*, 181–186.

Morvan, O., Quentin, M., Jaunear, A., Mareck, A., and Morvan, C. (1998). Immunogold localization of pectin methylesterases in the cortical tissues of flax hypocotyl. Protoplasma *202*, 175–184.

Mueller, S.C., and Brown, R.M. (1982). The control of cellulose microfibril deposition in the cell wall of higher plants. Planta *154*, 489–500.

Muller, S., Smertenko, A., Wagner, V., Heinrich, M., Hussey, P.J., and Hauser, M.T. (2004). The plant microtubule-associated protein AtMAP65-3/PLE is essential for cytokinetic phragmoplast function. Curr Biol *14*, 412–417.

Muller, S., Han, S., and Smith, L.G. (2006). Two kinesins are involved in the spatial control of cytokinesis in Arabidopsis thaliana. Curr Biol *16*, 888–894.

Murata, T., Sonobe, S., Baskin, T.I., Hyodo, S., Hasezawa, S., Nagata, T., Horio, T., and Hasebe, M. (2005). Microtubule-dependent microtubule nucleation based on recruitment of gamma-tubulin in higher plants. Nat Cell Biol *7*, 961–968.

Nakajima, K., Furutani, I., Tachimoto, H., Matsubara, H., and Hashimoto, T. (2004). SPIRAL1 encodes a plant-specific microtubule-localized protein required for directional control of rapidly expanding Arabidopsis cells. Plant Cell *16*, 1178–1190.

Nakamura, M., and Hashimoto, T. (2009). A mutation in the Arabidopsis -tubulin-containing complex causes helical growth and abnormal microtubule branching. Journal of Cell Science *122*, 2208–2217.

Nakamura, M., Naoi, K., Shoji, T., and Hashimoto, T. (2004). Low concentrations of propyzamide and oryzalin alter microtubule dynamics in Arabidopsis epidermal cells. Plant Cell Physiol *45*, 1330–1334.

Nakaoka, Y., Kimura, A., Tani, T., and Goshima, G. (2015). Cytoplasmic nucleation and atypical branching nucleation generate endoplasmic microtubules in Physcomitrella patens. Plant Cell *1*, 228–242.

Oda, Y., and Fukuda, H. (2013). Rho of plant GTPase signaling regulates the behavior of Arabidopsis kinesin-13A to establish secondary cell wall patterns. Plant Cell *25*, 4439–4450.

Oda, Y., Iida, Y., Nagashima, Y., Sugiyama, Y., and Fukuda, H. (2015). Novel coiled-coil proteins regulate exocyst association with cortical microtubules in Xylem cells via the conserved oligomeric Golgi-complex protein. Plant Cell Physiol *56*, 277–286.

Orfila, C., and Knox, J.P. (2000). Spatial regulation of pectic polysaccharides in relation to pit fields in cell walls of tomato fruit pericarp. Plant Physiol *122*, 775–781.

Palin, R., and Geitmann, A. (2012). The role of pectin in plant morphogenesis. Biosystems *109*, 397–402.

Panteris, E., and Galatis, B. (2005). The morphogenesis of lobed plant cells in the mesophyll and epidermis: organization and distinct roles of cortical microtubules and actin filaments. New Phytol *167*, 721–732.

Panteris, E., Apostolakos, P., and Galatis, B. (1993). Microtubule organization and cell morphogenesis in 2 semi-lobed cell-types of Adiantum-Capillus-Veneris L leaflets. New Phytol *125*, 509–520.

Panteris, E., Apostolakos, P., and Galatis, B. (2006). Cytoskeletal asymmetry in Zea mays subsidiary cell mother cells: a monopolar prophase microtubule half-spindle anchors the nucleus to its polar position. Cell Motil Cytoskeleton *63*, 696–709.

Panteris, E., Adamakis, I.D., Daras, G., and Rigas, S. (2015). Cortical microtubule patterning in roots of Arabidopsis thaliana primary cell wall mutants reveals the bidirectional interplay with cell expansion. Plant Signal Behav *10*, e1028701.

Paredez, A.R., Somerville, C.R., and Ehrhardt, D.W. (2006). Visualization of cellulose synthase demonstrates functional association with microtubules. Science *312*, 1491–1495.

Pastuglia, M., Azimzadeh, J., Goussot, M., Camilleri, C., Belcram, K., Evrard, J.L., Schmit, A.C., Guerche, P., and Bouchez, D. (2006). Gamma-tubulin is essential for microtubule organization and development in Arabidopsis. Plant Cell *18*, 1412–1425.

Peaucelle, A., Wightman, R., and Hofte, H. (2015). The Control of Growth Symmetry Breaking in the Arabidopsis Hypocotyl. Curr Biol *25*, 1746–1752.

Pelloux, J., Rusterucci, C., and Mellerowicz, E.J. (2007). New insights into pectin methyl-esterase structure and function. Trends Plant Sci *12*, 267–277.

Pereira, G., and Schiebel, E. (1997). Centrosome-microtubule nucleation. J Cell Sci *110*, 295–300.

Pickett-Heaps, J.D., and Northcote, D.H. (1966). Organization of microtubules and endoplasmic reticulum during mitosis and cytokinesis in wheat meristems. J Cell Sci *1*, 109–120.

Pollard, T.D., and Beltzner, C.C. (2002). Structure and function of the Arp2/3 complex. Curr Opin Struct Biol *12*, 768–774.

Pollard, T.D., and Borisy, G.G. (2003). Cellular motility driven by assembly and disassembly of actin filaments. Cell *112*, 453–465.

Pollard, T.D., and Cooper, J.A. (2009). Actin, a Central Player in Cell Shape and Movement. Science *326*, 1208–1212.

Quan, L., Xiao, R., Li, W., Oh, S.A., Kong, H., Ambrose, J.C., Malcos, J.L., Cyr, R., Twell, D., and Ma, H. (2008). Functional divergence of the duplicated AtKIN14a and AtKIN14b genes: critical roles in Arabidopsis meiosis and gametophyte development. Plant J *53*, 1013–1026.

Radford, J.E., and White, R.G. (1998). Localization of a myosin-like protein to plasmodesmata. Plant J *14*, 743–750.

Rahni, R., and Birnbaum, K.D. (2016). Plant Cell Shape: Trafficking Gets Edgy. Dev Cell *36*, 353–354.

Rasmussen, C.G., Wright, A.J., and Muller, S. (2013). The role of the cytoskeleton and associated proteins in determination of the plant cell division plane. Plant Journal *75*, 258–269.

Raynaud-Messina, B., and Merdes, A. (2007). γ-tubulin complexes and microtubule organization. Curr Opin Cell Biol *19*, 24–30.

Ridley, B.L., O'Neill, M.A., and Mohnen, D. (2001). Pectins: structure, biosynthesis, and oligogalacturonide-related signaling. Phytochemistry *57*, 929–967.

Romagnoli, S., Cai, G., Faleri, C., and Cresti, M. (2007). Microtubule- and actin filament-dependent motors are distributed on pollen tube mitochondria and contribute differently to their movement. Plant Cell Physiol *48*, 345–361.

Rosero, A., Oulehlova, D., Stillerova, L., and Cvrckova, F. (2016). Arabidopsis FH1 Formin affects cotyledon pavement cell shape by modulating cytoskeleton dynamics. Plant Cell Physiol *57*, 488–504.

Rounds, C.M., Lubeck, E., Hepler, P.K., and Winship, L.J. (2011). Propidium Iodide competes with Ca2+ to label pectin in pollen tubes and Arabidopsis root hairs. Plant Physiol *157*, 175–187.

Sachs, J. (1878). Über die Anordnung der Zellen in jüngsten Pflanzentheilen. Arb Bot Inst *2*, 46–104.

Sampathkumar, A., Lindeboom, J., DeBolt, S., Gutierrez, R., Ehrhardt, D.W., Ketelaar, T., and Persson, S. (2011). Live cell imaging reveals structural associations between the actin and microtubule cytoskeleton in Arabidopsis. Plant Cell *23*, 2302–2313.

Sampathkumar, A., Gutierrez, R., McFarlane, H.E., Bringmann, M., Lindeboom, J., Emons, A.-M., Samuels, L., Ketelaar, T., Ehrhardt, D.W., and Persson, S. (2013). Patterning and lifetime of plasma membrane-localized cellulose synthase is dependent on actin organization in Arabidopsis interphase cells. Plant Physiol *162*, 675–688.

Sampathkumar, A., Krupinski, P., Wightman, R., and Meyerowitz, E.M. (2014a). Subcellular and supracellular mechanical stress prescribes cytoskeleton behavior in Arabidopsis cotyledon pavement cells. ELife *3*, e01967.

Sampathkumar, A., Yan, A., Krupinski, P., and Meyerowitz, E.M. (2014b). Physical forces regulate plant development and morphogenesis. Curr Biol *24*, 475–483.

Sapala, A., Runions, A., and Smith, R.S. (2018). Mechanics, geometry and genetics of epidermal cell shape regulation: different pieces of the same puzzle. Curr Opin Plant Biol *47*, 1–8.

Sasaki, T., Fukuda, H., and Oda, Y. (2017). CORTICAL MICROTUBULE DISORDERING1 Is Required for Secondary Cell Wall Patterning in Xylem Vessels. Plant Cell *29*, 3123–3139.

Schaefer, E., Belcram, K., Uyttewaal, M., and Bouchez, D. (2017). The preprophase band of microtubules controls the robustness of division orientation in plants. Science *356*, 186–189.

Seltzer, V., Janski, N., Canaday, J., Herzog, E., Erhardt, M., Evrard, J.-L., and Schmit, A.-C. (2007). Arabidopsis GCP2 and GCP3 are part of a soluble γ-tubulin complex and have nuclear envelope targeting domains: Targeting of γ-tubulin complex proteins. The Plant Journal *52*, 322–331.

Shaw, S.L., Kamyar, R., and Ehrhardt, D.W. (2003). Sustained microtubule treadmilling in Arabidopsis cortical arrays. Science *300*, 1715–1718.

Shi, X., and Ma, Y. (2010). Understanding phase behavior of plant cell cortex microtubule organization. Proc Natl Acad Sci U S A *107*, 11709–11714.

Small, J.V., and Kaverina, I. (2003). Microtubules meet substrate adhesions to arrange cell polarity. Curr Opin Cell Biol *15*, 40–47.

Smith, L.G., and Oppenheimer, D.G. (2005). Spatial control of cell expansion by the plant cytoskeleton. Annu Rev Cell Dev Biol *21*, 271–295.

Somerville, C., Bauer, S., Brininstool, G., and Youngs, H. (2004). Toward a systems approach to understanding plant cell walls. Science *306*, 2206–2211.

Sotiriou, P., Giannoutsou, E., Panteris, E., Galatis, B., and Apostolakos, B. (2017). Local differentiation of cell wall matrix polysaccharides in sinuous pavement cells : its possible involvement in the flexibility of cell shape. Plant Biology http://dx.doi.org/10.1111/ plb.12681.

Sousa, A., Reis, R., Sampaio, P., and Sunkel, C.E. (2007). The Drosophila CLASP homologue, Mast/Orbit regulates the dynamic behaviour of interphase microtubules by promoting the pause state. Cell Motil Cytoskeleton *64*, 605–620.

Spinner, L., Gadeyne, A., Belcram, K., and Van De Slijke, E. (2013). A protein phosphatase 2A complex spatially controls plant cell division. Nat Commun *4*, 1863.

Steiner, A., Rybak, K., Altmann, M., McFarlane, H.E., and Assaad, F.F. (2016). Cell cycle-regulated PLEIADE/AtMAP65-3 links membrane and microtubule dynamics during plant cytokinesis. Plant Journal *88*, 831–841.

Sterling, J.D., Atmodjo, M.A., Inwood, S.E., and Mohnen, D. (2006). Functional identification of an Arabidopsis pectin biosynthetic homogalacturonan galacturonosyltransferase. Proc Natl Acad Sci U S A *103*, 5236–5241.

Su, S., Liu, Z., Chen, C., Zhang, Y., Wang, X., Zhu, L., Miao, L., Wang, X., and Yuan, M. (2010). Cucumber mosaic virus movement protein severs actin filaments to increase the plasmodesmal size exclusion limit in tobacco. Plant Cell *22*, 1373–1387.

Sugimoto, K., Himmelspach, R., Williamson, R.E., and Wasteneys, G.O. (2003). Mutation or drug-dependent microtubule disruption causes radial swelling without altering parallel cellulose microfibril deposition in Arabidopsis root cells. Plant Cell *15*, 1414–1429.

Szymanski, D.B. (2000). The role of actin during Arabidopsis trichome morphogenesis. In Actin: A Dynamic Framework for Multiple Plant Cell Functions, p.

Szymanski, D.B. (2014). The kinematics and mechanics of leaf expansion: new pieces to the Arabidopsis puzzle. Curr Opin Plant Biol *22*, 141–148.

Szymanski, D.B., and Staiger, C.J. (2018). The actin cytoskeleton: functional arrays for cytoplasmic organization and cell shape control. Plant Physiol *176*, 106–118.

Szymanski, D.B., Jilk, R.A., Pollock, S.M., and Marks, M.D. (1998). Control of GL2 expression in Arabidopsis leaves and trichomes. Development *125*, 1161–1171.

Takeuchi, M., Karahara, I., Kajimura, N., and Mineyuki, Y. (2016). Single microfilaments mediate the early steps of microtubule bundling during preprophase band formation in onion cotyledon epidermal cells. Mol Biol Cell *27*, 1809–1820.

Thomas, C.L., Bayer, E., Ritzenthaler, C., Fernandez-Calvino, L., and Maule, A. (2008). Specific targeting of a Plasmodesmal protein affecting cell-to-cell communication. PLoS Biol *6*, e7.

Tindemans, S.H., Hawkins, R.J., and Mulder, B.M. (2010). Survival of the aligned: ordering of the plant cortical microtubule array. Phys Rev Lett *104*, 58103.

Tischer, C., Brunner, D., and Dogterom, M. (2009). Force- and kinesin-8-dependent effects in the spatial regulation of fission yeast microtubule dynamics. Molecular Systems Biology *5*.

Traas, J., Doonan, J.H., Rawlins, D.J., Shaw, P.J., Watts, J., and Lloyd, C.W. (1987). An actin network is present in the cytoplasm throughout the cell cycle of carrot cells and associates with the dividing nucleus. J Cell Biol *105*, 387–395.

Tsuge, T., Tsukaya, H., and Uchimiya, H. (1996). Two independent and polarized processes of cell elongation regulate leaf blade expansion in Arabidopsis thaliana (L.) Heynh. Development *122*, 1589–1600.

Ueda, K., Matsuyama, T., and Hashimoto, T. (1999). Visualization of microtubules in living cells of transgenicArabidopsis thaliana. Protoplasma *206*, 201–206.

Uyttewaal, M., Burian, A., Alim, K., and Hamant, O. (2012). Mechanical stress acts via katanin to amplify differences in growth rate between adjacent cells in Arabidopsis. Cell *149*, 439–451.

Valster, A.H., and Hepler, P.K. (1997). Caffeine inhibition of cytokinesis: Effect on the phragmoplast cytoskeleton in living Tradescantia stamen hair cells. Protoplasma *196*, 155–166.

Van Damme, D., and Geelen, D. (2008). Demarcation of the cortical division zone in dividing plant cells. Cell Biol Int *32*, 178–187.

Van Damme, D., Bouget, F.Y., Van Poucke, K., Inze, D., and Geelen, D. (2004). Molecular dissection of plant cytokinesis and phragmoplast structure: a survey of GFP-tagged proteins. Plant Journal *40*, 386–398.

Van Damme, D., Coutuer, S., De Rycke, R., Bouget, F.Y., Inze, D., and Geelen, D. (2006). Somatic cytokinesis and pollen maturation in Arabidopsis depend on TPLATE, which has domains similar to coat proteins. Plant Cell *18*, 3502–3518.

Vanstraelen, M., Van Damme, D., De Rycke, R., Mylle, E., Inze, D., and Geelen, D. (2006). Cell cycle-dependent targeting of a kinesin at the plasma membrane demarcates the division site in plant cells. Curr Biol *16*, 308–314.

Vaskebova, L., Samaj, J., and Ovecka, M. (2018). Single-point ACT2 gene mutation in the Arabidopsis root hair mutant der1-3 affects overall actin organization, root growth and plant development. Ann Bot *122*, 889–901.

Vos, J.W., Dogterom, M., and Emons, A.M.C. (2004). Microtubules become more dynamic but not shorter during preprophase band formation: A possible “search-and-capture” mechanism for microtubule translocation. Cell Motil Cytoskeleton *57*, 246–258.

Walker, K.L., Muller, S., Moss, D., Ehrhardt, D.W., and Smith, L.G. (2007). Arabidopsis TANGLED identifies the division plane throughout mitosis and cytokinesis. Curr Biol *17*, 1827–1836.

Wan, Y., Otsuna, H., Chien, C., and Hansen, C. (2009). An interactive visualization tool for multi-channel confocal microscopy data in neurobiology research. IEEE Trans Vis Comput Graph *15*, 1489–1496.

Wang, D.M., Wang, X.C., and Zhang, W.C. (2002). Evidence of ultrastructure and physiology of F-actin as component of plasmodesmata. Acta Bot Sinica *44*, 1278–1285.

Wang, X., Zhu, L., Liu, B., Wang, C., Jin, L., Zhao, Q., and Yuan, M. (2007). Arabidopsis MICROTUBULE-ASSOCIATED PROTEIN18 functions in directional cell growth by destabilizing cortical microtubules. Plant Cell *19*, 877–889.

Wang, X., Zhang, J., Yuan, M., Ehrhardt, D.W., Wang, Z., and Mao, T. (2012). Arabidopsis MICROTUBULE DESTABILIZING PROTEIN40 Is Involved in Brassinosteroid Regulation of Hypocotyl Elongation. The Plant Cell *24*, 4012–4025.

Wasteneys, G.O. (2004). Progress in understanding the role of microtubules in plant cells. Current Opinion in Plant Biology *7*, 651–660.

Wasteneys, G.O., and Ambrose, J.C. (2009). Spatial organization of plant cortical microtubules: close encounters of the 2D kind. Trends Cell Biol *19*, 62–71.

Wasteneys, G.O., and Galway, M.E. (2003). Remodelling the cytoskeleton for growth and form: an overview with some new views. Annu Rev Plant Biol *54*, 691–722.

Wasteneys, G.O., Jablonsky, P.P., and Williamson, R.E. (1989). Assembly of purified brain tubulin at cortical and endoplasmic sites in perfused internodal cells of the alga Nitella tasmanica. Cell Biol Int Rep *13*, 513–528.

Wernicke, W., and Jung, G. (1992). Role of cytoskeleton in cell shaping of developing mesophyll of Wheat (Triticum-Aestivum L). Eur J Cell Biol *57*, 88–94.

White, R.G., Badelt, K., Overall, R.L., and Vesk, M. (1994). Actin associated with plasmodesmata. Protoplasma *180*, 169–184.

Wick, S. (1985). The higher-plant mitotic apparatus - redistribution of microtubules, calmodulin and microtubule initiation material during its establishment. Cytobios *43*, 285–294.

Wiese, C., and Zheng, Y. (2006). Microtubule nucleation: -tubulin and beyond. Journal of Cell Science *119*, 4143–4153.

Wightman, R., and Turner, S.R. (2007). Severing at sites of microtubule crossover contributes to microtubule alignment in cortical arrays. Plant J *52*, 742–751.

Wightman, R., and Turner, S.R. (2008). The roles of the cytoskeleton during cellulose deposition at the secondary cell wall. Plant J *54*, 794–805.

Willats, W.G., McCartney, L., Mackie, W., and Knox, J.P. (2001a). Pectin: cell biology and prospects for functional analysis. Plant Mol Biol *47*, 9–27.

Willats, W.G., Orfila, C., Limberg, G., and Voragen, A.G.J. (2001b). Modulation of the degree and pattern of methyl-esterification of pectic homogalacturonan in plant cell walls: implications for pectin methyl esterase action, matrix properties, and cell adhesion. J Biol Chem *276*, 19404–19413.

Woollard, A.D., and Moore, I. (2008). The functions of Rab GTPases in plant membrane traffic. Current Opinion in Plant Biology *11*, 610–619.

Wright, A.J., and Smith, L.G. (2007). Division Plane Orientation in Plant Cells. In Cell Division Control in Plants, (Springer-Verlag), pp. 33–57.

Xu, X.M., Rodrigo-Peiris, T., Brkljacic, J., He, C.B., Mueller, S.C., Meier, I., and Zhao, Q. (2008). RanGAP1 is a continuous marker of the Arabidopsis cell division plane. Proc Natl Acad Sci U S A *105*, 18637–18642.

Yamazaki, D., Oikawa, T., and Takenawa, T. (2007). Rac-WAVE-mediated actin reorganization is required for organization and maintenance of cell-cell adhesion. J Cell Sci *120*, 86–100.

Yanagisawa, M., Desyatova, A.S., Belteton, S.A., and Szymanski, D.B. (2015). Patterning mechanisms of cytoskeletal and cell wall systems during leaf trichome morphogenesis. Nature Plant *1*, p15014.

Yanagisawa, M., Alonso, J.M., and Szymanski, D.B. (2018). Microtubule-dependent confinement of a cell signaling and actin polymerization control module regulates polarized cell growth. Curr Biol *28*, 2459–2466.

Yao, M., Wakamatsu, Y., Itoh, T.J., Shoji, T., and Hashimoto, T. (2008). Arabidopsis SPIRAL2 promotes uninterrupted microtubule growth by suppressing the pause state of microtubule dynamics. J Cell Sci *121*, 2372–2381.

Zerzour, R., Kroeger, J.H., and Geitmann, A. (2009). Polar growth in pollen tubes is associated with spatially confined dynamic changes in cell mechanical properties. Dev Biol *334*, 437–446.

Zhang, G.F., and Staehelin, L.A. (1992). Functional compartmentation of the Golgi apparatus of plant cells: immunocytochemical analysis of high-pressure frozen- and freeze-substituted sycamore maple suspension culture cells. Plant Physiol *99*, 1070–1083.

Zhang, C., Kotchoni, S.O., Samuels, A.L., and Szymanski, D.B. (2010). SPIKE1 signals originate from and assemble specialized domains of the endoplasmic reticulum. Curr Biol *20*.

Zhang, C., Halsey, L.E., and Szymanski, D.B. (2011). The development and geometry of shape change in Arabidopsis thaliana cotyledon pavement cells. BMC Plant Biol *11*, 27.

Zhang, C., Mallery, E.L., and Szymanski, D.B. (2013a). ARP2/3 localization in Arabidopsis leaf pavement cells: a diversity of intracellular pools and cytoskeletal interactions. Front Plant Sci *4*, 238.

Zhang, C., Mallery, E.L., Reagan, S., Boyko, V.P., Kotchoni, S.O., and Szymanski, D.B. (2013b). The Endoplasmic Reticulum is a reservoir for WAVE/SCAR regulatory complex signaling in the Arabidopsis leaf. Plant Physiol *162*, 689–706.

Zhang, Q., Fishel, E., Bertroche, T., and Dixit, R. (2013c). Microtubule severing at crossover sites by katanin generates ordered cortical microtubule arrays in Arabidopsis. Curr Biol *23*, 2191–2195.

Zhang, Y., Iakovidis, M., and Costa, S. (2016). Control of patterns of symmetric cell division in the epidermal and cortical tissues of the Arabidopsis root. Development *143*, 978–982.

Zhu, C., Ganguly, A., Baskin, T.I., McClosky, D.D., Anderson, C.T., Foster, C., Meunier, K.A., Okamoto, R., Berg, H., and Dixit, R. (2015). The Fragile Fiber1 kinesin contributes to cortical microtubule-mediated trafficking of cell wall components. Plant Physiol *167*, 780–792.

Zimmermann, I., Saedler, R., Mutondo, M., and Hulskamp, M. (2004). The Arabidopsis GNARLED gene encodes the NAP125 homolog and controls several actin-based cell shape changes. Mol Genet Genomics *272*, 290–296.

APPENDIX: MT encounter-based catastrophe in Arabidopsis cortical MT arrays

This chapter is based on data from the following paper:

Chi, Z., and Ambrose, C. (2016). Microtubule encounter-based catastrophe in Arabidopsis cortical microtubule arrays. BMC Plant Biol *16*, 18.

ZC and CA performed experiments. ZC performed data analysis and figure assembly. ZC and CA wrote the manuscript. CA conceived the study. Both authors have read and approved the final version of the manuscript.

Abstract

Background: The cortical MTs (CMTs) that line the plasma membrane of interphase plant cells are extensively studied owing to their importance in forming cell walls, and their usefulness as a model system for the study of MT dynamic instability and acentrosomal MT organization. CMTs influence the orientation and structure of cellulose microfibrils in the cell wall by cooperatively forming arrays of varied patterns from parallel to netted. These CMT patterns are controlled by the combined activities of MT dynamic instability and MT-MT interactions. However, it is an open question as to how CMT patterns may feedback to influence CMT dynamics and interactions.

Results: To address this question, we investigated the effects of CMT array patterning on encounter-based CMT catastrophe, which occurs when one CMT grows into another and is unable to cross over. We hypothesized that the varied CMT angles present in disordered (mixed CMTs) arrays will create more opportunities for MT-MT interactions, and thus increase encounter-based catastrophe rates and distribution. Using live-cell imaging of Arabidopsis cotyledon and leaf epidermal cells, we found that roughly 87% of catastrophes occur via the encounter-based mechanism, with the remainder occurring without encounter (free). When comparing ordered (parallel) and disordered (mixed orientation) CMT arrays, we found that disordered configurations show higher proportions of encounter-based catastrophe relative to free. Similarly, disordered CMT arrays have more catastrophes in general than ordered arrays. Encounter-based catastrophes were associated with frequent and sustained periods of pause prior to depolymerization, and CMTs with tight anchoring to the plasma membrane were more prone to undergo encounter-based catastrophe than weakly-attached ones. This suggests that encounter-based catastrophe has a mechanical basis, wherein MTs form physical barriers to one another. Lastly, we show that the commonly used measure of catastrophe frequencies (F_{cat}) can also be influenced by CMT ordering and plasma membrane anchoring.

Introduction

MTs (MTs) are polymers of α/β-tubulin heterodimers that self-assemble into polar filaments with a fast-growing end, the plus end, and a relatively stable end, the minus end (Desai and Mitchison, 1997). MTs play diverse roles at all stages of the eukaryotic cell cycle; guiding cell division, expansion, and morphogenesis. To accomplish their varied tasks, MTs group together to form

specialized arrays that are continuously remodeled by a process termed dynamic instability, wherein individual MT ends switch stochastically between growth and shrinkage through GTP hydrolysis (Desai and Mitchison, 1997; Shaw et al., 2003). Transitions from growth to shrinkage are termed catastrophe, and the transitions from shrinkage to growth are called rescue (Mitchison and Kirschner, 1984). These parameters are biochemically modulated by MT-associated proteins (MAPs), which perform a variety of functions including stabilizing MTs through promoting polymerization of tubulin (Kawamura and Wasteneys, 2008; Yao et al., 2008) , facilitating MT-MT interactions (e.g. crosslinking)(Hussey et al., 2002; Muller et al., 2004), and destabilizing MTs through increasing depolymerization rate or severing MTs (Burk and Ye, 2002; Kawamura and Wasteneys, 2008).

To orchestrate MT organization on a cellular scale, MT-organizing centers (MTOCs) are important structures that provide biochemical, mechanical, and positional information. By nucleating and tethering MTs, MTOCs create polarized groups of MTs such as spindles and interphase cytoplasmic arrays. MTOCs are varied and ubiquitous throughout eukaryotes and include centrosomes in animal cells, spindle pole bodies in fungi (Gundersen et al., 2004), basal bodies in flagellated cells (Gundersen et al., 2004), the nuclear envelope in plants (Clayton et al., 1985; Wick, 1985; Liu et al., 1993; Erhardt et al., 2002; Kumagai et al., 2003; Brown and Lemmon, 2007; Seltzer et al., 2007; Ambrose and Wasteneys, 2014), and plastid in some algae (Brown and Lemmon, 2007). However, in many cells, MTOCs are absent but MTs still obtain global ordering through self-organization, a process wherein global order emerges in a system from interactions between individual elements (Ehrhardt and Shaw, 2006; Hashimoto and Kato, 2006). This "acentrosomal" MT organization is intensely studied in the interphase cortical array of plants, which consists of MTs that are laterally attached to the plasma membrane and undergo continuous dynamic behaviors. These Cortical MTs (CMTs) arrange in various orientations ranging from random/netted, parallel, and highly bundled. By guiding cellulose synthase complexes, CMT organization influences cell wall microfibril patterning, which in turn guides cell expansion patterns (Dixit and Cyr, 2004a). Since CMTs are restricted to the plane of the plasma membrane and highly dynamic, the probability of interactions between individual CMTs is much higher than MTs that are free to roam in three dimensions. Indeed numerous types of MT-MT interactions have been documented and shown to influence CMT arrangement (Dixit and Cyr, 2004b; Ehrhardt and Shaw, 2006; Wasteneys and Ambrose, 2009). These MT-MT interactions include bundle

formation, collision-induced catastrophe (Dixit and Cyr, 2004b), severing (Wightman and Turner, 2007; Lindeboom et al., 2013), and nucleation of MTs from pre-existing MTs (Wasteneys et al., 1989; Murata et al., 2005; Chan et al., 2009).

With respect to bundle formation and collision-induced catastrophe, when a growing CMT encounters another CMT, the relative angle between the two MTs determines whether the incoming MT will form a bundle with the barrier CMT or undergo catastrophe (Dixit and Cyr, 2004b). Specifically, when the contact angle between a growing plus end and the barrier MT is a small angle (for example, less than 40 degrees), the plus ends reorients and continues growth alongside the barrier MT, forming a bundle. But when the incoming MT contacts the barrier MT more directly (i.e. at a large angle), the MT either depolymerizes (encounter-based catastrophe) or crosses over. From this, Dixit and Cyr developed a model for self-organization of CMTs into parallel arrays, wherein bundling speeds up parallel CMT formation, and encounter-based catastrophe favors elimination of CMTs with orientations not parallel to the predominant CMT orientation (Dixit and Cyr, 2004b). Using quantitative experimental data from CMT dynamics, numerous computer simulations and mathematical models have supported this model, but the relative contributions of bundling and encounter-based catastrophe are less clear (Dixit and Cyr, 2004b; Baulin et al., 2007; Allard et al., 2010; Eren et al., 2010, 2012; Hawkins et al., 2010; Shi and Ma, 2010; Tindemans et al., 2010; Ambrose and Wasteneys, 2011; Deinum et al., 2011).

Whether CMT encounter-based catastrophe results from biochemical and/or mechanical mechanisms (or both) is not known. Several catastrophe-inducing MAPs have been found in plants, including kinesin-13A, MAP18, and ARK1kinesin (Wang et al., 2007; Oda and Fukuda, 2013; Eng and Wasteneys, 2014). However, since CMT catastrophe also occurs without an MT-MT encounter, it is unclear as to whether these MAPs have any specificity/preference for collision-induced catastrophe. In terms of mechanical forces, it is known that catastrophe can occur when a growing MT encounters a physical barrier. Specifically, the continued addition of tubulin subunits to the stalled MT plus end generates a compressive force along the MT axis, which can induce MT bending and catastrophe (Dogterom and Yurke, 1997; Janson et al., 2003; Janson and Dogterom, 2004; Tischer et al., 2009). In addition to MT-MT encounters, polymerization against cell edges can also induce CMT catastrophe (Mimori-Kiyosue et al., 2005; Ambrose et al., 2011).

Given that MT-MT encounter outcomes are angle-dependent, it is possible that the highly variable arrangements of CMTs can influence rates of catastrophes, which may then feedback to CMT arrangements. In this study, we sought to investigate: (1) if CMT arrangement can influence catastrophe rates and spatial distribution; and (2) what the mechanistic underpinnings of encounter-based catastrophe are. To address these questions, we performed detailed quantifications of CMT arrangements, catastrophe types (encounter-based or free-based), spatial distributions, crossovers, and CMT-cortex attachment levels. We provide evidence for a strong contribution of force-induced catastrophe and show that indeed CMT arrangement can influence catastrophe types and frequencies.

Results

Encounter-based catastrophes constitute the dominant source of CMT catastrophe

To visualize CMT dynamics, we performed confocal imaging using cotyledons and leaves of Arabidopsis seedlings constitutively expressing GFP fused to Arabidopsis TUBULIN BETA6 (GFP-TUB6) (Nakamura et al., 2004). All data shown represent the combined data from leaves and cotyledons. The sharp cell edges present in meristematic and unexpanded cells are known to induce catastrophe when MTs grow into them(Ambrose et al., 2011), so in the current study, we used mature epidermal cells in order to remove any potential cell edge effects on catastrophe behavior. The large size and rounded cell edges of these cells allowed sampling of large and relatively flat central areas of the outer cell face that were typically tens of microns away from nearby edges. For characterization of catastrophe types, we classified MT catastrophe into an encounter-based catastrophe (Figure A.1A, C) or free catastrophe (Figure A.1B, D). Notably, we found that 87.6% of catastrophes in leaves and cotyledons were encounter-based, with the remaining 12.4% being not associated with the encounter (Figure A.1E). The quantification of another line expressing 35S: GFP-EB1b showed a similar trend, with 85.3% of catastrophes being encounter-based (Figure A.1E).

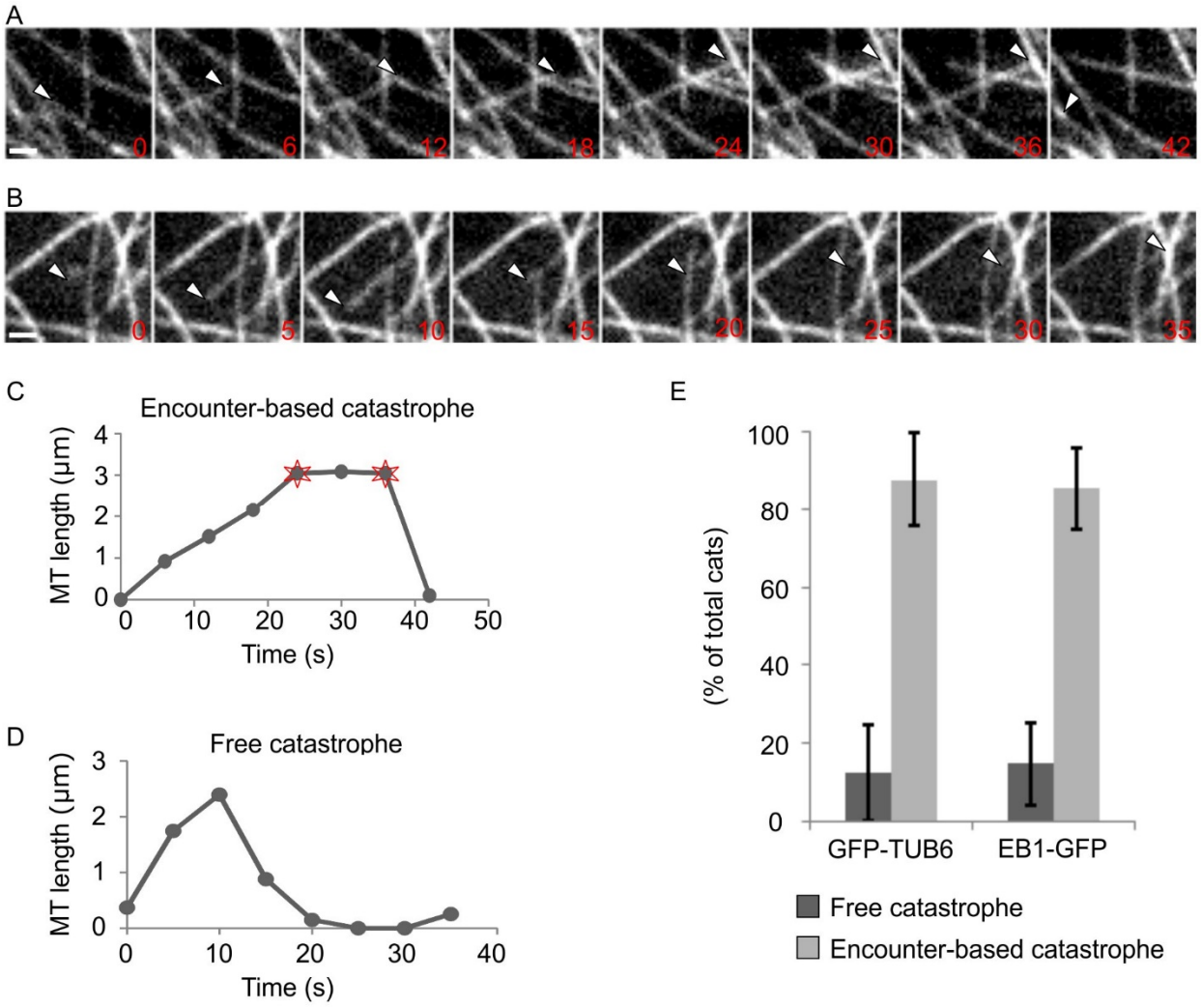

Figure A.1 Two types of catastrophe and their frequencies of occurrence.

(A) Encounter-based catastrophe and (B) free catastrophe. White arrowheads mark CMT plus ends. Numbers indicate time in seconds. (C, D) MT length-changes over time, corresponding to the tracked MTs in A and B, respectively. The stars mark the start and end of a pause. (E) Encounter-based catastrophe is the dominant type of CMT catastrophe. Data were obtained using GFP-TUB6 and EB1-GFP as MT reporters. For GFP-TUB6, n=48 cells, 376 catastrophe events; for GFP-EB1b, n=20 cells, 245 catastrophe events. Bars: A, B = 1 µm.

CMT organization influences the type and spatial distribution of catastrophes

Based on these data, we hypothesized that compared to ordered (parallel) arrays, a highly disordered CMT array will provide more opportunities for CMT collision, and will thus have a larger proportion of encounter-based catastrophes compared to free catastrophes (i.e. a higher ratio of encounter-based to free). To test this, we measured CMT angles within parallel and disordered

arrays (see methods section for CMT angle measurements) and assessed the relative frequency of encounter-based catastrophes (i.e. % encounter-based to total catastrophes). As a measure of array order, we used the standard deviation of CMTs angles. With this method, parallel arrays show smaller standard deviations in CMT angle than net-like arrays. This is illustrated in Figure A.2, which shows an example of a disordered array (SD = 52) (Figure A.2A) and an example of an ordered array (SD = 19) (Figure A2B). To ensure the specificity of our data, SD and catastrophe ratios were measured on a cell-by-cell basis. We sampled 48 cells with varying degrees of order and found a correlation between CMT array disorder and encounter-based catastrophes (Figure A.2C and D). Specifically, the more disordered a CMT array is, the higher the proportion of encounter-based catastrophes is. We observed a similar trend using *35S:: GFP-EB1b* lines (data not shown). These results indicate that CMT arrangement is an important determinant of catastrophe type.

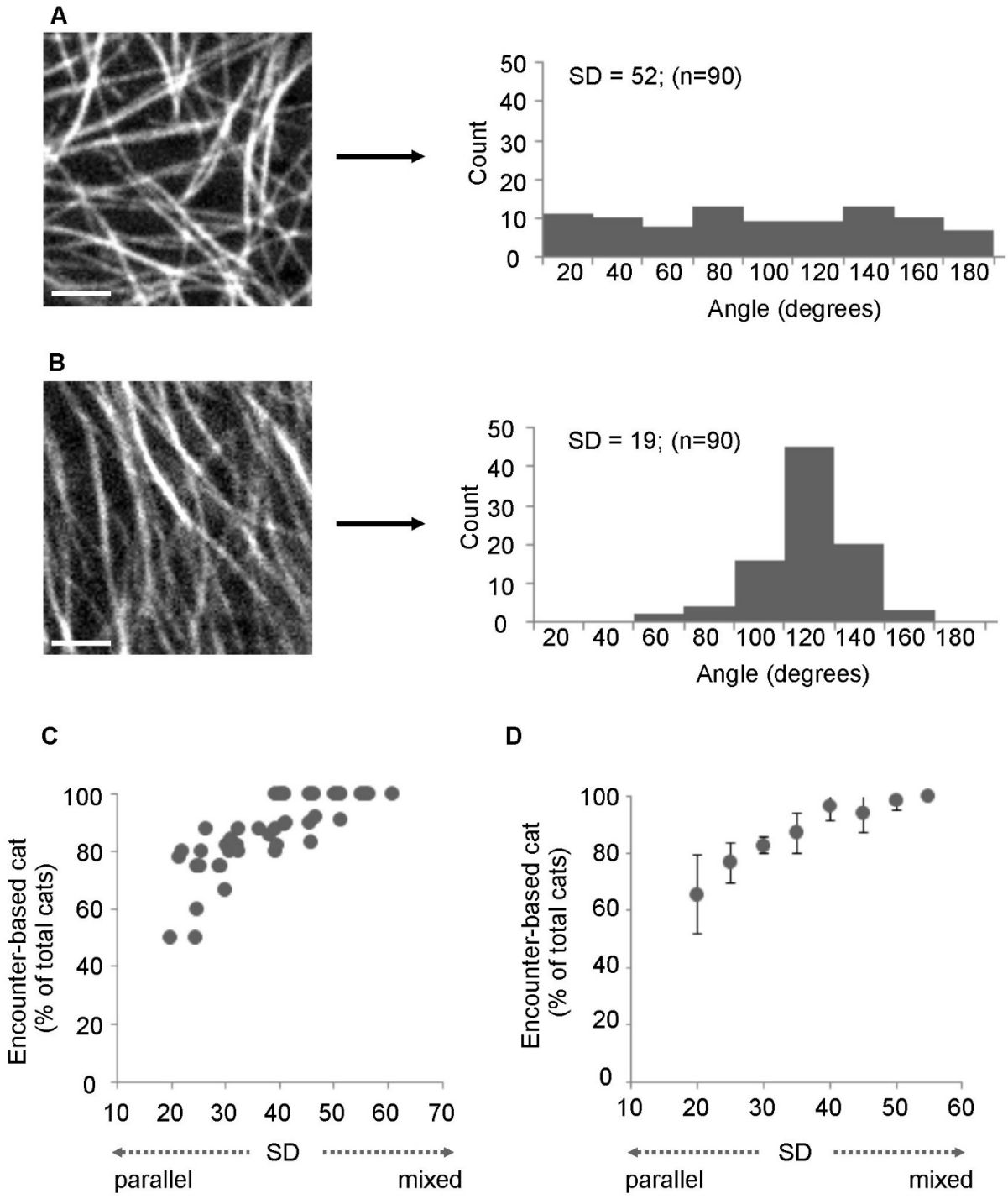

Figure A.2 The ratio of encounter-based to free catastrophe varies with CMT arrangement.

Examples of disordered (A) and highly ordered CMTs (B). Histograms show CMT angle distributions corresponding to the images. (C, D) Disordered CMT arrays have a higher proportion of encounter-based catastrophes relative to free catastrophes. CMT order is expressed as the SD of CMT angles. (C) Un-binned data from individual cells (i.e. each point represents one cell); (D) data from C binned in five SD units. Bars: A, B = 2.5 μm.

Given this organizational influence on catastrophe type, we hypothesized that disordered CMT arrays will also have a higher number of catastrophe events in general (i.e. per unit area and time). We term this property as Density of Catastrophe (D_{cat}) in order to clearly distinguish it from the dynamic instability parameter Catastrophe Frequency (F_{cat}). Proper quantification of D_{cat} presents a number of challenges. For example, simply measuring catastrophes per cellular area is problematic because the MT density itself within a given area would be a major determinant of the density of catastrophe. Similarly, even normalizing for the area occupied by MTs is biased due to the fact that many MTs are very long, bundled, and stable, such that they span the entire region of observation and do not show observable MT end dynamics during the duration of the observation period. Based on these caveats, we chose to normalize density of catastrophe by expressing it as a function of the number of growing plus ends present within the observational region. To obtain simple and accurate counts of growing plus ends, we employed a subtractive technique similar to that used by Burnette et al 2011 (Burnette et al., 2011). By subtracting pixel values between sequential time frames, only areas occupied by new MT growth are shown in the output image (Figure A.3A). Using this method, we indeed found a positive correlation between CMT disordering and density of catastrophe (Figure A.3B). We found a similar trend using GFP-EB1b lines as an indicator of plus end density (MT sidewall labeling was enough to detect the presence or absence of a barrier MT for each catastrophe) (Figure A.3C, D). These data indicate that CMT organization can influence the type and density of catastrophes.

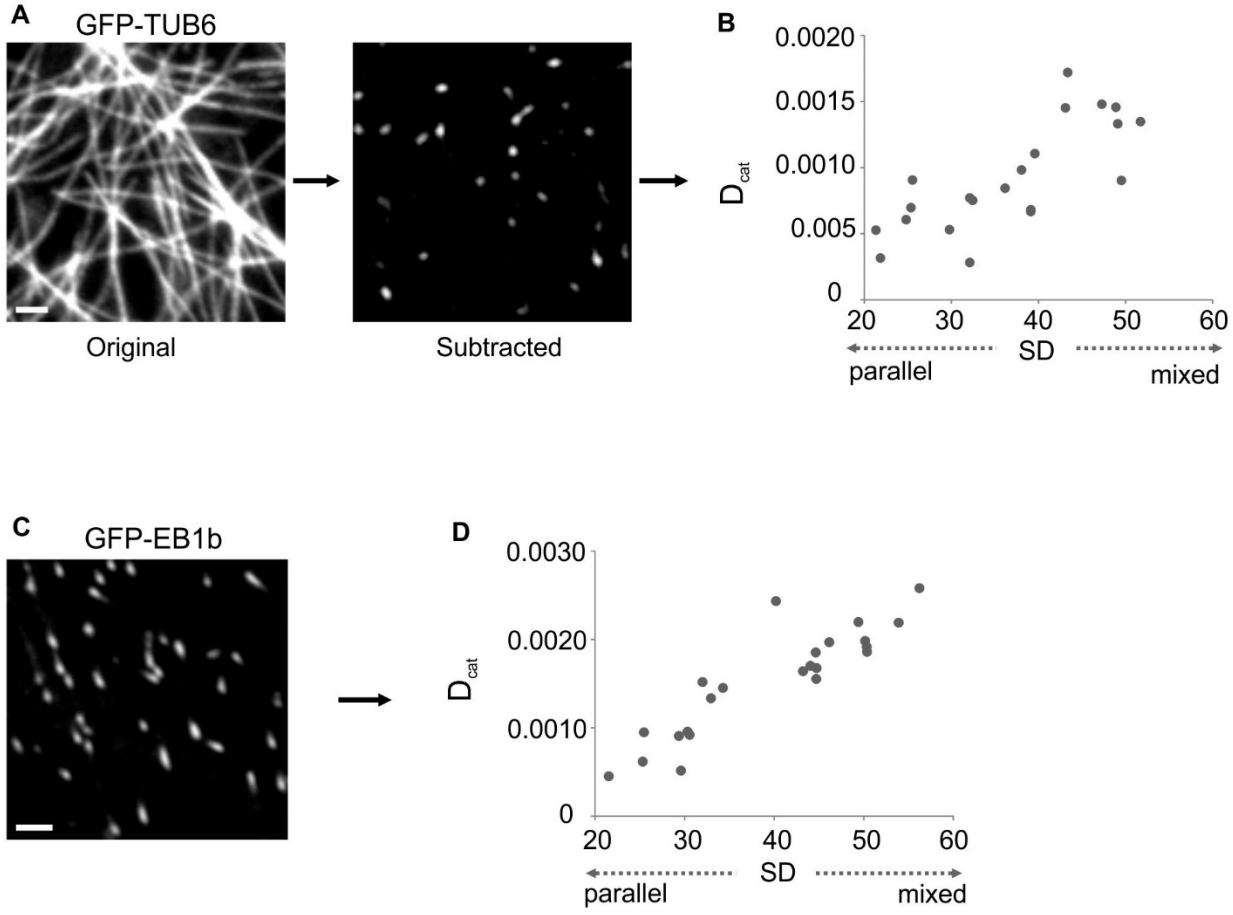

Figure A.3 The density of catastrophe (Dcat) varies with CMT arrangement.

(A) Example of the subtracted image used for measurements to count growing plus ends with GFP-TUB6. (B) The density of catastrophe (Dcat) increases with increasing CMT array disorder (expressed as SD of CMT angles). Measurements derived from GFP-TUB6 subtraction method. (C) Example of the GFP-EB1b image used to count growing plus ends. (D) GFP-EB1b data shows a similar trend to GFP-TUB6 in (B). Bars: A, C = 2 μm.

Strong MT-cortex attachment favors encounter-based catastrophe

We next sought to investigate the mechanism governing encounter-based catastrophe. Given that MT polymerization against a physical barrier is known to induce MT bending and depolymerization (Laan et al., 2008; Ambrose et al., 2011), and that the degree of CMT-cortex attachment influences the outcome of MT-MT interactions by imposing constraints on lateral motions of the MT polymer(Ambrose and Wasteneys, 2008; Baulin et al., 2007), we hypothesized that when a weakly-attached CMT encounters a barrier MT, it will be more prone to lateral motions such as bending and detachment, which act to relieve the axial compression on the incoming MT,

and hence reduce the probability of depolymerization. To test this, we quantified CMT behavior in clasp-1 mutants, which show decreased CMT-cortex attachment (Ambrose and Wasteneys, 2008). To quantify the frequencies of encounter-based catastrophe, we classified encounter events as either cross-over or catastrophe (MT-MT bundling events were excluded). In general, cross-overs were far more numerous than catastrophes in both genotypes, in agreement with previous findings in Arabidopsis (Wightman and Turner, 2007). Figure A.4A shows two examples of MT crossovers, one of which grows in a straight line and eventually undergoes pause and encounter-based catastrophe (red), and another which shows partial detachment and swinging of the growing end as it grows across other MTs (green). This MT appears to be less anchored to the cortex because after it re-attaches, it encounters another MT and stalls, during which time it bends (presumably due to the force of continued polymerization at the stalled plus end). Figure A.4B shows a kymograph of an individual MT growing across several other MTs (which appear as vertical lines in the kymograph).

For quantification of crossover and catastrophes, measurements were normalized using the ratio of encounter-based catastrophe to total encounter events (i.e. catastrophe + cross-over). We found that CMTs in *clasp-1* are more prone to cross over barrier MTs than wild type, and are less likely to undergo catastrophe (Figure A.4C). These data support the idea that strongly-attached MTs are prone to catastrophe because they are restricted to any lateral movement (which would dissipate axial compression), and are unable to detach and cross over the barrier MT.

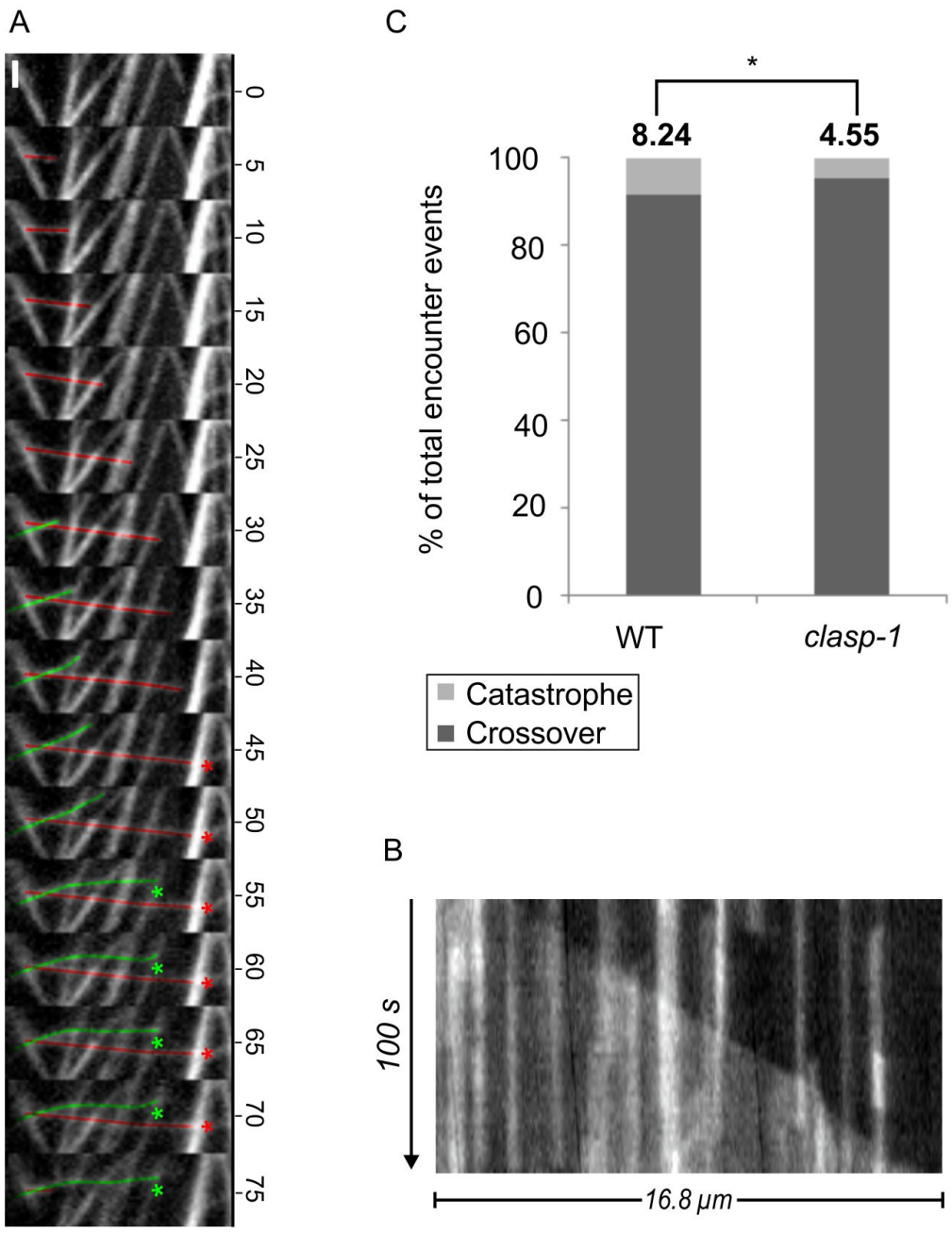

Figure A.4 Encounter-based catastrophe is related to CMT-cortex attachment.

(A). Example of cross-over and encounter-based catastrophe in WT. Redline marks several cross-over events before pause and encounter-based catastrophe. Green line marks a detachment event as described in results. Numbers indicate time in seconds. Both asterisks indicate pause events. Bars: A = 2 µm. (B) Kymographs showing CMT with several cross-over events. (C) Quantification of crossover and encounter-based catastrophe. Asterisk indicates a statistically significant difference of catastrophe frequency between WT and clasp-1 when $P < 0.05$. n=10 cells, 3675 encounter events.

Encounter-based catastrophes exhibit a pause in growth before the catastrophe

During our analysis of catastrophe events, we noticed that the growth of an incoming CMT often pauses upon encounter with a barrier MT and is followed by catastrophe and depolymerization. Figure A.5A shows kymographs of free catastrophes without pause (left panel) and encounter-based catastrophe with pause (right panel). As shown in the histogram in Figure A.5B, the time spent in a pause state for encounter-based catastrophe event varies considerably, with a mean of 19±11 seconds, and a maximum of 80 seconds. For subsequent analysis, we defined pause as a state during which no observable MT growth is detectable for more than 5 seconds. Quantification of pause events revealed that 91.7% of encounter-based catastrophe events were preceded by pause (Figure A.5C). In contrast, only 37.8% of free catastrophes were preceded by pause, and the mean time for pause is 12± 6 seconds (~34% less than for encounter-based pauses) (Figure A.5C). Taken together, these data show that encounter of a growing CMT plus-end with a barrier MT greatly enhances the likelihood and duration of pause prior to depolymerization.

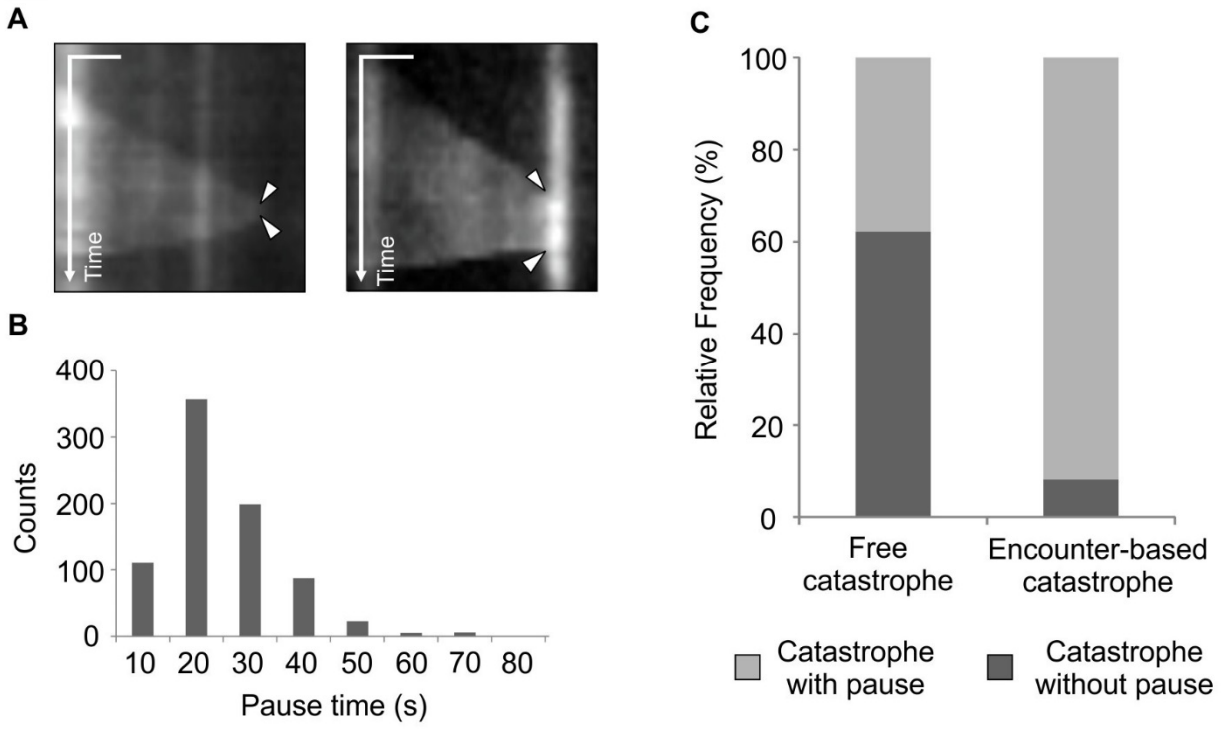

Figure A.5 CMTs with encounter-based catastrophe pause upon encounter with the barrier MT.

(A) Kymographs showing free catastrophe without pause (left panel) and encounter-based catastrophe with pause (right panel). The arrowheads mark the start and the end of the contact. Bars: The kymographs display a period of 76s, scale bar=1 um. (B) Histogram showing the distribution of pausing times for MTs that undergo encounter-based catastrophe. The pausing time ranges from 10 to 80 seconds, and the average time is 19.23 seconds. (C) Encounter-based catastrophes are preceded by pause more frequently than are free catastrophes. n=107 cells, 119 free catastrophe, and 1196 encounter-based catastrophe events.

CMT instability dynamics for catastrophe frequency vary with array organization

Having found that CMT-cortex attachment and CMT organization both have effects on CMT catastrophes, we hypothesized that these factors may lead to inconsistencies in standard measurements of catastrophe frequencies (F_{cat}). To test this, we measured and compared F_{cat} values between disordered and parallel arrays; as well as between weakly-attached and strongly-attached CMT arrays (i.e. clasp-1 vs WT) (Results summarized in Table A.1). F_{cat} was calculated using the total number of catastrophe events divided by the total time spent in growth and pause, and only CMTs that show catastrophe at any point during its observation was used for measurements (Dhonukshe and Gadella, 2003; Dixit and Cyr, 2004b; Vos et al., 2004). Notably, we found that

CMTs showing free-type catastrophes have a significantly higher F_{cat} (0.030±0.009 events/s) compared to those having encounter-based catastrophes (0.021±0.002 events/s) (Table A.1). However, this difference is heavily biased from the longer durations of pause associated with encounter-based catastrophes (i.e. longer pauses increase total measured MT growth times, and thus decreased F_{cat}). Despite these differences, when comparing F_{cat} between disordered CMT arrays (defined as arrays with SDs between 50 and 60) and well-ordered (defined as arrays with SDs between 20 and 30), we found no significant difference in F_{cat} values (disordered = 0.022±0.002 events/s; Ordered = 0.021±0.002 events/s) (Table A.1). This suggests that although free catastrophes do have higher average F_{cat} values than an encounter-based catastrophe, they are not numerous enough to significantly influence overall cellular F_{cat} measurements. However, when assessing the influence of CMT-cortex attachment on F_{cat}, we found that wild-type cells have a significantly higher F_{cat} (0.021±0.001 events/s) than *clasp-1* (0.014±0.001 events/s) (Table A.1). This is consistent with the above observations of WT CMTs being less likely to cross over the barrier MT (Figure A.4C).

Table A.1

Catastrophe frequency varies between different catastrophe types and cell types. Values are means ± s.d. For catastrophe frequencies, n= 12 cells and 191 catastrophe events; for Fcat in both WT and clasp, n=10 cells and 234 catastrophe events.

CMT catastrophe frequencies (events/s)	
General catastrophe Fcat	0.022±0.002
Free catastrophe Fcat	0.030±0.009
Encounter-based catastrophe Fcat	0.021±0.002
Less organized CMT catastrophe Fcat	0.021±0.003
Well organized CMT catastrophe Fcat	0.022±0.002
General catastrophe in WT Fcat	0.021±0.001
General catastrophe in clasp Fcat	0.014±0.001

Discussion

Since the first characterization of plant CMT dynamic instability (Shaw et al., 2003), several studies have made dynamic measurements using a variety of cell types, mutants, and drug treatments to investigate the mechanisms of CMT organization (Dhonukshe and Gadella, 2003; Mathur et al., 2003c; Dixit and Cyr, 2004a; Nakamura et al., 2004; Van Damme et al., 2004; Vos et al., 2004; DeBolt et al., 2007; Kawamura and Wasteneys, 2008; Yao et al., 2008; Nakamura and Hashimoto, 2009; Wang et al., 2012; Galva et al., 2014; Komis et al., 2014; Nakaoka et al., 2015). From these studies, several types of MT-MT interactions were discovered and have emerged to be major players in defining CMT organization and behavior. Our findings build on this, showing that CMT organization can itself feedback to influence CMT interactions. The observation that ~87% of CMT catastrophes are associated with MT-MT encounter indicates that MT catastrophe, in particular, is heavily influenced by MT-MT interactions and CMT array organization.

Observations by Zhang et al (2013) and Wightman et al (2007) that MTs frequently depolymerize following their katanin-dependent severing at MT-MT crossover points suggests that severing rates may also be influenced by overall CMT organization (since disorganized arrays have more MT-MT crossover points)(Wightman and Turner, 2007; Zhang et al., 2013c).

Based on our findings that MT organization can influence the catastrophe properties of individual MT is important to consider when assessing the in vivo functions of plant MAPs because it may confound assumed measurements of biochemical activities. This is illustrated in the current study by our clasp-1 mutant data. Without taking into account MT-MT influences on dynamic instability, our observations of reduced F_{cat} in clasp-1 mutants could be interpreted to indicate that CLASP functions biochemically to induce MT catastrophe, thereby acting as a MT de-stabilizer. However, numerous studies have shown that CLASP stabilizes MTs via promotion of pause and rescue in animals and fungi (Mimori-Kiyosue et al., 2005; Sousa et al., 2007; Al-Bassam et al., 2010). This apparent contradiction can be reconciled by our data, which suggest that the clasp-1 reduction in F_{cat} results at least in part from the enhanced MT cross-overs associated with weakly cortex-bound CMTs. CLASPs generally stabilize MTs specifically in localized regions of the cell such as cell edges (Ambrose and Wasteneys, 2011; Ambrose et al., 2011), chromosomal kinetochores (Maiato et al., 2003), and between overlapping regions of interpolar spindle MTs in fission yeast (Bratman and Chang, 2007). Therefore, measurements from different parts of a given cell can also yield seemingly contradictory data.

With respect to the mechanism of encounter-based catastrophe, our data suggest that in plants, mechanical forces on MTs play a major role in catastrophe induction. This applies not only to CMT encounter-based catastrophe, but also to cell edge-induced catastrophe (Ambrose et al., 2011). Thus, when considering the cell as a whole, the bulk of CMT catastrophes occur either at cell edges (Ambrose et al., 2011) or via encounter-based catastrophe (current study). In both cases, catastrophe is preceded by behaviors characteristic of MT polymerization against a physical barrier such as prolonged pause and bending (Ambrose et al., 2011; Janson et al., 2003; Komarova et al., 2002; Small and Kaverina, 2003; Wightman and Turner, 2007).

Conclusions

Studies on CMT dynamics and organization in plants generally have focused on the mechanisms by which CMT behavior influences cellular CMT organization. The data presented in the current study show that the organization of CMTs within a cell also has strong influences on CMT dynamic behavior. Thus, a dynamic interplay exists between cellular CMT organization and individual CMT dynamics, indicating feedback between the two elements.

Methods

Plant materials and growth conditions

Transgenic Arabidopsis thaliana (Columbia-0) and clasp-1 lines expressing 35S:TUB6-GFP (Ueda et al., 1999), (Ambrose and Wasteneys, 2008), as well as WT plants expressing 35S:GFP-EB1b (Komaki et al., 2010) were used for measurements. Prior to plating, all seeds were stored in the dark at 4°C for 2 d. Seeds were sterilized in 70% ethanol, rinsed twice with sterile water, and plated onto Petri dishes containing ½ MS media, 1.0% agar, and 1% sucrose. Plates were wrapped with nescofilm (Azwell Inc.) and transferred to a 21 °C growth cabinet (with continuous light) and placed vertically. Young pavement cells of leaf and cotyledon cells were imaged at 3–4 days.

Microscopy and image analysis

All observations were performed on living cells. Cotyledons/leaves were cut at their base, mounted on to slides in Perfluoroperhydrophenanthrene (PP11) (Littlejohn et al., 2014) under a coverslip and sealed with wax. Images were obtained via point-scan confocal microscopy (Zeiss Meta 510 with Zeiss Axiovert 200M microscope, 63X water immersion), TIRF (Olympus IX83 with ANDOR iXon Ultra EMCCD camera, 100X oil immersion), and structured light illumination (Zeiss Apotome mounted on Zeiss Axio Imager Z1 with AxioCam MRm, 63x oil immersion). Time-lapse intervals ranged from 2-5s. Images were processed with Image J software (http://rsb.info.nih.gov/ij/), and figures were assembled using Corel Draw software.

CMT angle and density measurements

For quantification of CMT array order, images were sampled by using five evenly-spaced horizontal rectangular boxes that were 2μm high and as wide as the image. The narrow height was used to remove any ambiguity of MT angle that may arise due to MTs that are bent to varying degrees. Only regions of cells that were covered by a sampling box were measured, which helped remove selection bias when using large cells. MT angles were defined relative to the horizontal

axis of the image. Using the second method to measure CMT angles produced similar results. For this, a central area of the cell (away from edges) was sampled for up to 30 MTs.

For quantification of SF_{cat}, subtractive analysis of sequential time frames was performed by duplicating the time-lapse image twice, and removing one to two frames from the start of the first duplicate, and removing the same number of frames from the end of the second duplicate. Using the image calculator function of ImageJ, the duplicates were then subtracted, and the resulting image was used to count growing plus ends. Since catastrophes were measured for the entire time series, we sampled plus end numbers at four evenly spaced time-points throughout the series and averaged the counts. 21 cells were sampled in total.